COMPUTATIONAL SIMULATION OF DROPLETS

WETTING ON MICRO AND NANO FILAMENTS

A Thesis
Submitted to the Graduate Faculty
of the
North Dakota State University
of Agriculture and Applied Science

By

Amol Anil Bedarkar

In Partial Fulfillment of the Requirements
for the Degree of
MASTER OF SCIENCE

Major Department:
Mechanical Engineering

April 2010

Fargo, North Dakota

North Dakota State University
Graduate School

Title

Computational Simulation of Droplets Wetting

On Micro and Nano Filaments

By

Amol Bedarkar

The Supervisory Committee certifies that this **disquisition** complies with North Dakota State University's regulations and meets the accepted standards for the degree of

MASTER OF SCIENCE

ABSTRACT

Bedarkar, Amol Anil, M.S., Department of Mechanical Engineering, College of Engineering and Architecture, North Dakota State University, April 2010. Computational Simulation of Droplets Wetting on Micro and Nano Filaments. Major Professor: Dr. Xiang-Fa Wu.

In this thesis, wetting properties of liquid droplets on micro and nano filaments were explored. First, droplet-on-filament systems were considered, made of liquid droplets and wetting between parallel filaments of identical geometries and surface wetting properties. Criteria for morphology transition between barrel-shaped droplet and droplet-bridge morphology was determined in terms of critical droplet volume at varying filament spacing, droplet volume, and contact angle. A family of wetting characteristic curves was obtained as a universal law of morphology transition in such systems. Additionally, wetting lengths of the above droplet-on-filament systems were demonstrated at varying geometries and surface properties. Secondly, a surface finite element method was employed to simulate the capillary torque generated in a droplet bridge formed between two misaligned filaments at varying filament spacing, contact angle, droplet volume, and filament orientation angle. Consequently, a novel, hydroelastic model was developed to examine the capillary effect in the mechanical response of ultrathin, soft filaments wetted with droplets and subjected to axial stretching. The filament was modeled as a hyperelastic, Mooney-Rivlin solid, and an explicit stress-stretch relationship was determined. The results obtained in this research broaden the theoretical understanding of droplet wetting and spreading on filaments and are applicable for design and analysis of filament-based microfluidic devices, biological cell manipulators, drug delivers, fiber wetting property differentiators, etc.

ACKNOWLEDGMENTS

TABLE OF CONTENTS

LIST OF FIGURES

CHAPTER 1. INTRODUCTION

Wetting and spreading of liquid on solid surface is one of the ubiquitous, natural phenomena where surface physics and surface chemistry meet and simultaneously dominate the relevant process due to the interaction between liquid molecules and solid surface. Understanding of wetting phenomena is one of the natural interests of human scientific exploration and, to date, has led to remarkable exploitation of these intriguing phenomena and related knowledge for practical utilizations in industry and human life. Among these, wetting and spreading of liquids on filaments is a common experience in life and engineering practices such as wetting of spider web by morning dews, cleaning and dyeing of textiles, chemical treatment of human hair, etc., in which capillary effect plays a crucial role due to the small characteristic dimensions (e.g. radius) of filaments and fibers.

Although the fundamental principles of capillary phenomenon (e.g. the Young-Laplace equation) were established over 200 years ago, rigid study of droplets wetting on filaments started only about three decades ago due to the obstacles raised in both experimental and theoretical aspects. On the experimental side, it needs accurate measurements of micro liter liquids and precise microscopic imaging system; on the theoretical side, it needs to solve a highly nonlinear partial differential equation (PDF) with mixed boundary conditions (BCs). After Carroll's (1976) pioneering work of determining the explicit solution of a barrel-shaped droplet wetting on a filament, substantial research progress has been made on wetting and spreading of droplets on individual filaments such as the roll-up condition of droplets (Carroll, 1986), computational morphology transition between barrel-shaped droplet and clamshell-shaped droplet (McHale et al., 2001; McHale and Newton, 2002),

etc. It needs to mention that birth of the surface finite element method for wetting simulations (e.g. the Surface Evolver package by Brakke, 2000) has remarkably enhanced the capability of accurately determining the morphology of liquids wetting on complex surfaces. Nevertheless, except for an earlier asymptotic study by Princen (1969a, 1969b & 1970), no rigid studies have been reported yet in the literature on morphology transition of droplets wetting simultaneously on multiple filaments. Among these, the simplest case is a droplet-on-filament system made of a droplet wetting on two parallel filaments of identical radius and surface wetting properties. In such a system, a droplet can potentially assume two symmetrical morphologies, i.e. a barrel-shaped morphology to completely enwrap the two filaments or a droplet-bridge partially wetting the filament surfaces. To date, the critical condition of morphology transition in such droplet-on-filament systems is still outstanding. In addition, when a droplet bridge forms between two misaligned filaments, capillary torque will be triggered due to the breakage of symmetry of the droplet-on-filament system. Such capillary torque has not yet been explored. Moreover, with recent development of nanotechnology, ultrathin soft fibers (e.g. those of biopolymers, hydrogels, etc.) with the diameter down to tens to hundreds of nanometers have been conveniently produced by means of electrospinning technique. Wetting of these fibers by micro droplets will lead to significant capillary forces that are expected to appreciably influence their mechanical response. Such hydroelastic problem has not been studied yet in the literature. The above outstanding problems form the main theoretical considerations of this thesis.

In practice, cosmetic engineers at the Ashland, Inc., at Wilmington, DE, recently developed an efficient wetting differentiation characterization technique based on droplet wetting on two parallel human hair fibers (Vaynberg, Stuart and Wu, 2010). This technique

2

is capable of simply differentiating the wetting properties of virgin, damaged, and chemically treated human hair fibers for the development of cosmetic product. Development of rigid theoretical basis for this technique was conducted in Professor Xiangfa Wu's group at NDSU and directly inspired the initial research of this thesis.

The research of this thesis consists of four parts. In Chapter 2, a brief literature review is made on surface tension, surface wetting, and droplets wetting on single and multiple filaments. Chapter 3 is dedicated to determination of the critical condition of morphology transition between a barrel-shaped droplet and a droplet bridge wetting symmetrically on two parallel filaments. Surface finite element method is adopted to simulate the morphology assumed by the droplets at varying filament spacing, droplet volume, and contact angle. A family of wetting characteristic curves is first achieved. Chapter 4 is devoted to calculating the capillary torque triggered by a droplet bridge formed between two misaligned filaments of identical geometries and surface wetting properties. The influences of filament spacing, droplet volume, contact angle, and filament orientation are examined numerically in detail by using the surface finite element method. In Chapter 5, a novel hydroelastic model is developed to examine the capillary effect in the mechanical behavior of ultrathin, soft fibers wetted with droplets. The material of the soft fibers is modeled as isotropic, hyperelastic Moony-Rivlin solid, and an explicit stress-strain relationship is obtained. This initial study is expected to open up a new research field of hydroelasticity of micro and nano filamentary materials. Consequently, summary and future development of the research is presented in Chapter 6.

In this study, the Surface Evolver software package (Brakke, 2000) was adopted for the numerical simulations of all the cases of droplets wetting on filaments.

3

CHAPTER 2. LITERATURE REVIEW

Wetting and spreading phenomenon is omnipresent in nature, life experiences and engineering practices. The principles of wetting and spreading have found vibrant applications in textile industry (e.g. dyeing, cleaning and waterproofing), polymer composites processing, cosmetic products development, and many other fields. Due to its crucial role in modern industry and life, the research of wetting and spreading has attracted significant researchers all over the world in the last several decades. In a particular area of droplet wetting on filaments, to date, not much has been researched on the fundamental understanding of liquid droplets wetting on multiple microfilaments although there exists broad complimentary research in the literature. This literature review is devoted to introduction of the fundamental concepts of wetting and spreading of liquid droplets on surfaces and then the current understanding of liquid droplets wetting on single and multiple microfilaments.

2.1. Surface Tension

In the state of liquid, neighboring molecules in a fluid are associated with strong attraction called as cohesive attraction. The strength of such force dominates the nature of fluid; if the cohesive attraction is stronger than thermal agitation, molecules transfer from gaseous phase to liquid phase.

In the interior surface of a liquid, molecules are subjected to equal cohesive forces exerted by neighboring molecules in all directions so that their net force becomes zero. Therefore, the internal molecules of a liquid can be described as equilibrium molecules. However, the molecules at the surface of a liquid are subjected to cohesive attraction,

4

which is balanced by liquid's resistance to compression. This force is responsible for minimizing the surface area of a liquid. These molecules are called nonequilibrium molecules, as they are responsible for a liquid adjusting its shape by minimizing the potential energy. Both types of the molecules are shown in Fig. 2.1.
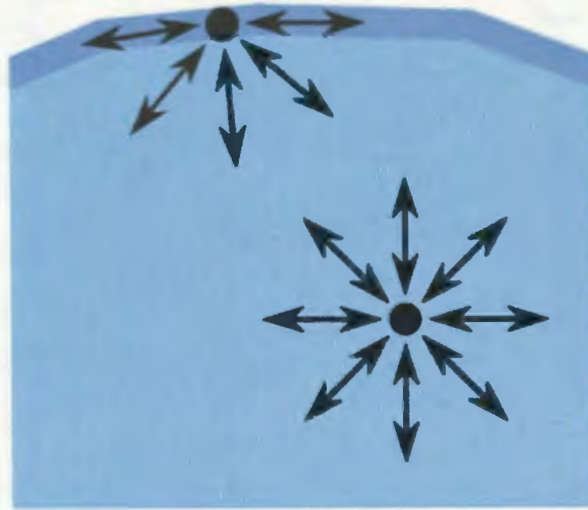
Figure 2.1: Physical origin of surface tension at molecular level. (Booyabazooka 2008)

Obviously, the cohesive energy of nonequilibrium molecules (molecules at the liquid's surface) is less than that of equilibrium molecules (molecules in the interior of a liquid). The loss of cohesive attraction is considered to be cut in half. If U is the cohesive energy per equilibrium molecule, a nonequilibrium molecule corresponds to half of the cohesive energy, i.e. $U/2$. Surface tension is a direct measure of this lost cohesive energy per unit of surface area. If 'a' is the molecule size and a^2 is the exposed surface area, the surface tension is approximately equal to $\gamma = U/(2a^2)$. Dimensionally, $[\gamma] = EL^{-2}$ and its unit will be J/m^2.

1. Water strider

Some insects, such as water striders, entirely depend on surface tension for living. Water striders walk over the water by using surface tension. As shown in Fig. 2.2, water striders grow two pairs of long legs, while the first pair is relatively shorter than the remaining one. In addition, water striders also have numerous hairs on each pair of legs. The nature of the hydrophobic hairs of the pair makes water striders float on water, while the hydrophilic pairs penetrate through the water surface to facilitate hunting prey. The hydrophilic legs of water striders deflect water, making dents and increasing its surface area, and the hairs on its legs boost this process. The mass of water strider is very low, and its resulting gravity is equal to the net force of the surface tension induced on the distorted water surface.

Figure 2.2: Insect walking on water surface creates impression on water surface which generates surface reaction forces (Bush, 2004).

2. Droplet formation from water stream

Fig. 2.3 shows a common example of droplet formation in a thin jet. When a jet of water has sufficient flow rate, it forms a thin cylinder of water. However, when the flow rate

6

reduces, the jet consequently forms spherical droplets. The reason lies in the concept of minimization of surface energy. By reducing the flow rate, the radius of the jet reduces correspondingly. As a result, the surface area of a formed cylinder is larger than that of formed discrete spheres in the condition of the same amount of volume. At this point, water takes the form of droplets instead of a water jet to minimize the surface energy and surface area.

Figure 2.3: Stream of water transforms to water droplets (Herval 2005, retrieved from http://www.flickr.com/photos/herval/19252684/sizes/o/)

2.2. Droplets on Single Cylinders

2.2.1. Laplace pressure

Before discussing interaction between droplets and a single cylinder, it is necessary to introduce the concept of Laplace pressure. Laplace published his seminal work on capillary pressure of liquids in 1805. In Laplace's view, there is an overpressure existing inside of a droplet, and surface tension is the prime reason for developing this overpressure.

Fig. 2.4 illustrates Laplace's overpressure in an oil droplet enwrapped by water where and are the pressures inside the oil droplet and water, respectively.

7
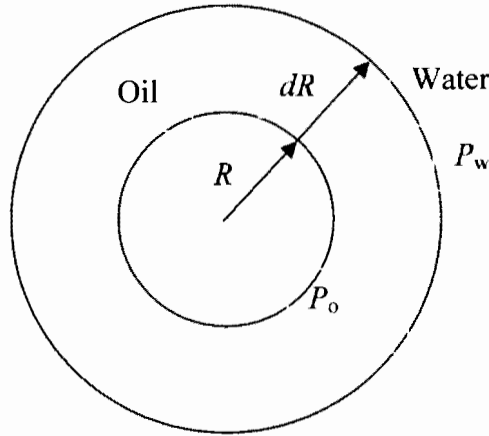
Figure 2.4: Laplace's concept of overpressure inside a droplet.

If the oil/water interface is displaced by dR, the work done by the pressure and the capillary force can be written as

$$\delta W = -p_o dV_o - p_w dV_w + \gamma_{ow} dA, \tag{2.1}$$

where $dV_o = 4\pi R^2 dR = -dV_w$ and $dA = 8\pi R dR$ are the increments in volume and surface area, respectively, and γ_{ow} is the specific interface energy between water and oil. Applying the condition of equilibrium $\delta W = 0$ leads to

$$\Delta p = p_o - p_w = \frac{2\gamma_{ow}}{R}. \tag{2.2}$$

After generalization to an arbitrary curvilinear surface, it has

$$\Delta p = \gamma \left(\frac{1}{R_1} + \frac{1}{R_2} \right) = \gamma C, \tag{2.3}$$

where R_1 and R_2 are the principal radii of curvature of the surface and $C = \left(\frac{1}{R_1} + \frac{1}{R_2} \right)$.

2.2.2. Interaction of droplets with a single cylinder

Wetting properties of liquid rely on its chemical properties and surface geometry. When surface geometry is considered, cylindrical shape is the most common shape observed in

8

nature. For instance, fibers and filaments are the most fundamental building blocks integrated in various natural and engineering materials (e.g. trees, textiles, fiber composites, etc.) and structures. Besides, study of liquid droplets on cylindrical microfilaments is crucial to exploring the adhesive properties of composite materials and it can be extended in optimizing the mechanical properties and improving the interfacial shear strength between fibers and matrix in fiber-reinforced polymer composites (Bernet et al, 2000). Moreover, wetting properties can also be used in determining fiber coating conditions (Quere, 1999), chemical modification and decoration of carbon nanotubes (CNTs) (Ebbesen, 1996), among others. Fig. 2.5 shows a microdroplet wetting on a single cylinder.
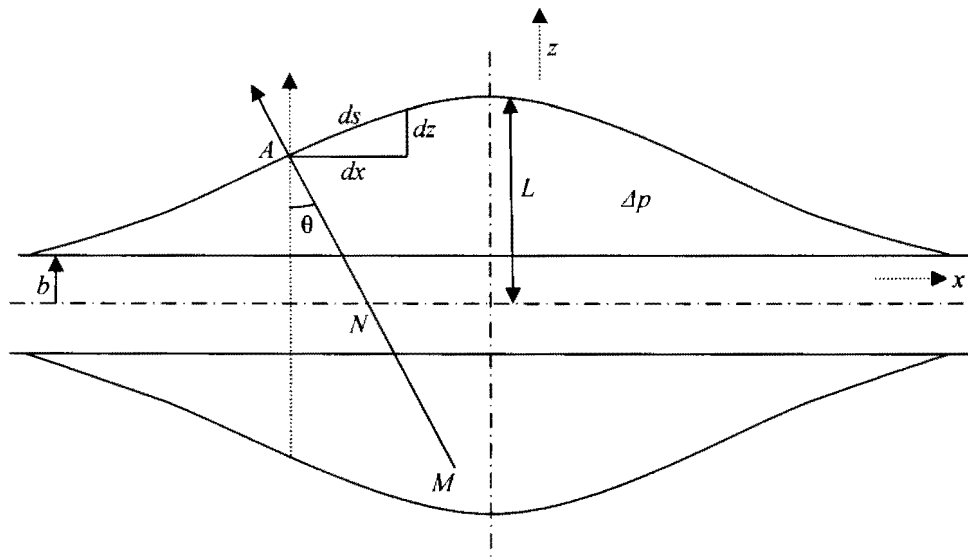
Figure 2.5: Schematic diagram of a micro-sized droplet on a single cylinder (Gennes et al, 2001).

In such a study, the gravity can be safely neglected due to the small droplet volume (i.e. the characteristic dimension is much larger than the capillary length). According to Eq. (2.3), the Laplace overpressure inside the droplet wetting on the cylinder is

Herein,   is the overpressure,   is the surface tension,   is a constant curvature, and

and   are the two principal radii of curvature at a particular point on the droplet surface.

Consider a point '*A*' on a particular location on the droplet surface, here   = *AM* and

=*AN*. Point *N* lies at the intersection of normal *MN* to the surface at point '*A*'. For this

system, the above Laplace overpressure equation can be recast as (Gennes et al. 2001)

$$\overline{\qquad\qquad} \quad \overline{\qquad\qquad} \quad —$$

The above equation can be also obtained by the summation of all the forces acting on a

representative differential area left to the vertical line at point *A* and equating it to zero.

These forces include the capillary forces, forces due to the pressure and forces exerted by

the fiber on the droplet. Fig. 2.6 shows an Epon^{TM} resin droplet resting on a single carbon

fiber with the diameter around 10 μm.
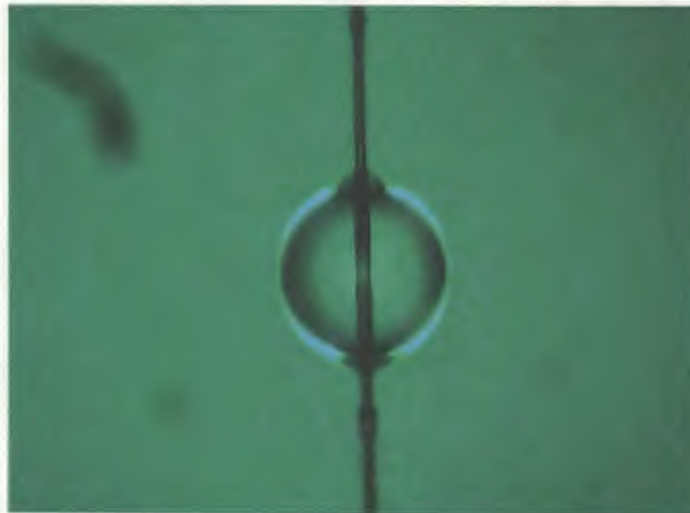
Figure 2.6: An Epon^{TM} resin droplet wetting on a single carbon fiber. [Image was captured
using an optical microscope at the North Dakota State University].

2.2.3. Roll up transition

Both the wetting behavior and droplet profile will be no longer the same when a droplet is resting on the cylindrical surface compared to that resting on a flat surface. As shown in Fig. 2.8, two possible morphologies can be assumed in such a system, i.e. a barrel shape and a clamshell. Carroll (1976) first studied the barrel-shaped droplet on a single fiber, and he re-derived the Laplace overpressure expression in dimensionless quantities by using the elliptical integrals of the first and second kind. This expression can be further used to determine other quantities, such as droplet volume and wetting length, as well as Laplace overpressure inside the droplet. Fig. 2.7 illustrates the definitions of symbol that Carroll used in his study.
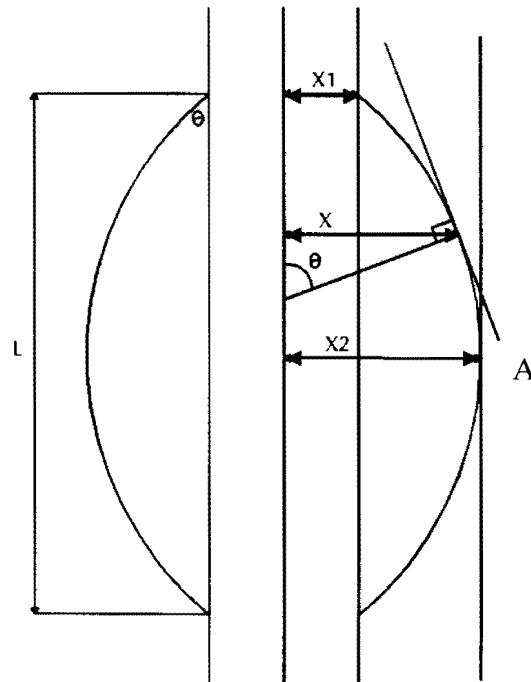
Figure 2.7: Definitions of symbol used by Carroll (1976)

In his study, Carroll (1976) employed two dimensionless quantities n and defined by

$$n = \frac{x_2}{x_1} \text{ and } \bar{L} = \frac{L}{x_2}.$$

In this case, overpressure inside the droplet can be expressed as

$$\Delta p = \frac{2\gamma(n - cos\theta)}{x_1(n^2 - 1)}. \tag{2.5}$$

Parameters used in Eq. (2.5) are explained in Fig. 2.7. This equation can be used to understand the roll-up process. Fig. 2.8 describes how such a transition takes place from a barrel-shaped droplet to a clamshell shaped droplet. When the contact angle is small or close to zero, a droplet wetting on a single cylinder will form a symmetrical profile with respect to the cylinder axis (called as barrel-shaped morphology); when this contact angle is sufficiently large, a non-symmetric morphology is formed (called a clamshell-shaped morphology). The critical contact angle responsible for the transition from a barrel-shaped morphology to a clamshell-shaped morphology depends upon the droplet volume and cylinder radius (Carroll, 1976). Adam (1937) was the first to emphasize the importance of roll-up for the process of detergency of oils from fabrics.

(a)   (b)
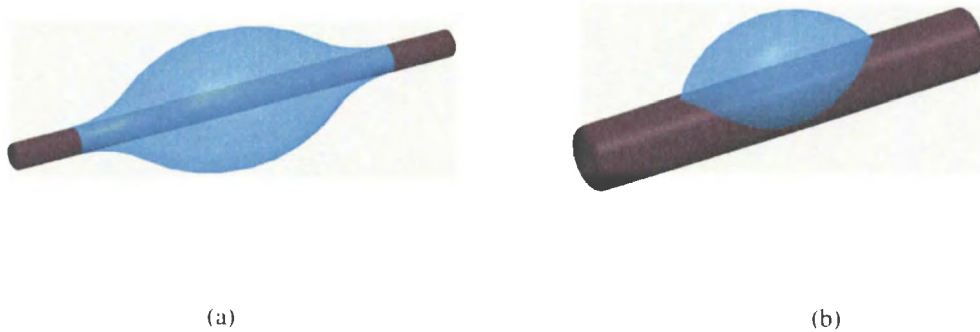
Figure 2.8: Roll-up transition from a barrel-shaped morphology to a clam-shell shaped morphology. (a) Barrel-shaped morphology. (b) Clam-shell shaped morphology [Images were drawn in ProE wildfire and overall size of (b) was zoomed to show the droplet profiles].

12

In addition, Carroll (1986) explained the roll-up process by using Eq. 2.5 as the starting point.

$$\Delta p = \gamma \left(\frac{1}{R_1} + \frac{1}{R_2} \right) = \frac{2\gamma(n - \cos\theta)}{x_1(n^2 - 1)}. \tag{2.6}$$

At point A in Fig. 2.7, the principal radius of curvature R_2 is equal to x_2. Combination of this condition with Eq. (2.6) leads to the remaining principal radius of curvature as

$$\frac{1}{R_1} = \frac{n^2 - 2n\cos\theta + 1}{x_1(n^2 - 1)} \quad and \quad \frac{1}{R_2} = \frac{1}{x_1 n}. \tag{2.7}$$

Now, a small perturbation of the barrel-shaped geometry is allowed from its equilibrium position involving a small movement of contact lines at a constant droplet volume. In such a perturbation, at point A, R_2 increases and R_1 decreases. Change in the Laplace pressure is given by using Eq. (2.8):

$$\delta(\Delta p) = \gamma \left(\frac{n^4 - 4n^3\cos\theta + 4n^2 - 1}{n^2(n^2 - 1)^2} - \frac{1}{n^2} \right). \tag{2.8}$$

Value of $\delta(\Delta p)$ changes its sign at particular values of n and θ. These values can be obtained by solving the resulting equation: $2n^3\cos\theta - 3n^2 + 1 = 0$.

When $\delta(\Delta p)$ <0 (upper part of Fig. 2.9), a stable barrel-shaped morphology prevails, while for $\delta(\Delta p)$ >0 (lower part), the metastable morphology of the clamshell can exist. The curve satisfying equation, $2n^3\cos\theta - 3n^2 + 1 = 0$ serves as the boundary between the two morphologies. Experimentally, it is difficult to change this contact angle in a controlled environment. However, this problem was solved by varying the droplet volume instead of the contact angle. For instance, an oil drop attached to a fiber can be immersed in a surfactant solution where the oil is dissolved slowly over time, while maintaining the same contact angle (Carroll, 1986).

13
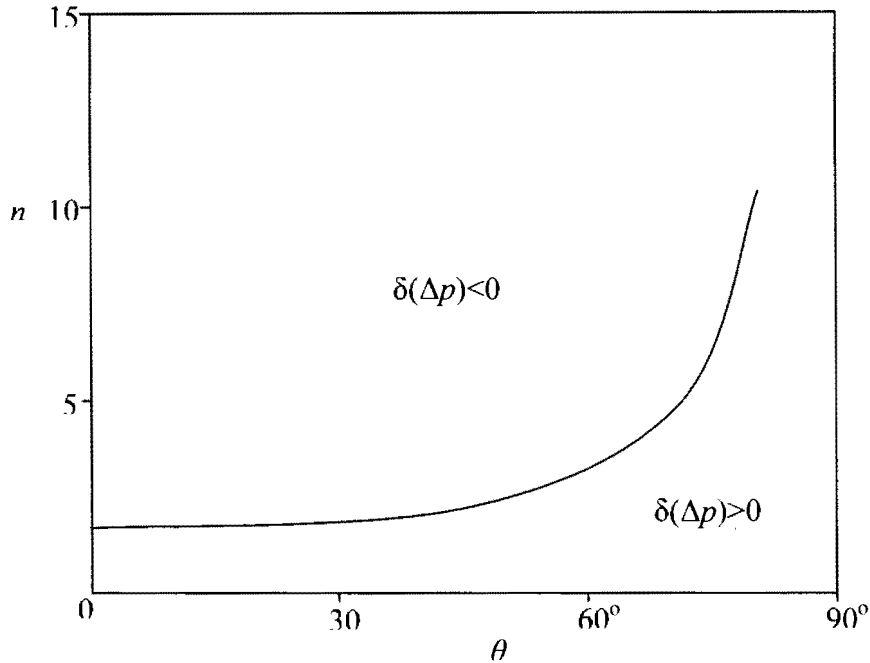
Figure 2.9: Diagram of critical value of n vs. critical value of θ (Carroll, 1986).

Furthermore, McHale and Newton (2002) also studied the roll-up process using a surface, finite element approach, in which they determined the possible shape of a droplet on a cylindrical profile. It was considered that "*The stability of a barrel shape is lost when reduction in droplet volume causes the inflexion point to touch the fiber surface*" (McHale et al., 2001). The point of inflexion is where the principal radius of curvature R_1 changes its sign from positive to negative. Therefore, the profile of curvature is opposite near the cylindrical surface in contrast to that away from the surface.

In addition, McHale and Newton (2002) explained the condition of absolute stability based on the concept of minimum surface energy. They used a surface finite element software package (Brakke, 2008) to calculate the surface energy for certain physical quantities. For the same physical quantities, the lower the minimum surface energy, the

14

more stable is the corresponding morphology. They summarized the concepts of absolute stability, metastability and inflexion condition in the following Fig. 2.10. (McHale & Newton, 2002).
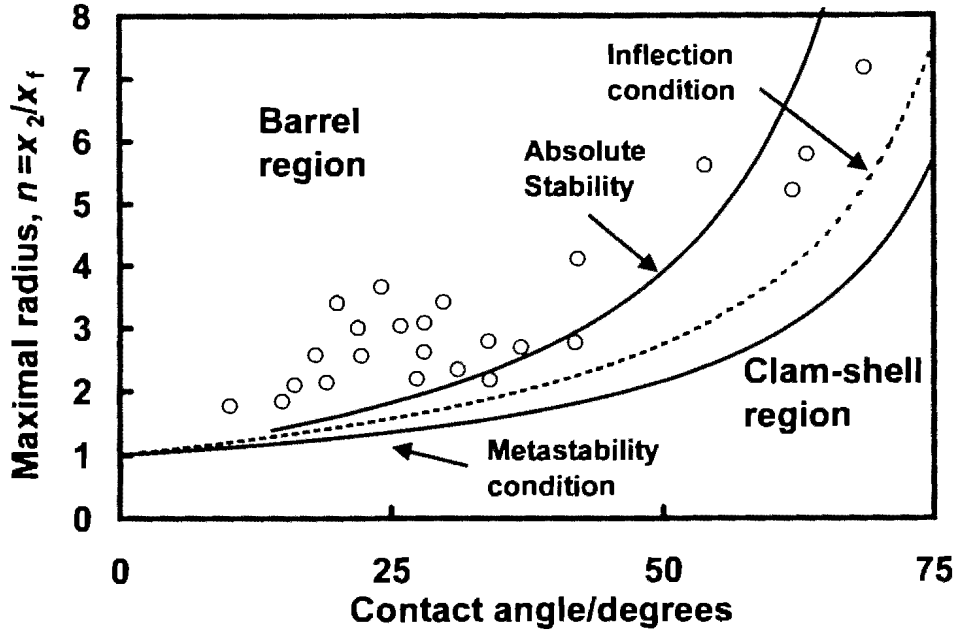
Figure 2.10: Explanation of absolute stability, inflection condition, and metastability. The curves divide the entire domain into two regions, i.e. the barrel and clam-shell regions, respectively (McHale & Newton, 2002).

2.2.4. Droplets on inclined fibers

An implicit assumption made in the above studies is that the effect of gravity was neglected. What will happen when the cylinders are inclined at a certain angle and gravity should be taken into account due to appreciable droplet size? In nature, dew hanging on the stems of weeds in various tilted angles is often observed. Huang, at al. (2009), worked on the equilibrium of droplets on inclined fibers. They performed detailed experiments with silk fibers (spoke and spiral silk fibers) as well as engineering fibers (carbon and Kevlar fibers) and evaluated the critical angles of inclination, below which the equilibrium can be achieved, while above which droplets start sliding over the surface of fibers. They proved

15

that a sine function of this angle is reciprocal to the droplet volume and this relationship is linear. Based on their experiments and numerical analysis, the equilibrium condition from angle 0° (horizontal cylinder) to 90° (vertical cylinder) is achieved. Fig. 2.11. illustrates the rate of increase in critical angle of inclination with respect to $1/V$. This rate of increase varies at different cylindrical configurations, material properties, and the properties of droplets, such as surface tension.
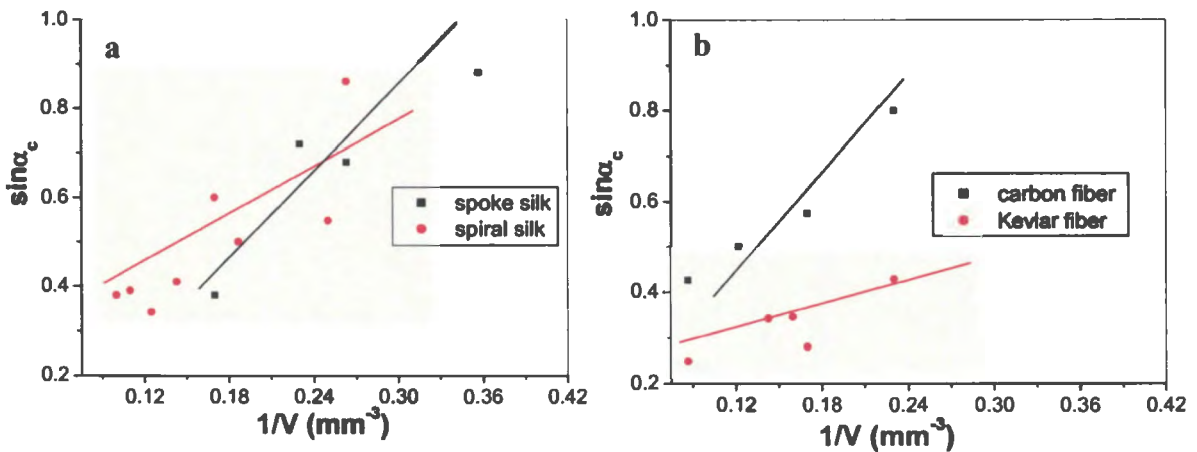
Figure 2.11: Angle of inclination at which droplets start sliding as a function of droplet size: (a) Spoke and silk fibers and (b) carbon and Kevlar fibers. (Huang et al, 2009)

2.2.5 Determination of contact angle on single cylinders

When a droplet sits on a flat surface, determination of its contact angle is a straightforward, convenient procedure. The experimental determination can be conducted by primarily two methods, i.e. the goniometer and Wilhelmy's methods. In the goniometer procedure, a droplet is deposited on the flat surface of a solid material by using a small diameter syringe. Images can be captured using a high-resolution camera and the contact angle is extracted either by using a protractor or with special purpose image analysis software. By varying the droplet size, a large number of data can be averaged to consolidate the results. This is the most common and simplest method, but it often comes

16

with a high possibility of measuring and instrumental errors. The second method is Wilhelmy's method. During this process, a force meter is attached to a flat, solid plate which is vertically dipped into the liquid under consideration. The force meter measures the force exerted by a liquid on a flat surface. Contact angle can be calculated by the formula:

$$cos\theta = \frac{(F - F_b)}{L\gamma}.$$

2.9

Here, F is the total force measured by the force meter, F_b is the buoyancy force due to liquid displacement by the solid plate, L is the wetted length, and γ is the surface tension of the liquid.

Although these methods work well with flat, solid plates, experimental results become less accurate and less reproducible when the flat, solid plates are replaced with thin, cylindrical fibers. The main reason for this is that part of the liquid profile near the cylinder has the principal curvatures of very high magnitude and opposite sign to the cylinder radius (Yamaki & Katayama, 1975). It is well known that cylindrical shape is the most common geometry in nature and its wetting properties play an important role in many other studies. Among others, Carroll and Yamaki (1975) developed a method to evaluate the contact angle of a droplet-on-fiber system. They discribed three diagrams, namely $L - K$, $L - \alpha$ and $K - \alpha$. Herein, L and K parameters can be determined by droplet height, droplet length, and cylinder radius, and α is the apperant contact angle at which the liquid surface curve becomes linear and can be measured conveniently.

Furthermore, Wagner (1990) presented two methods to determine the contact angle using an itterative approach:

1. $\theta = cos^{-1}\left\{\dfrac{1}{t} + \left(1 - \dfrac{cos\theta}{t}\right)\left[\dfrac{l(t^2+1-2tcos\theta)^{0.5}}{2(t-cos\theta)R_F} - t\left(1 - \dfrac{1}{3}\dfrac{(t^2-1)}{t^2(t^2+1-2tcos\theta)}\dfrac{R_D}{R_F}\right)\right]\right\}$,

2. $\theta_i = \dfrac{\theta_{i-2}-\theta_{i-1}}{l_{i-2}-l_{i-1}}l + \dfrac{l_{i-2}\theta_{i-1}-l_{i-1}\theta_{i-2}}{l_{i-2}-l_{i-1}}.$ 2.10

In the first method, an initial θ is the first trial value which can be chosen from plots given by Carroll (1976). Other parameters can be discovered through a visual inspection. In the second method, the first trial value is made by using the same manner as that of the first method and the second trial is selected close to the first value (Wagner, 1990). Besides, Song and his co-workers (Song et al., 1998) used the Carroll's integration as the basis of their study and proposed a numerical algorithm to extend Carroll's study for contact angle determination based on experimental measurements.

Recently, Wu and Dzenis (2006) demonstrated a simple semi-analytic approach to determine the contact angle of droplets on single fibers with high accuracy when the contact angle is above 15°. They began with the free energy variation of a droplet on a cylindrical fiber and re-derived the governing equation and boundary conditions based on the geometrical shape, contact angle and fiber wetting length.

2.3. Droplets on Two Parallel Cylinders

2.3.1. Analytical studies

When a pair of parallel thin cylinders is dipped vertically into liquid, capillary rise between two cylinders occurs. Princen (1969a, 1969b, & 1970) in his three papers gave an in-sight interpretation of this phenomenon by means of asymptotic approaches. In the first paper, Princen calculated the capillary rise of liquid between the two parallel cylinders as a function of the distance of separation and contact angle which occurs when the contact angle is less than 90°. When the contact angle is greater than 90°, capillary depression takes

18

place and the configuration will have mirror image as that of capillary rise (Princen, 1969a).

In addition, by assuming that the capillary rise was much larger than the radius of cylinders, Princen (1969b) formulated the following equations. The parameters used in Eqs. (2.11) and (2.12) are explained in Fig. 2.12.

$$\frac{R_2}{r} = \frac{1 + \dfrac{d}{r} - cos\alpha_2}{cos(\theta + \alpha_2)},$$ 2.11

and

$$\left(\frac{R_2}{r}\right)^2 \left[\frac{\pi}{2} - (\theta + \alpha_2) + sin(\theta + \alpha_2)cos(\theta + \alpha_2)\right]$$

$$+ 2\left(\frac{R_2}{r}\right)[sin\alpha_2 cos(\theta + \alpha_2) - \alpha_2 cos\theta] + sin\alpha_2 cos\alpha_2 - \alpha_2 = 0.$$ 2.12

Both of above equations can be solved for various values of (d/r) and θ. Then, the capillary rise can be calculated by

$$\frac{z_2}{r} = \frac{1}{cr^2}\frac{r}{R_2},$$ 2.13

where z_2 is the capillary height and $c = \rho g/\gamma$.

Princen further stipulated similar equations for droplets between a solid plate and a cylinder. Using these equations, he conducted detailed numerical analysis and indicated that the capillary rise is less for a higher contact angle and higher spacing between two parallel cylinders.

19
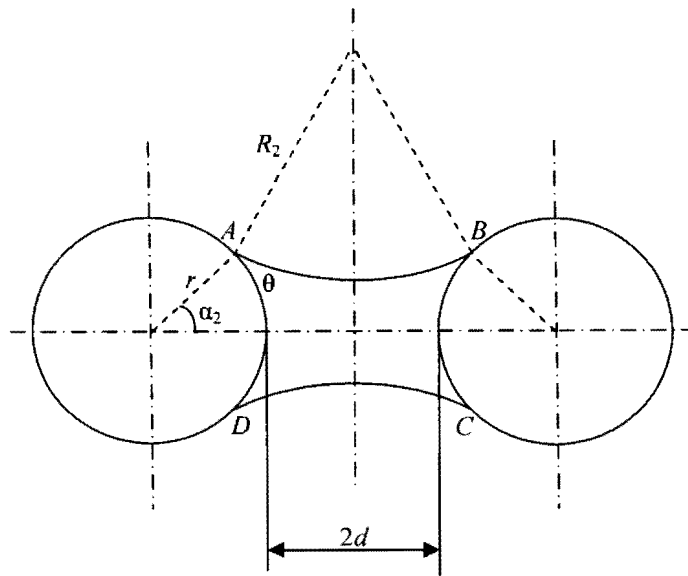
Figure 2.12: Definitions of geometrical parameter in the horizontal cross-section used by Princen (1969a).

2.3.2. Differential Wetting Characterization of Human Hair Fibers

Wetting properties of human hair are vital in hair-caring products and hair treatment. Undamaged human hair is hydrophobic in nature; this is because of the outermost epicutical layer which protects the hair core. Due to effects by chemicals and weathering, this epicutical layer is gradually removed, making human hair hydrophilic. Therefore, the purpose of hair treatment is to keep this layer intact or keep the human hair hydrophobic in nature. Vaynberg and co-workers (Vaynberg, Stuart, & Wu, 2010) at Ashlan Inc., DE, developed a new technique, termed as differential wetting characterization (DWC) method (Fig. 2.13), which allows a simple, efficient characterization of human hair fibers. Fig. 2.14 shows the variation in the droplet profile as the extent of damage to the hair fiber increases from the left to the right.
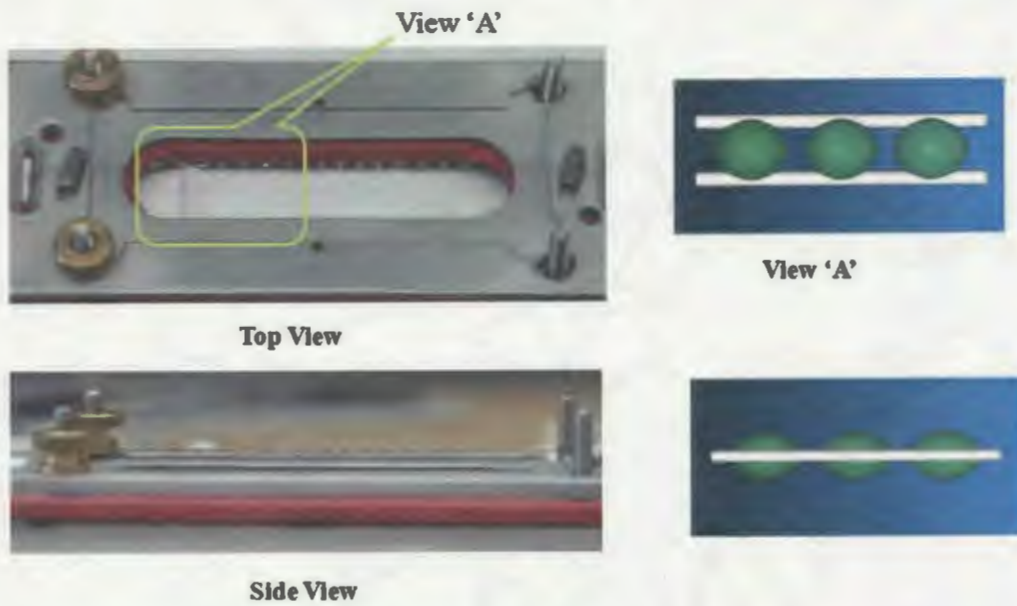
Figure 2.13: Experimental setup for differential wetting characterization of liquids (Vaynberg, Stuart, & Wu, 2010).

Figure 2.14: Variation in water droplet shape with the extent of damage. Stripping and bleaching indicate the extents of damage to outer layer of human hair, respectively. The reference fiber at the bottom was virgin in all cases. (Vaynberg, Stuart, & Wu, 2010)

The outer protective layer (18-methyl-eicosanoic acid) was removed with treatments including stripping and bleaching. Removal of this layer made hair hydrophilic by reducing its contact angle against water. After stripping, 1 hour of bleaching and 2 hours of bleaching, the contact angle was reduced to $83\pm2^{\circ}$, $78\pm1^{\circ}$, and $77\pm1^{\circ}$, respectively (Vaynberg, Stuart, & Wu, 2010). Furthermore, images in Fig. 2.14 show the water droplets tended to tilt towards the damaged hair fiber while in the first case, both hair fibers were virgin and hydrophobic, and the droplet profile was symmetrical.

Experimental work performed by Vaynberg and co-workers inspired the resarch of this thesis. Experimental images obtained from these experiments were compared with simulation results by keeping all parameters (e.g. droplet volume, fiber diameter, spacing between two hair fibers and contact angles) close to those observed in experiments. While working on these simulations, we were confronted with several outstanding problems in regards to this field, which will be described in a further subsection.

2.4. Droplets on Multi-Cylinder Systems

Theory of droplets wetting between parallel cylinders can be extended to multi-cylinder systems. Structures such as hexagonal lattice and square lattice are commonly observed in woven textiles, woven paper, and metal media. The basic constituent of such structures is three-cylinder and four-cylinder systems, respectively. It is important to study systems of droplets on these three- or four-cylinder systems. In his early works (Princen, 1969a, 1969b & 1970), Princen derived the mathematical equations for these multi-cylinder systems by using a similar approach and criteria as used for droplets on two parallel cylinder systems.

When the distance between cylinders ($2d$) is very small, there exist two heights for capillary rise, i.e. lower and upper boundaries. When this distance increases, the upper

22

boundary elevation reduces faster than the lower boundary and the condition is reached when the two boundaries intersect with each other. This transition occurs at a distance of d_{tr}, so analysis can be divided into two parts $d<d_{tr}$ and $d>d_{tr}$. A typical three-cylinder system wetted by a liquid droplet is illustrated in Fig. 2.15.

(a)   (b)
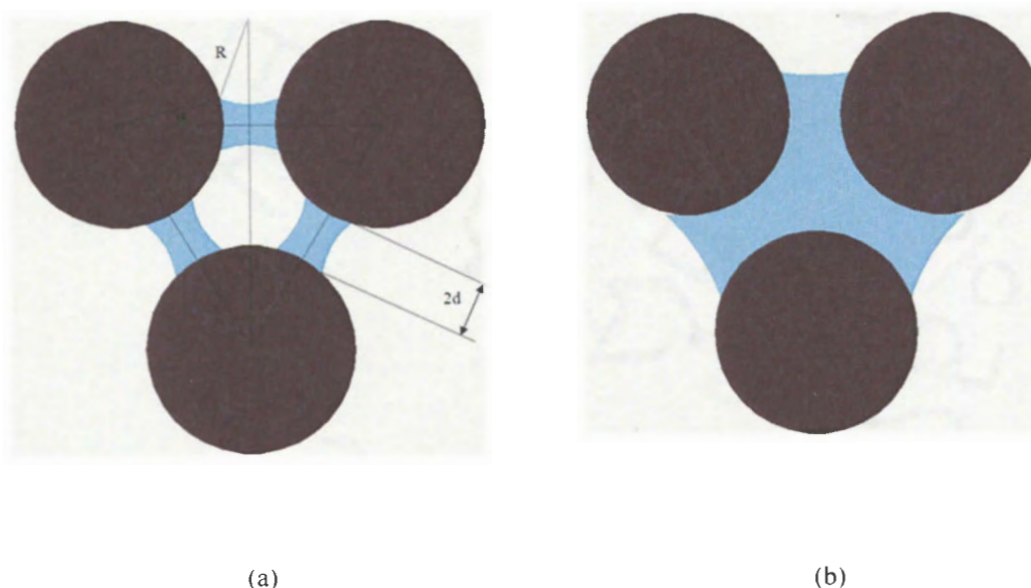
Figure 2.15: Horizontal cross-section of three parallel cylinder systems.   Definition of parameters used by Princen a) $d<d_{tr}$ b) $d>d_{tr}$. (Princen, 1969a &1969b)

When the distance is less than d_{tr}, the third cylinder does not affect the capillary height and the shape of liquid is the same as in two-cylinder systems. Similar behavior was also observed when the droplet was resting on four-cylinder systems (Princen, 1969a & 1969b).

Work conducted to complete this thesis used the roll-up process in multi-cylinder systems. Two parallel cylinder (filament) systems and two angled cylinder (filament) systems will be employed to explore different properties.

23

2.5. Outstanding Problems to be Resolved

1. Morphology transition: It has been observed that when a liquid droplet is resting symmetrically on two parallel microfilaments, only two possible symmetrical morphologies can be observed, i.e. a barrel-shaped morphology in which the droplet completely enwraps both the filaments, and a bridge-shaped morphology in which the liquid partially wets the filaments. The transition between these morphologies has not been explored in the past.

2. Wetting length dependencies: In the above droplet-on-filament systems, variation of the wetting length at varying fiber spacing, contact angle, and droplet volume has not been discussed yet in the literature.

3. Capillary torque of a droplet bridge wetting on two angled filaments: When the geometrical symmetry of two parallel filaments is disturbed in contact with a liquid droplet, the filaments try to align themselves to achieve symmetry (i.e. in parallel) to reduce the system's potential energy. This scenario needs to be explored for potential application in micro fluidics.

4. Micro droplets wetting on ultrathin fibers induce appreciable capillary forces, which consequently modulate the mechanical behavior of fibers, especially for ultrathin soft fibers. Moreover, because of compressive axial forces by hydrophilic liquid droplet, capillary buckling is likely to happen in fibers. The behavior of ultrathin soft fibers, coupled with a capillary effect, has not been studied in the literature.

These outstanding problems form the main theoretical considerations for developing the research of this thesis.

24

CHAPTER 3. MORPHOLOGY TRANSITION AND WETTING LENGTH OF DROPLETS ON TWO PARALLEL FILAMENTS

In this chapter, morphology transition of droplet wetting on two parallel filaments is explored. As mentioned in Chapter 2, a droplet wetting symmetrically on two, identical, parallel filaments can assume a barrel-shaped morphology or a liquid bridge, depending on the filament configuration, droplet volume, and contact angle. In this study, the critical condition for morphology transition between a barrel-shaped morphology and a liquid bridge is defined in terms of a critical droplet volume. When the droplet volume is large enough to enwrap both filaments, a barrel-shaped morphology is preferred. As the droplet volume reduces below the critical droplet volume, a liquid-bridge is formed. Secondly, in the above droplet-on-filament systems, variation of the wetting length with respect to contact angle is explored at varying droplet volume, fiber spacing, and droplet morphology. During the process, the Surface Evolver software package (Brakke, 2008) is utilized for numerical simulations of all cases of droplet-on-filament systems under consideration.

3.1. Introduction

In Chapter 2, the literature review was mainly focused on the wetting and spreading of droplets on individual filaments. In reality, fibers mostly exist in state of yarns/bundles, fiber networks/fabrics, or woven and nonwoven textiles. Among these, the simplest and basic structure is the one made of two parallel filaments in contact with liquid. Princen (1969a, 1969b, & 1970) first studied this case and determined the capillary rise in two or multiple cylindrical filaments. Such a droplet-on-filament system is applicable for

manipulating micro-quantities of fluids (Keis et al., 2004). Experimental study (Keis, et al, 2004) has indicated that droplet spreading on such filament systems approximately follow the Lucas-Washburn law, which states that meniscus displacement is proportional to the complete wicking time (the time interval from the start of droplet spreading to its disappearance) for given fiber spacing (Lucas, 1918 & Washburn, 1921). Consider a droplet wets symmetrically on two parallel identical microfilaments with gravity and other microscopic forces ignored. Two possible morphologies are possible, i.e. a barrel-shaped morphology, which completely enwraps the two fibers; or a droplet bridge, which only wets the inside surface of the filaments. Detailed numerical studies have been performed to evaluate surface energies of droplets with two different morphologies by varying the parameters, including droplet volume, contact angle, and filament spacing. Morphology transition between a barrel-shaped morphology and liquid bridge morphology is addressed in view of droplet volume at given contact angle and filament spacing. A family of wetting characteristic curves is obtained in terms of dimensionless droplet volume with respect to filament spacing ratio at varying contact angles. The wetting characteristic curves can be considered as a universal law that governs morphology transition of droplets wetting on filaments.

Figs. 3.1(a) and (b) show the barrel-shaped morphology and a liquid bridge, respectively. Fig. 3.2 shows the morphology transition from a barrel-shaped system to a bridge-shaped system when the liquid droplet volume is gradually reduced.

Fig. 3.3 shows the images captured when a water droplet wetted on two human hair fibers with different contact angles. The water droplet was allowed to evaporate over time. These images show the tendency of morphology transition from a barrel shape to a bridge

26

shape. Finally, the droplet was detached from the more hydrophobic hair fiber and rest on the hydrophilic hair fiber.

(a)   (b)
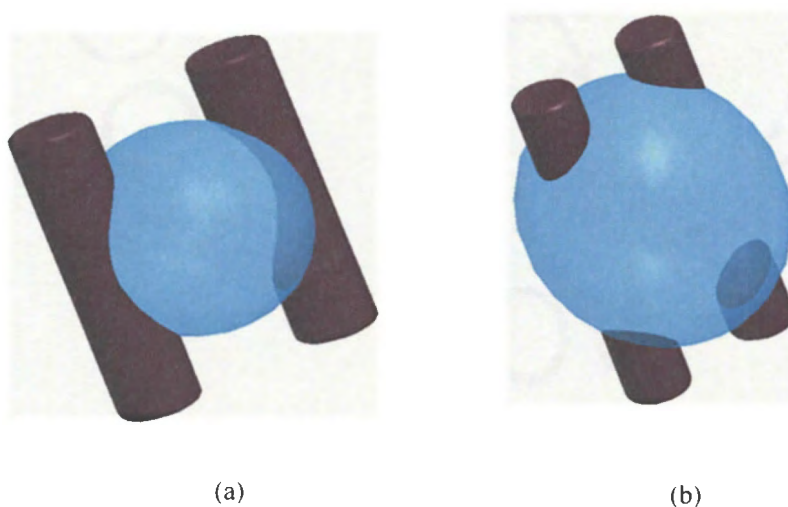
Figure 3.1: Different morphologies for systems made of two parallel filaments in contact with a liquid droplet: (a) Bridge-shaped system when the droplet volume is less; (b) Barrel-shaped system when the droplet volume is larger enough to wrap both the filaments
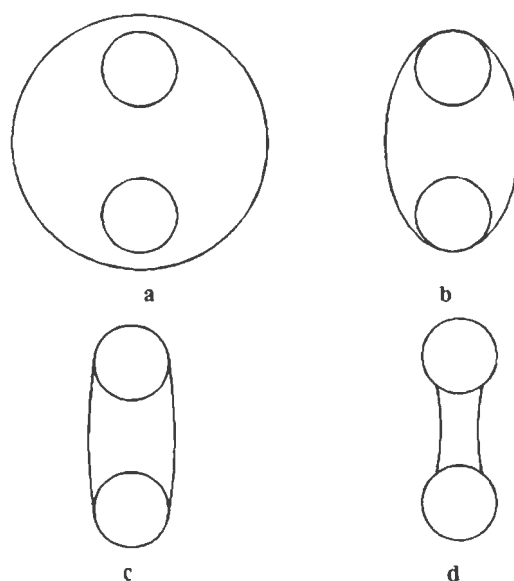
Figure 3.2: Morphology transition when liquid is allowed to evaporate. Transition from a barrel shape to a bridge shape occurs from (a) to (d) as droplet volume reduces.

27

Figure 3.3: Experimental images when a droplet of water sat on two human hair fibers with dissimilar contact angles. Water was allowed to evaporate and morphology transition was observed from a barrel shape to a bridge shape. Finally, the droplet was attached to the more hydrophilic hair fiber having less contact angle. (Experiments were performed at Ashland, Inc. Dublin, OH, USA) (Vaynberg, Stuart, & Wu, 2010).

Secondly, in this chapter we will examine the relationship of wetting length (shown in

Fig 3.4) in both a bridge-shaped system and a barrel-shaped system with respect to the

droplet volume, spacing ratio, and contact angle.
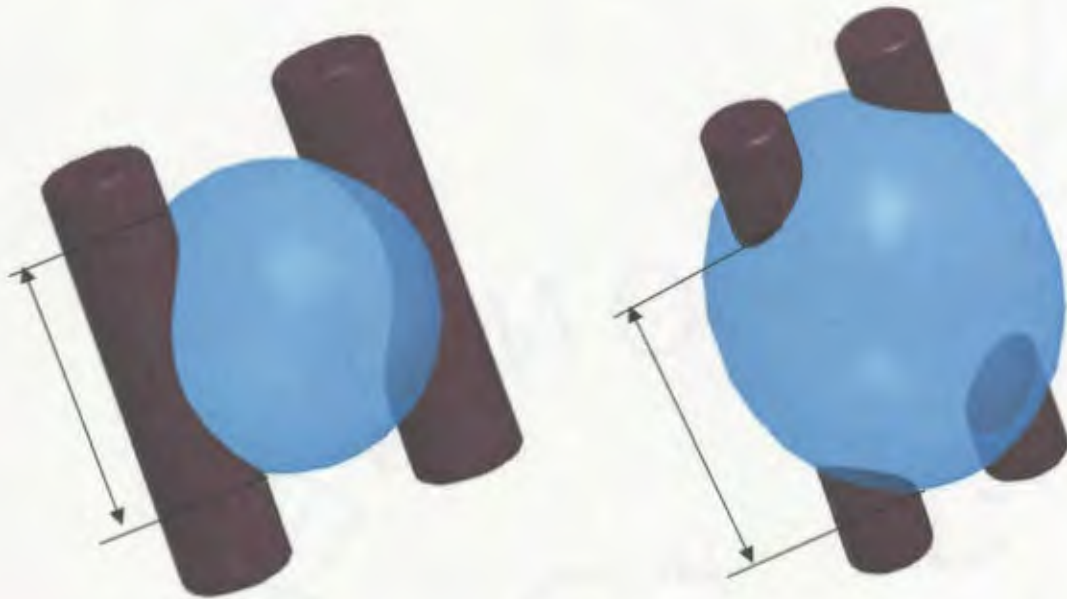
Figure 3.4: Schematic of droplet wetting length on two parallel filaments.

Recent experimental effort has been made to apply the droplet-on-filament systems to differentiate the wetting properties of human hair fibers for the purpose of hair-caring products development (Vaynberg, Stuart, & Wu, 2010). The wetting length of hair-caring liquid droplets on two parallel hair fibers was considered as a measure to differentiate the wetting properties.

3.2. Problem Formulation

A droplet sitting on two parallel filaments in the form of either a bridge-shaped morphology [Fig. 3.1 (a)] or a barrel-shaped morphology [Fig. 3.1(b)] has the total surface energy expressed by dimensional analysis (Logan, 1997):

$$\frac{\Pi}{(4\pi r^2)\gamma_{LV}} = f\left(\frac{V}{4/3\pi r^3}, \frac{D}{r}, \theta\right). \tag{3.1}$$

Here, Π (J) is the total surface energy of the system, γ_{LV} (N/m) is the surface tension of the liquid droplet (liquid-vapor interfacial tension), D (m) is the filament spacing (the distance between two filament surfaces), r (m) is the radius of the cylindrical filaments, θ is the contact angle between the droplet and the filament, and f is a dimensionless function of total surface energy with respect to the dimensionless volume $V/(4/3\pi r^3)$, spacing ratio D/r, and θ. The effect of gravity is neglected in this numerical simulation since droplet size is of the order of micron. In the above, the two fibers are assumed to carry the same diameter and surface wetting properties.

Besides, wetting length of a droplet in the same system is given by following relation:

$$\frac{L}{r} = g\left(\frac{V}{4/3\pi r^3}, \frac{D}{r}, \theta\right), \tag{3.2}$$

where g is another dimensionless function of dimensionless wetting length of the droplet with respect to the dimensionless volume $V/(4/3\pi r^3)$, spacing ratio D/r and θ. L (m) is the

wetting length of droplet. The final morphology of the system is the one that has the lowest total surface energy. Theoretically, morphology of the system under study can be determined by two basic approaches; one is by directly solving the resulting Young-Laplace equation and the second is based on minimization of the surface potential energy. In the first approach, the Laplace excess pressure, given in Chapter 2 (2.3), is constant all over the surface when equilibrium is achieved in the system. Carroll (1986) and others determined the shape of a microdroplet resting on a filament using this approach. However, when droplets come into contact with one or more complex surfaces, such as multiple fibers, the governing nonlinear partial differential equation (PDE), along with the complicated boundary conditions, becomes extremely difficult to handle, and therefore, it is almost impossible to determine the final droplet morphology by using an analytic approach. In the second approach, the total surface energy of the droplet-on-filament system is minimized through purely numerical methods. In this case, the final droplet morphology can be achievable using modern, cutting-edge, computational technologies. With the huge capability of today's computational software packages (e.g. finite element packages) and computational hardware facilities, the latter becomes more fundamental and favorable to determine the droplet morphologies. To formulate the computational problem of a droplet-on-filament system, the total surface energy of the system is given as

$$\Pi = min[\gamma_{LV}A_{LV} + (\gamma_{LV} - \gamma_{SV})A_{SL}], \qquad (3.3)$$

where γ_{LV}, γ_{LV} and γ_{SV} are the interfacial tensions of solid-liquid, liquid-air, and solid-air interfaces, respectively. A_{LV} and A_{SL} are the liquid-air and solid-liquid interfacial areas, respectively. The wetting properties are derived by the contact angle θ between the solid and liquid surface:

30

$$cos\theta = \frac{\gamma_{SV} - \gamma_{SL}}{\gamma_{LV}}. \tag{3.4}$$

Wetting of the liquid on a solid surface can be complete wetting ($\theta = 0^\circ$), partial wetting ($0^\circ < \theta < 180^\circ$), and non-wetting ($\theta = 180^\circ$). Complete wetting and non-wetting are very rare to find in real life and the most common type of wetting in nature is partial wetting, which can be further divided into two groups: hydrophilicity ($0^\circ < \theta < 90^\circ$) and hydrophobicity ($90^\circ < \theta < 180^\circ$).

3.2.1. Assumptions

- The total surface energy of the system under study is dependent only on the droplet volume, filament radius, surface tension (liquid-air), distance between two filaments, and contact angle between liquid and solid surface. The two filaments under examinations are considered to carry the same diameter and surface wetting properties.

- Final morphology of the system is considered to be the one which minimizes the total surface energy.

- When the microdroplet comes into contact with the two, cylindrical microfilaments, the droplet morphology will be either a symmetrical, bridge-shape or barrel shape, as explained earlier (Fig. 3.1).

- The critical condition of morphology transition between a bridge-shaped and a barrel-shaped morphology is reached when the total surface energies of both droplet morphologies are equal.

- Gravity and other microscopic forces can be neglected as the droplet under study is considered as microdroplet and the characteristic dimension of the droplet-on-filament system is larger than the capillary length: $l = \sqrt{\gamma_{LV}/(\rho g)}$.

3.3. Numerical Simulation

Surface finite element method through minimizing the total surface energy was adopted in this study to determine the final shape of the droplets. For this purpose, the efficient, open-source, Surface Evolver program was used, which was developed by Brakke in 1989 under the support of a grant for computational geometry from the National Science Foundation (NSF) of the United States. The software package used for this study is the newest version 2.30, released in 2008.

The Surface Evolver program is capable of determining the surface shape of liquids by minimizing the total surface energy of a system using the gradient descent method (Brakke, 2008). The user is allowed to create a data file as the input for the program, including initial dimensions of the system (initial topology), and volume and boundary constraints. An initial topology is created using a number of vertices, edges, faces, and bodies. Moreover, the user can also input energies in the form of either surface integral or knot energy, which (in combination with other energies such as surface tension, gravitational energy and square mean curvature) can calculate the total surface energy of the system. After each iteration, the program minimizes the total surface energy and modulates the shape of the system accordingly, which is then captured in the graphical user interface, as available with the code. The numerical algorithm of this program is based on a finite element approach where the user can control the meshing and iterations at every step of execution.

To validate the numerical accuracy of the Surface Evolver program, benchmark examples of barrel-shaped droplet wetting on a monofilament are first considered. In this case, radius and wetting length of the droplet have been determined in the literature (Carroll 1976). Comparison of Carroll's solutions with purely numerical results based on the Surface Evolver program is made and illustrated in Figs. 3.5 and 3.6 for two contact angles (15° and 60°). It can be observed from Figs. 3.5 and 3.6 that the relative differences based on two the methods are low (<3%) and therefore the Surface Evolver program is capable of providing reliable numerical results for the present study.
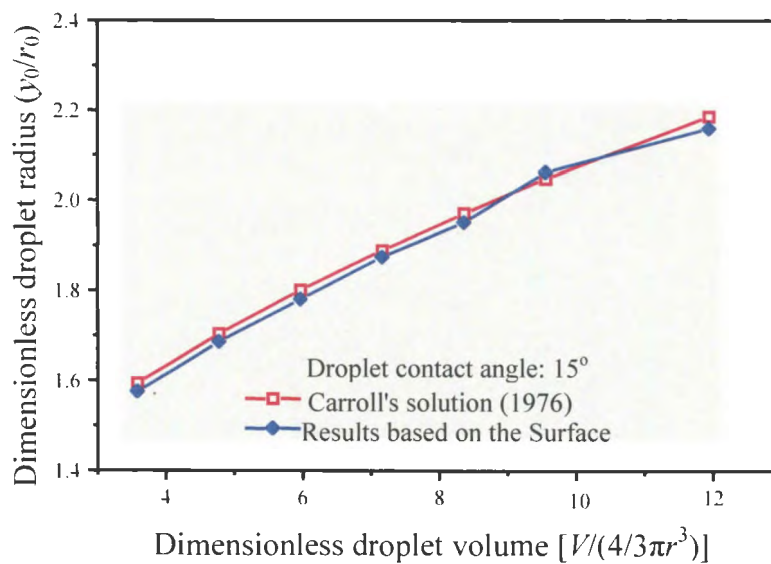
Fig. 3.5(a): Comparison between Carroll's solution (1976) and numerical results based on the Surface Evolver program: Variation of dimensionless droplet radius with varying dimensionless droplet volume (contact angle: 15°)
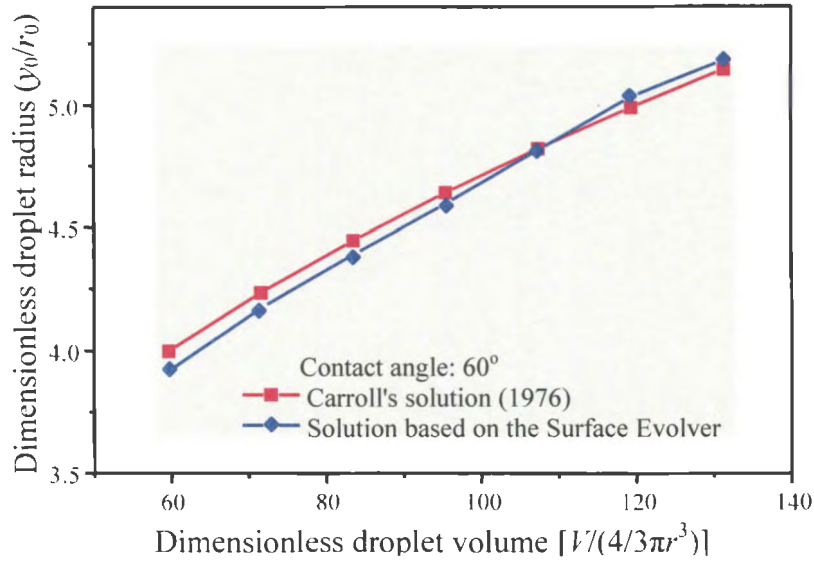
Fig. 3.5(b): Comparison between Carroll's solution (1976) and numerical results based on the Surface Evolver program: Variation of dimensionless droplet radius with varying dimensionless droplet volume (contact angle: 60°)
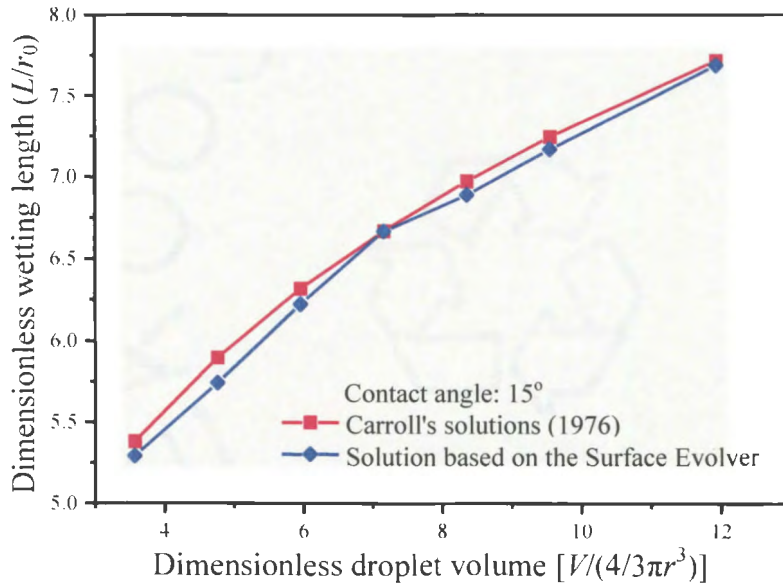
Fig. 3.6(a): Comparison between Carroll's solution (1976) and numerical results based on the Surface Evolver program: Variation of dimensionless droplet wetting length with varying dimensionless droplet volume (contact angle: 15°)
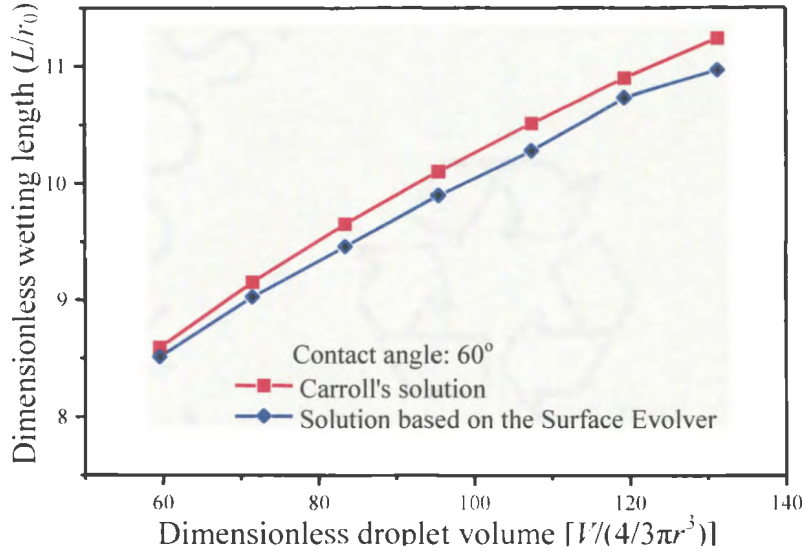
Fig. 3.6(b): Comparison between Carroll's solution (1976) and numerical results based on the Surface Evolver program: Variation of dimensionless droplet wetting length with varying dimensionless droplet volume (contact angle: 60°)

During the numerical simulation of droplets wetting on two filaments, two types of data files were created; one was for a bridge-shaped system and the other was for a barrel-shaped system. While creating data files, the constraints of the systems were loaded. A few examples to show how to implement the constraints are listed in Appendices.

1. Surfaces where the filament is in contact with the droplet are constrained by equation $x^2 + y^2 = R^2$ with R as the radius of filament. Moreover, the interfacial energy of the liquid with the filament is compensated by an edge integral over the edges where the liquid surface meets the filament.

$$E = \iint_S -T\cos\theta\, dA = -T\cos\theta \int_{\partial S} z\, ds = T\cos\theta \int_{\partial S} \frac{z}{R}(y\vec{i} - x\vec{j})d\vec{s}, \qquad (3.5)$$

where, S is the fiber surface, T is the surface tension of the liquid, and θ is the internal contact angle. This energy is included as the part of constraints in respective direction, which is applied on the cylindrical surface.

2. The constraint named 'nonnegative' is used to keep the computational vertices outside the cylindrical surface of filaments. When the contact angle is around 180° or the liquid droplet volume is large, the liquid will try to invade the cylindrical boundary. A nonnegative constraint ensures that the liquid will remain outside the filament boundary. Nonnegative constraints can be applied to any vertex, edge, or face trying an incursion on the fiber surface.

3. When dealing with curved surfaces such as the filament surface, the Surface Evolver program often splits the edges in a singular manner, as elongated edges with minimum partitions can utilize less energy. The new constraint has been employed to distribute the edges uniformly by splitting up every single edge into two identical halves when a special refinement command is adopted in runtime. This constraint uses a real algebraic module function with an arctangent to create a periodic constraint. a specific refinement command is listed at the end of the data file.

After creating the data file with proper constraints and boundary conditions, the data file can be executed by a regular command prompt. With every 'go' command, the program minimizes the total surface energy of the system and shows the value in the command prompt window, while the graphical output is shown in the graphical user interface. To accelerate the numerical process and simultaneously maintain high numerical stability in the program, 1/8-models of both the bridge-shaped system and the barrel-shaped system were utilized. Thus, the total surface energy obtained in each simulation is 1/8 of the

surface energy of the complete model. Meshing is controlled throughout the execution of data file. These models are shown in Figs 3.7 and 3.8.

<div align="center">(a)</div>

<div align="center">(b)</div>

<div align="center">(c)</div>

<div align="center">(d)</div>
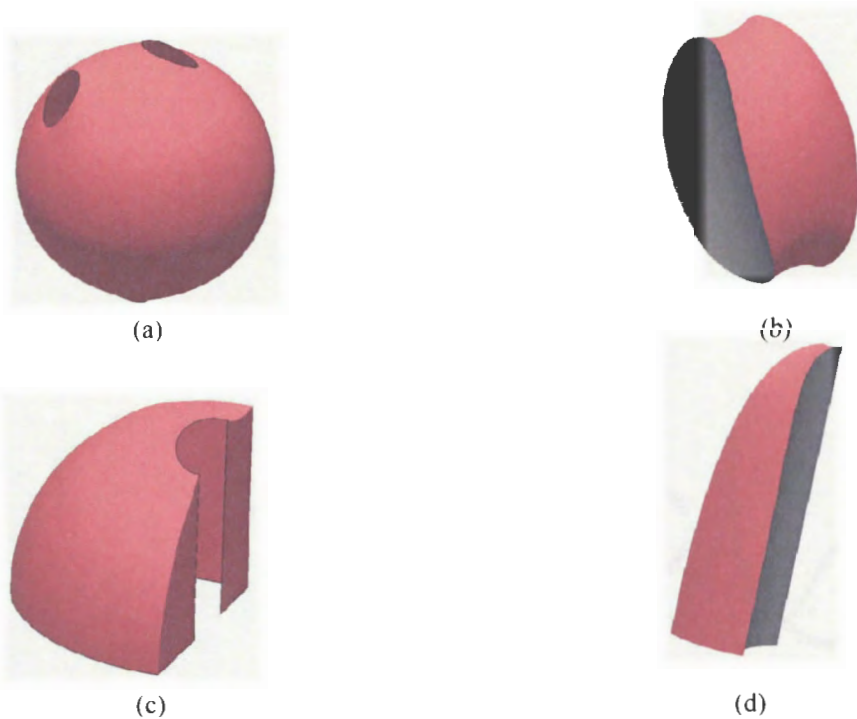
Figure 3.7: Graphical outputs after execution of data files: (a) Full model of a barrel-shaped system; (b) full model of a bridge-shaped system; (c) 1/8 model of a barrel-shaped system; and (d) 1/8-model of a bridge-shaped system

3.3.1. Morphology transition

While performing numerical simulations for examination of the morphology transition, two data files were created with the same parameters; surface energies of both the barrel-shaped system and bridge-shaped system were calculated by varying the droplet volume. The volume at which the surface energies of both systems are equal is considered the transition point and the corresponding volume is considered the critical droplet volume. Simulation was carried out with all possible combinations of different spacing ratios (D/r) and contact angle (θ). In the simulation, five spacing ratios (1, 2, 4, 8, & 12) and three

<div align="center">37</div>

contact angles (30°, 90°, & 120°) were selected. A number of data points corresponding to the critical droplet volume for each combination of spacing ratio and contact angle were obtained; these points are plotted against the spacing ratio for varying contact angles. These curves are called as wetting characteristic curves (*W*-curves).
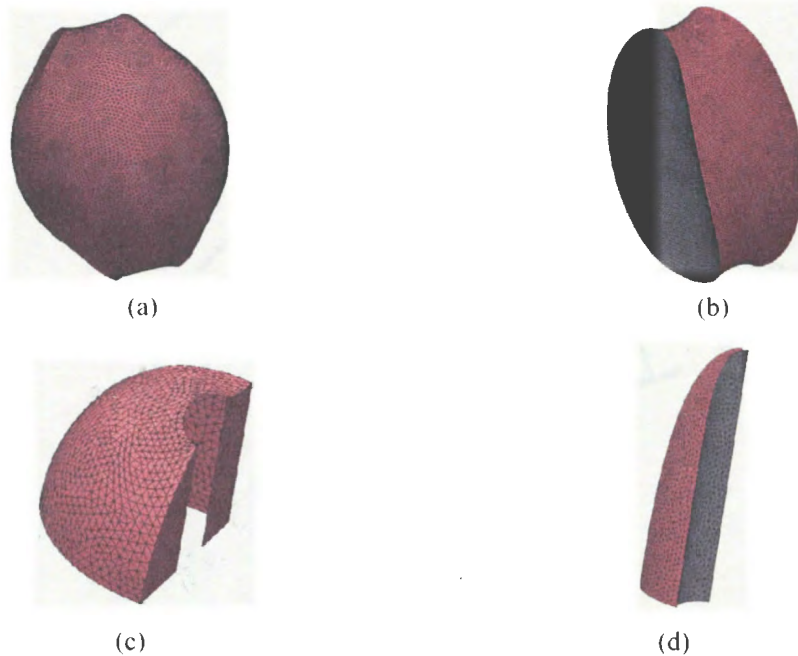
Figure 3.8: Meshing qualities were achieved while running the data files: (a) Full model of a barrel-shaped system; (b) full model of a bridge-shaped system; (c) 1/8- model of a barrel-shaped system; and (d) 1/8- model of a bridge-shaped system.

3.3.2. *Wetting length behavior*

In this simulation, 1/8-models of both the systems were adopted and dimensionless wetting length *(L/r)* was calculated for different combinations of dimensionless volumes $[V/(4/3\pi r^3)]$, spacing ratios *(D/r)*, and contact angles *(θ)*. In the simulations, three spacing ratios: 1, 2 and 3; and five contact angles: 30°, 60°, 90°, 120°, and 150° were used; two droplet volumes: 15 and 30 were used for the bridge-shaped systems, while two droplet volumes: 250 and 400 were used for the barrel-shaped systems. The reason for selecting

38

different volumes is because at low droplet volumes, a bridge-shaped system is a more stable morphology; while at high droplet volume, a barrel-shaped system is a more stable morphology. These points were plotted graphically to examine the wetting length behavior on these system parameters.

3.4. Results and Discussion

3.4.1. Morphology transition

Figs. 3.9 to 3.11 show that dimensionless surface energies of both the bridge-shaped and barrel-shaped systems increase with increasing dimensionless droplet volume. The surface energies become equal for both the morphologies at the critical droplet volume where morphology transition occurs. Numerical results are shown in Figs. 3.9 to 3.11 for different contact angles and spacing ratios between the two filaments. For the volume below the critical droplet volume, the total surface energy of a bridge-shaped system is less than that of a barrel-shaped system with the same parameters, whereas for the droplet volume beyond this value, the total surface energy of a barrel-shaped system is less than that of a bridge-shaped system carrying the same parameters. In nature, microfluidic systems always tends to minimize the total surface energy by achieving a favorable shape; therefore, it can be concluded that as the droplet volume increases, the droplet morphology transforms from a bridge-shaped system to a barrel-shaped system at the critical droplet volume.

From this discussion, it can be stipulated that the dimensionless critical droplet volume $[V_0/(4/3\pi r^3)]$ is a dimensionless function of the filament spacing ratio (D/r) and the contact angle (θ), so that

$$V_0 = w\left(\frac{D}{r}, \theta\right). \tag{3.6}$$

$8 \times U / (4\pi r^2 \gamma)$

Contact angle: θ=30°
Spacing ratio: D/r=1.0

▼ Droplet-bridge
▲ Barrel-shaped droplet

Transition point: (17.01, 2.09)

Dimensionless droplet volume $[8 \times V / (\frac{4}{3}\pi r^3)]$

(a)

$8 \times U / (4\pi r^2 \gamma)$

Contact angle: θ=30°
Spacing ratio: D/r=2.0

▼ Droplet-bridge
▲ Barrel-shaped droplet

Transition point: (18.95, 2.35)

Dimensionless droplet volume $[8 \times V / (\frac{4}{3}\pi r^3)]$

(b)
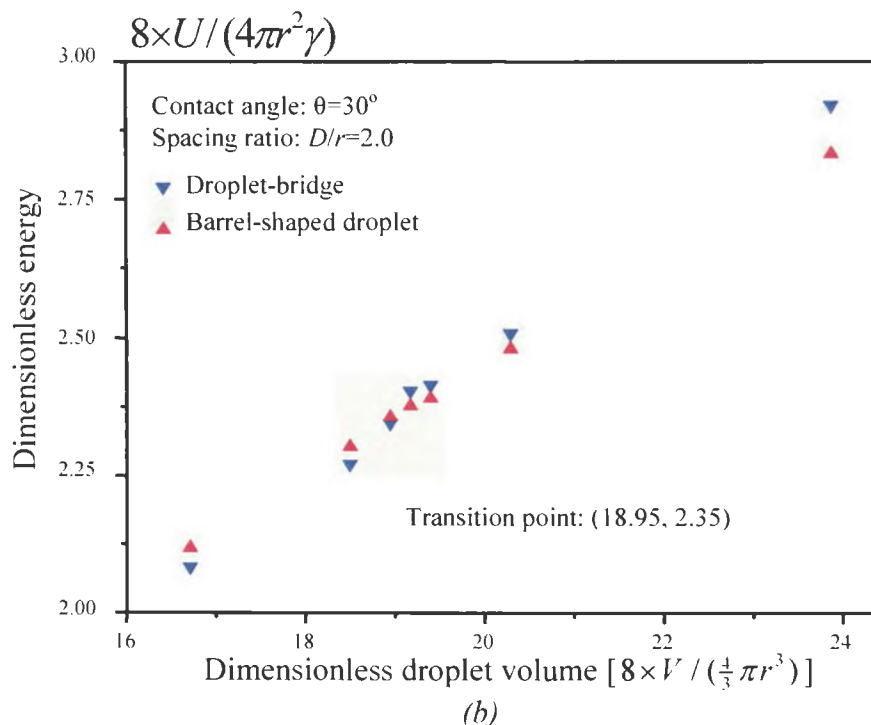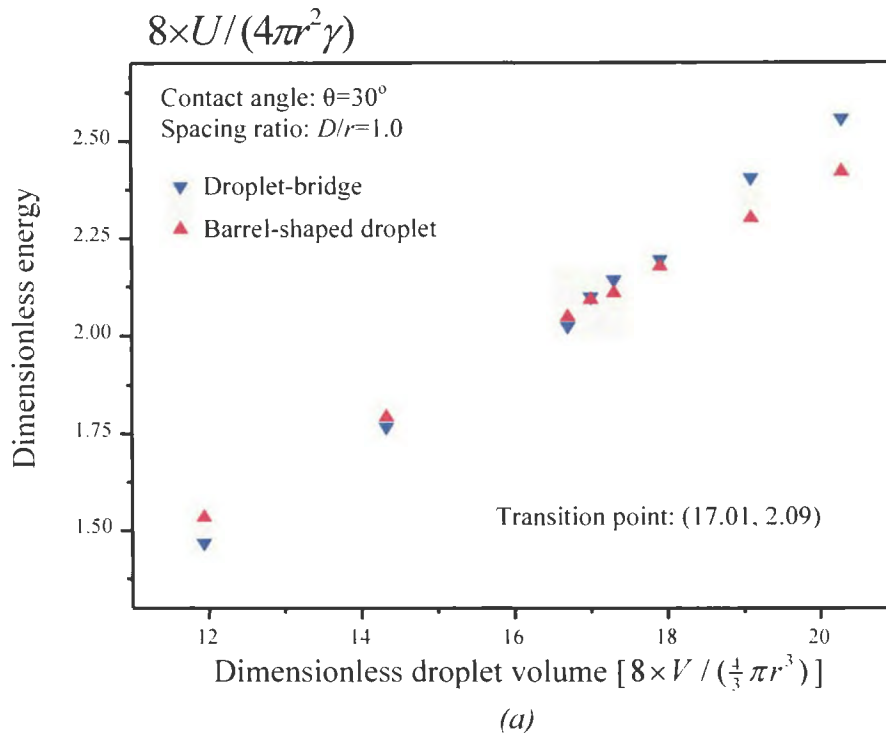
Figure 3.9(a): Variation of the dimensionless droplet surface energy vs. the dimensionless droplet volume for droplet-bridges and barrel-shaped droplets at contact angle θ=30° and varying filament spacing ratio: (a) D/r=1 and (b) D/r=2. (Wu, Bedarkar & Vaynberg, 2010)

40

$8 \times U / (4\pi r^2 \gamma)$

(c)

$8 \times U / (4\pi r^2 \gamma)$

(d)

Figure 3.9(b): Variation of the dimensionless droplet surface energy vs. the dimensionless droplet volume for droplet-bridges and barrel-shaped droplets at contact angle $\theta = 30°$ and varying filament spacing ratio: (c) $D/r = 4$ and (d) $D/r = 8$. (Wu, Bedarkar & Vaynberg, 2010)

41
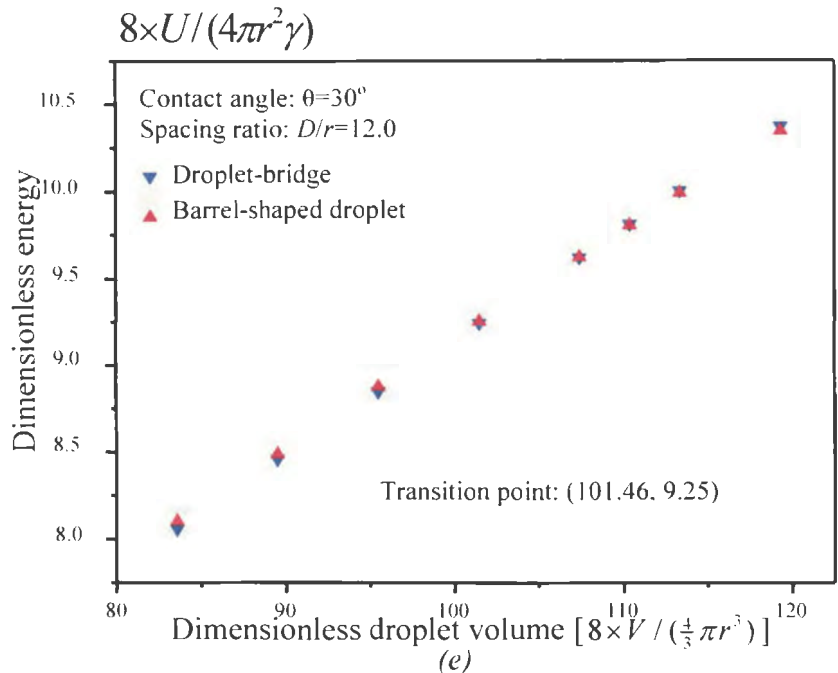
Figure 3.9(c): Variation of the dimensionless droplet surface energy vs. the dimensionless droplet volume for droplet-bridges and barrel-shaped droplets at contact angle θ=30° and varying filament spacing ratio: (e) D/r=12. (Wu, Bedarkar & Vaynberg, 2010)
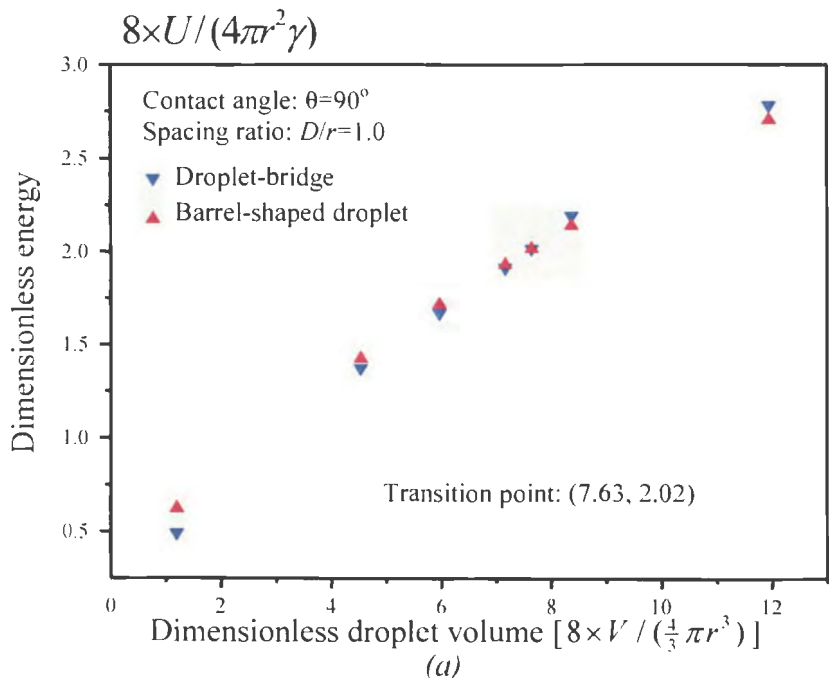
Figure 3.10(a): Variation of the dimensionless droplet surface energy vs. the dimensionless droplet volume for droplet-bridges and barrel-shaped droplets at contact angle θ=90° and varying filament spacing ratio: (a) D/r=1. (Wu, Bedarkar & Vaynberg, 2010)

(b)

(c)
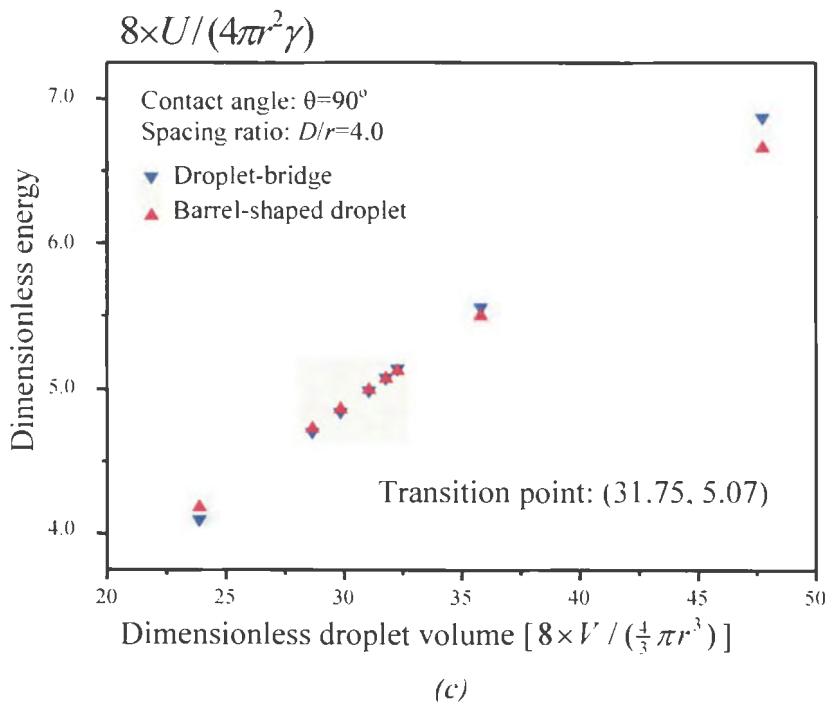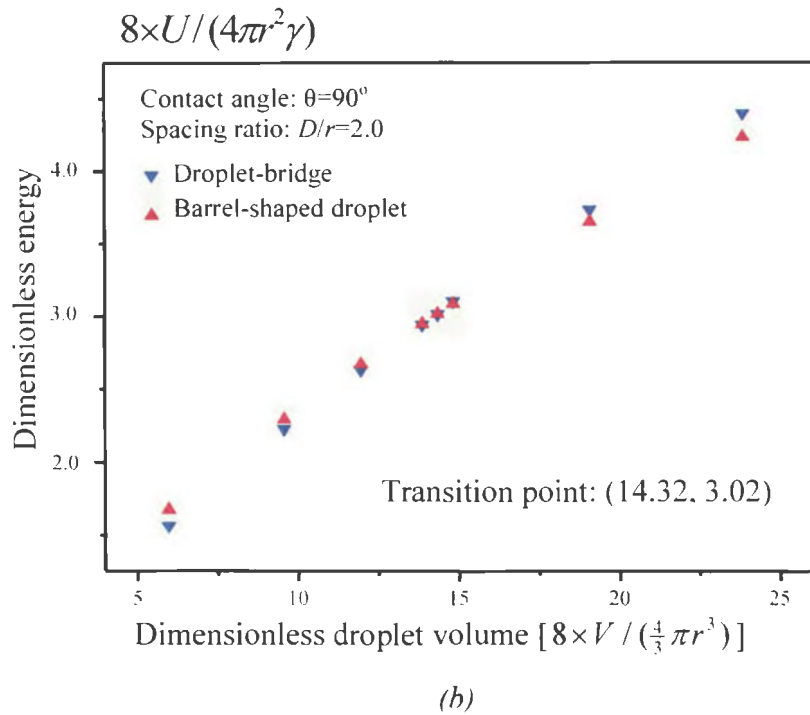
Figure 3.10(b): Variation of the dimensionless droplet surface energy vs. the dimensionless droplet volume for droplet-bridges and barrel-shaped droplets at contact angle θ=90° and varying filament spacing ratio: (b) D/r=2 and (c) D/r=4 (Wu, Bedarkar & Vaynberg, 2010)

43

$8 \times U / (4\pi r^2 \gamma)$

Contact angle: θ=90°
Spacing ratio: D/r=8.0

▼ Droplet-bridge
▲ Barrel-shaped droplet

Transition point: (92.39, 10.25)

Dimensionless energy

Dimensionless droplet volume [$8 \times V / (\frac{4}{3}\pi r^3)$]

$8 \times U / (4\pi r^2 \gamma)$ *(d)*

Contact angle: θ=90°
Spacing ratio: D/r=12.0

▼ Droplet-bridge
▲ Barrel-shaped droplet

Transition point: (186.93, 16.35)

Dimensionless energy

Dimensionless droplet volume [$8 \times V / (\frac{4}{3}\pi r^3)$]
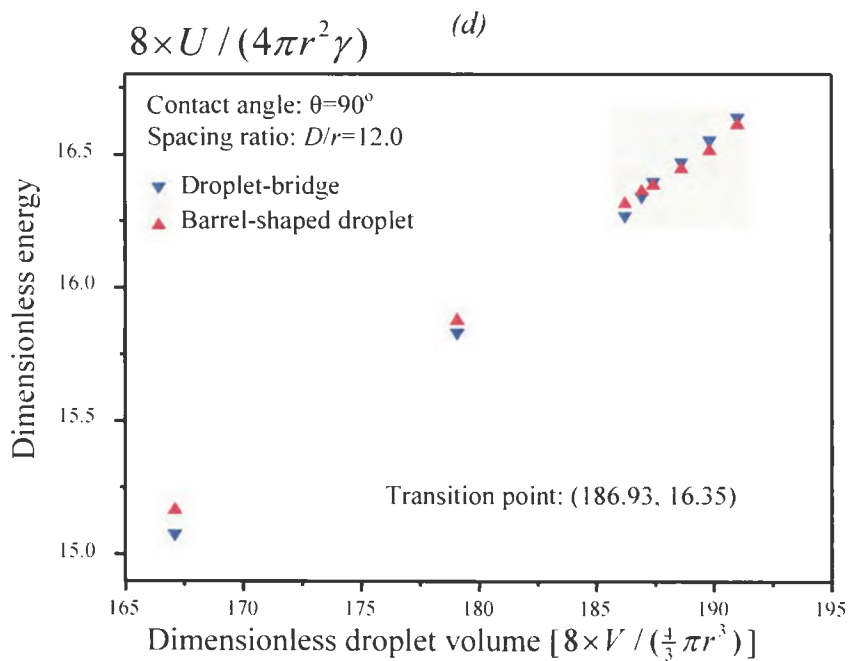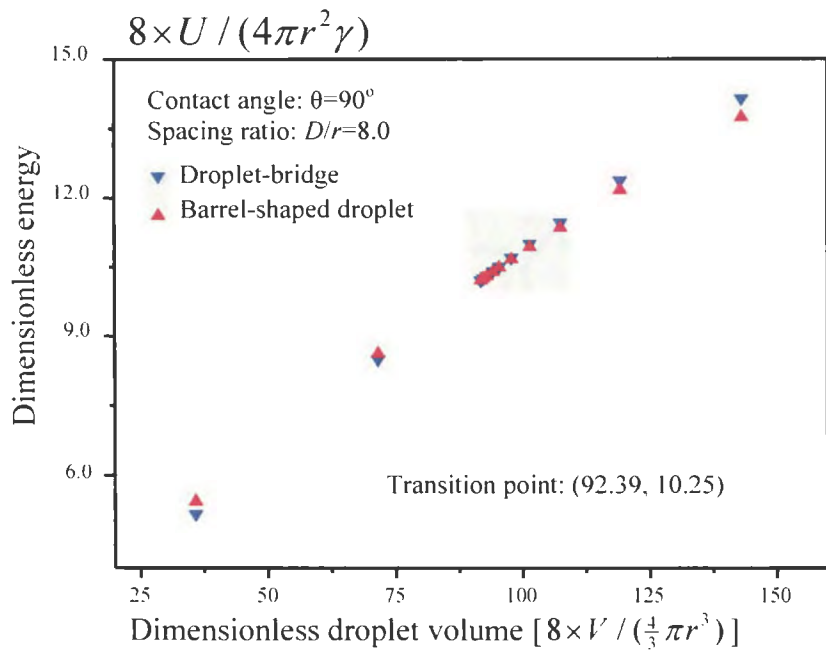
(e)

Figure 3.10(c): Variation of the dimensionless droplet surface energy vs. the dimensionless droplet volume for droplet-bridges and barrel-shaped droplets at contact angle θ=90° and varying filament spacing ratio: (d) D/r=8 and (e) D/r=12 (Wu, Bedarkar & Vaynberg, 2010)

$8 \times U / (4\pi r^2 \gamma)$

Contact angle: $\theta = 120°$
Spacing ratio: $D/r = 1.0$

▼ Droplet-bridge
▲ Barrel-shaped droplet

Transition point: (13.13, 3.33)

Dimensionless energy

Dimensionless droplet volume $[\, 8 \times V / (\tfrac{4}{3}\pi r^3)\,]$

(a)

$8 \times U / (4\pi r^2 \gamma)$

Contact angle: $\theta = 120°$
Spacing ratio: $D/r = 2.0$

▼ Droplet-bridge
▲ Barrel-shaped droplet

Transition point: (18.62, 4.12)

Dimensionless energy

Dimensionless droplet volume $[\, 8 \times V / (\tfrac{4}{3}\pi r^3)\,]$
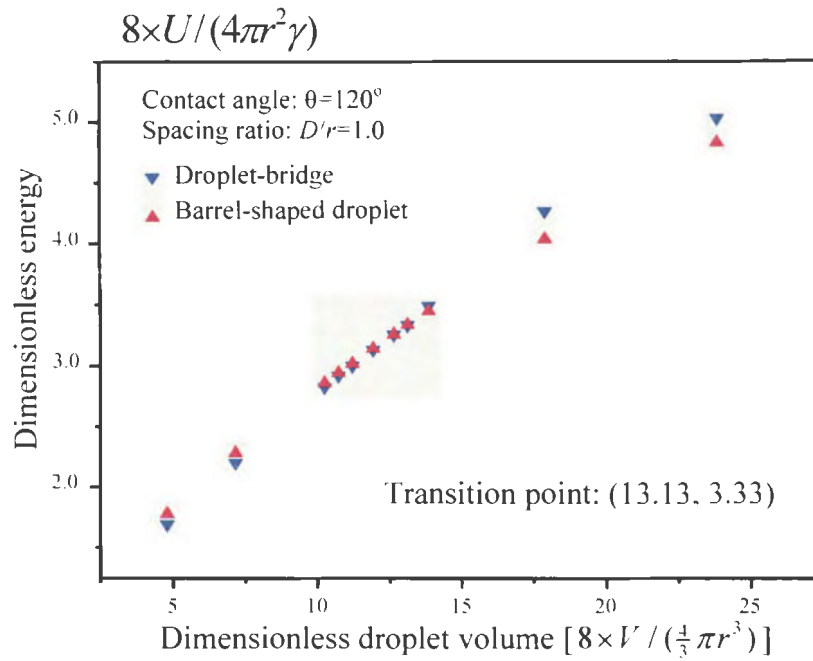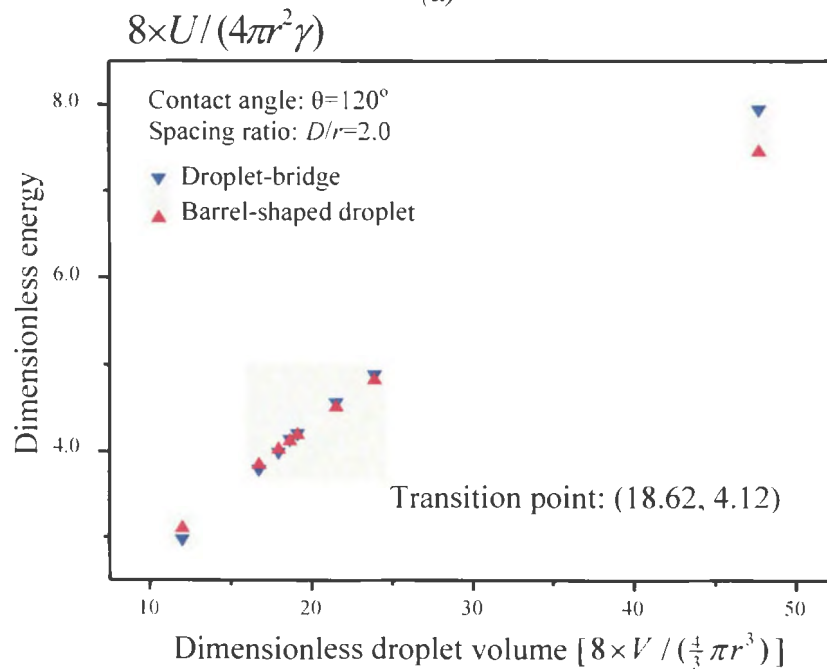
(b)

Figure 3.11(a): Variation of the dimensionless droplet surface energy vs. the dimensionless droplet volume for droplet-bridges and barrel-shaped droplets at contact angle $\theta = 120°$ and varying filament spacing ratio: (a) D/r=1 and (b) D/r=2 (Wu, Bedarkar & Vaynberg, 2010)

45

$$8 \times U / (4\pi r^2 \gamma)$$

Dimensionless energy

Contact angle: θ=120°
Spacing ratio: D/r=4.0
▼ Droplet-bridge
▲ Barrel-shaped droplet

Transition point: (45.36, 7.14)

Dimensionless droplet volume $[8 \times V / (\frac{4}{3} \pi r^3)]$

(c)

$$8 \times U / (4\pi r^2 \gamma)$$

Dimensionless energy

Contact angle: θ=120°
Spacing ratio: D/r=8.0
▼ Droplet-bridge
▲ Barrel-shaped droplet

Transition point: (126.05, 13.59)

Dimensionless droplet volume $[8 \times V / (\frac{4}{3} \pi r^3)]$
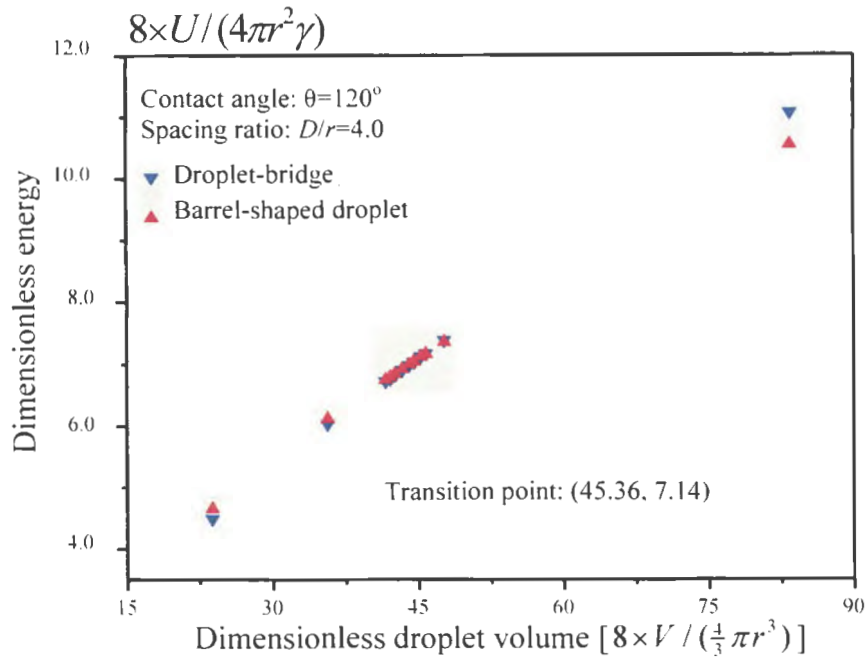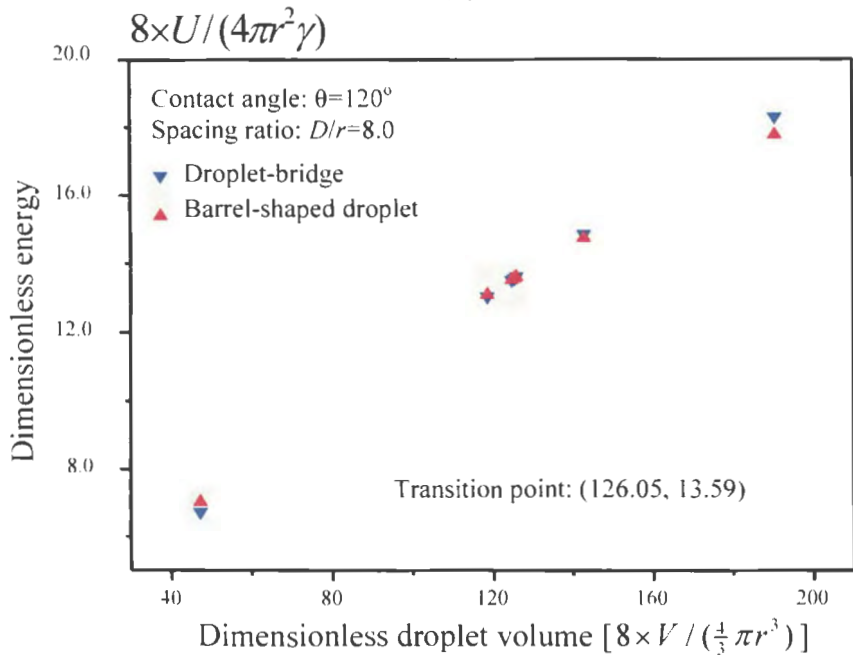
(d)

Figure 3.11(b): Variation of the dimensionless droplet surface energy vs. the dimensionless droplet volume for droplet-bridges and barrel-shaped droplets at contact angle θ=120° and varying filament spacing ratio: (c) D/r=4 and (d) D/r=8 (Wu, Bedarkar & Vaynberg, 2010)

46

$8 \times U / (4\pi r^2 \gamma)$

Contact angle: $\theta = 120°$
Spacing ratio: $D/r = 12.0$

▼ Droplet-bridge
▲ Barrel-shaped droplet

Transition point: (122.23, 13.60)

23.0

22.0

21.0

20.0

Dimensionless energy

230   240   250   260   270   280   290

Dimensionless droplet volume $[8 \times V / (\frac{4}{3}\pi r^3)]$
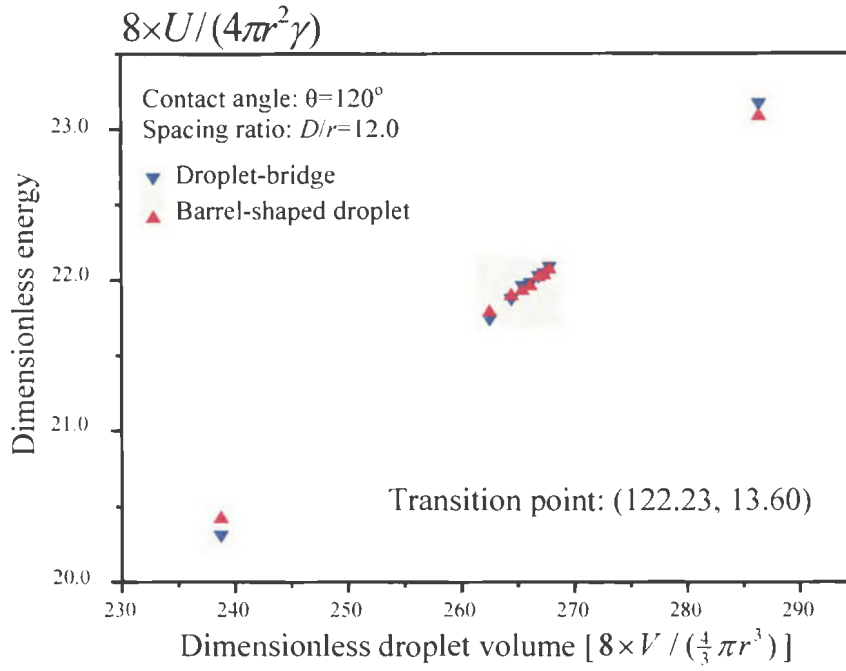
(e)

Figure 3.11(c): Variation of the dimensionless droplet surface energy vs. the dimensionless droplet volume for droplet-bridges and barrel-shaped droplets at contact angle $\theta = 120°$ and varying filament spacing ratio: (e) D/r=12. (Wu, Bedarkar & Vaynberg, 2010)

Based on the results obtained from the numerical analysis, a family of wetting characteristic curves can be plotted, as shown in Fig. 3.12, which can be called as *W*-curves as a function of the spacing ratio and the contact angle. It is observed from Fig. 3.12 that as the filament spacing ratio (more than 3) or the contact angle increases, the critical droplet volume required for morphology transition increases rapidly. In other words, when the distance between two fibers is larger or the droplets behave more hydrophobic, the droplet volume required to entirely wrap the two filaments becomes larger. Thus, the obtained results are in accordance with the physical senses.
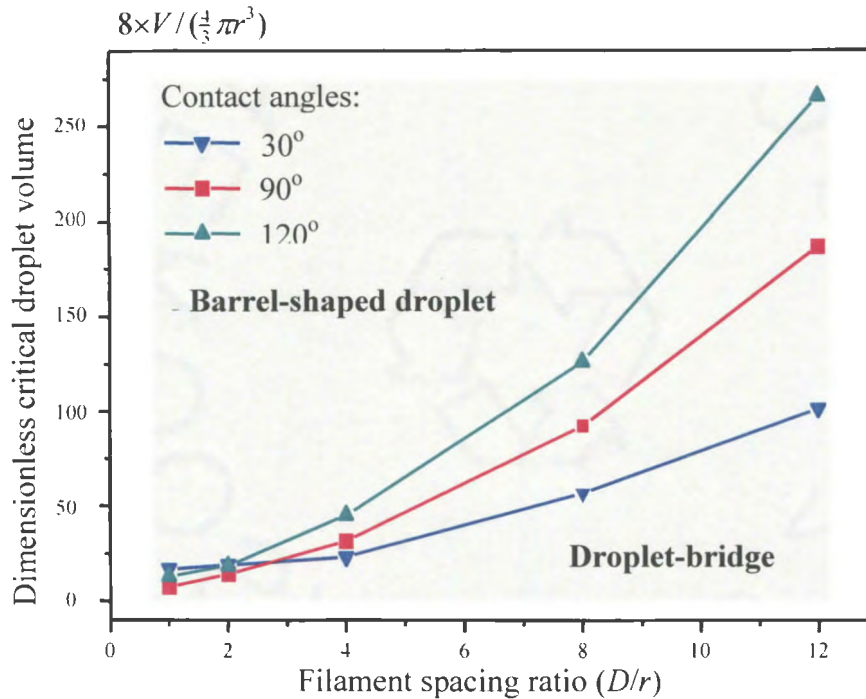
Figure 3.12: Variations of the dimensionless critical droplet volume for morphology transition vs. the filament spacing ratio at three contact angles θ=30°, 90° and 120°. Each wetting characteristic curve (W-curve) divides the (D/r, V_0)-domain into the barrel-shaped droplet region and droplet-bridge region (Wu, Bedarkar & Vaynberg, 2010)

Nevertheless, when the spacing ratio is less (< 3), the curves for different contact angles overlap. This is because at a low spacing distance, the capillary effect will yield a much larger wetting length, which further increases the requirement of droplet volume to cover both the filaments in order to keep a barrel-shaped morphology. In summary, a wetting characteristic curve can be considered as a universal law of droplets wetting on filament rails at a given contact angle. Such a curve divides the region into two domains: the upper corresponds to the barrel-shaped droplet region, while the lower corresponds to the bridge-shaped droplet region (Wu, Bedarkar & Vaynberg, 2010).

3.4.2. Wetting length behavior

Numerical results obtained from detailed analysis by using the Surface Evolver software package are plotted in Fig. 3.13. In Figs. 3.13(a) and 3.13(b), the wetting lengths of bridge shaped systems with a lower droplet volume are plotted with respect to the contact angle at three spacing ratios (D/r=1, 2, 3). It can be found that the wetting length decreases as the contact angle increases. For a small contact angle or a hydrophilic system, the liquid spreads over a larger surface area on the filaments, which increases the wetting length of the structure. Moreover, it can be observed that at a higher the spacing ratio, the wetting length does not have a significant variation with respect to the contact angle; while for a lower spacing ratio, the wetting length exhibits more sensitivity to the contact angle. This sensitivity becomes more pronounced by decreasing the spacing ratio, because the capillary effect becomes dominant at a small distance between two filaments.
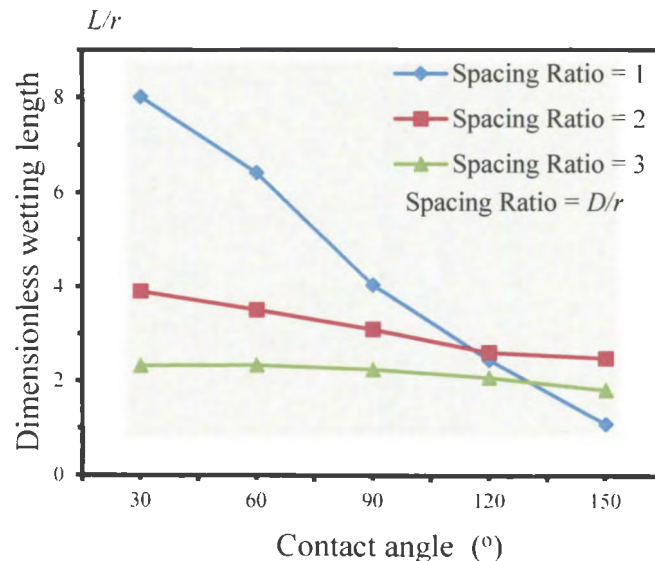
Figure 3.13(a): Variation of the wetting length vs. the contact angle for bridge-shaped systems with dimensionless volume $[V/(4/3\pi r^3)] = 15$. (Bedarkar, Wu & Vaynberg, under review)

49
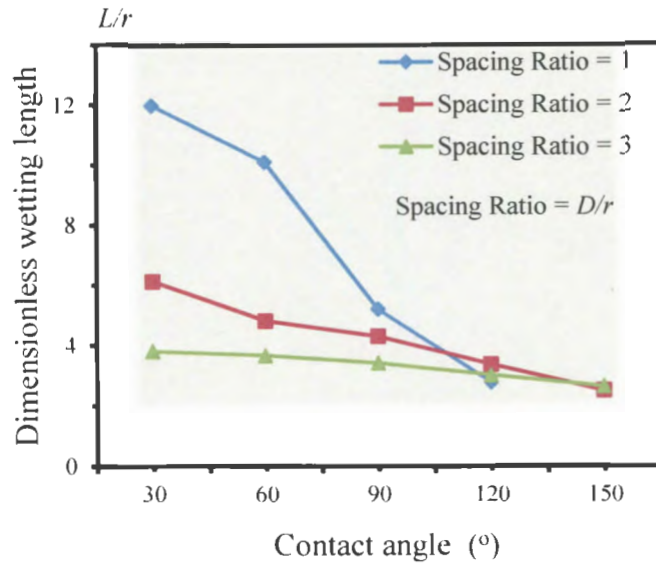
Figure 3.13(b): Variation of the wetting length vs. the contact angle for bridge-shaped systems with dimensionless volume $(V/4/3\pi r^3) = 30$. (Bedarkar, Wu & Vaynberg, under review)
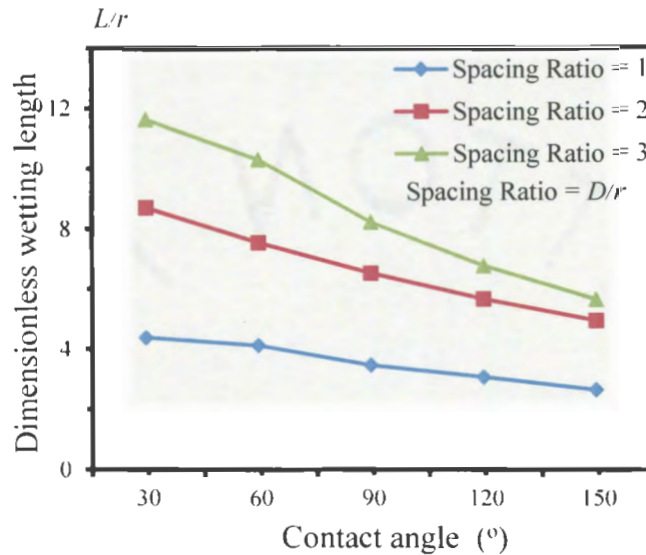
Figure 3.13(c): Variation of the wetting length vs. the contact angle for barrel-shaped systems with dimensionless volume $[V/(4/3\pi r^3)] = 250$. (Bedarkar, Wu & Vaynberg, under review)
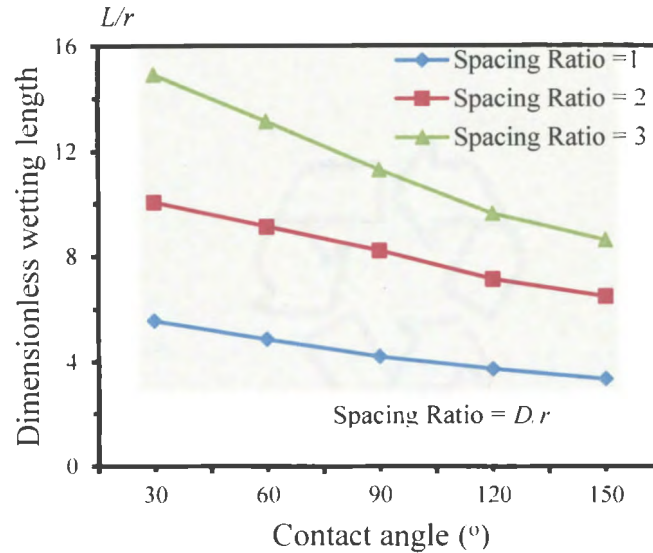
Figure 3.13(d): Variation of the wetting length vs. the contact angle for barrel-shaped systems with dimensionless volume [V/(4/3πr³)] = 400. (Bedarkar, Wu & Vaynberg, under review)

In Figs. 3.13(c) and 3.13(d), the wetting lengths of barrel-shaped systems with a high droplet volume are plotted against the contact angle at three spacing ratios (D/r=1,2, 3). It can be observed that the wetting lengths have nearly linear relationships with respect to the contact angle at three spacing ratios. The wetting length increases with growing spacing ratio, while it decreases with the increase of the contact angle.

3.5. Summary

In the first part of this chapter, criteria for morphology transition between a bridge-shaped morphology and a barrel-shaped morphology is determined. The critical droplet volume at which the morphology transition occurs is the one corresponding to the total surface energies of both morphologies with the same value at identical system parameters, including contact angle, spacing ratio, radius of filament, and liquid-air surface tension.

51

Furthermore, these values were plotted against the spacing ratio at varying contact angles to obtain the wetting characteristic curves. These curves define the boundaries of morphology transition when two parallel filaments are in contact with liquid droplets. Study performed herein has practical applications in the field including the analysis and design of microfluidic devices and testers based on droplet-on-filament systems, among others.

In the second part, the study was concentrated on the wetting length in similar droplet-on-filament systems. Numerical analysis was conducted to calculate the wetting length of both bridge-shaped and barrel-shaped systems with appropriate droplet volume by varying spacing ratio and contact angle. Results were plotted with respect to contact angle for different spacing ratios.

CHAPTER 4. CAPILLARY TORQUE IN A LIQUID BRIDGE

BETWEEN TWO ANGLED FILAMENTS

The principle of minimum potential energy is the fundamental law in nature that every system obeys. When a stable system is disturbed due to any external reason, the system naturally tends to achieve it back by exerting opposite potential forces. To minimize its potential energy, a symmetric liquid bridge can be formed between two parallel, identical filaments wetted by a small, liquid droplet. The symmetry of the droplet bridge will be broken when the two filaments form a small, spatial angle. As a result, the potential energy of this disturbed system is enhanced, and an internal potential force (e.g. a capillary torque) exists and tends to push the system back into the initial symmetric state.

This chapter will examine the variation of such a capillary torque with the filament orientation angle, contact angle, liquid droplet volume, and filament spacing.

4.1. Introduction

In the preceding chapter, we have discussed about morphology transition and wetting length behavior in droplet-on-filament systems made of two parallel, identical filaments wetting with a droplet in the form of either a barrel-shaped or bridge-shaped morphology. What will happen if the two filaments are tilted at a certain angle? This is a common situation in nature as well as in engineering, such as wetting of spider webs by dews, welding of microelectronic components, wetting of fabrics by resins, etc. When the droplet volume is below the critical droplet volume (as interpreted in Chapter 3), it forms a bridge-shaped droplet. Fig. 4.1 illustrates a few examples of a liquid bridge forming between two

angled filaments. Physical intuition indicates that the capillary torque is zero when the filament orientation angle is zero (i.e. two parallel filaments), and the capillary torque may increase as the filament orientation angle increases up to a certain peak value and then starts decreasing down to zero again at 90°. This states that two trivial filament orientation conditions exist where no capillary toque is triggered. In this study, numerical simulations were performed within the range of 0° to 90° by using the Surface Evolver software package.
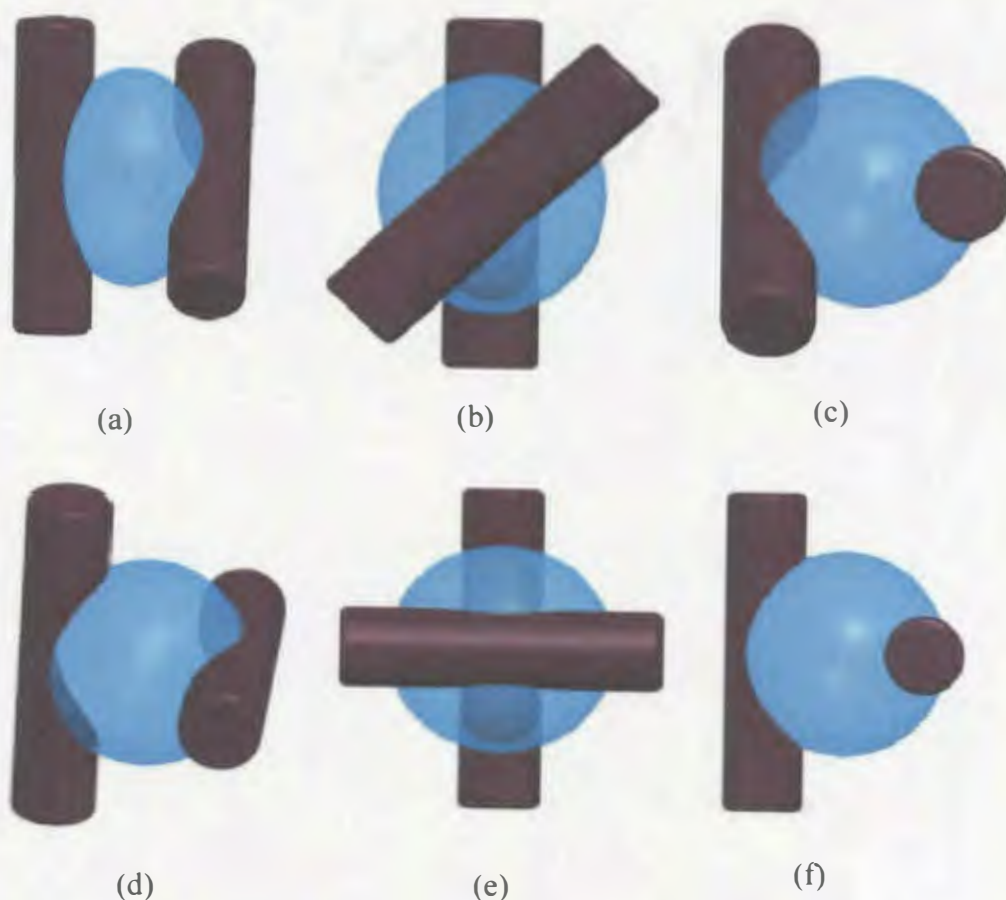
Figure 4.1: Bridge-shaped droplet-on-filament systems made of two misaligned microfilaments. (a)Isometric view with orientation angle 45°, (b) front view with orientation angle 45°, (c) top view with orientation angle 45°, (d) isometric view with orientation angle 90°, (e) front view with orientation angle 90°, and (f) top view with orientation angle 90°. (Images drawn in ProE wildfire 4.0)

54

4.2. Problem Formulation

For the droplet-on-filament system under study, when the two misaligned microfilaments come into contact with a small, liquid droplet, it forms a bridge-shaped droplet; scaling analysis indicates the total surface energy can be expressed as

$$\frac{\Pi}{(4\pi r^2)\gamma_{LV}} = f\left(\frac{V}{4/3\pi r^3}, \frac{D}{r}, \theta, \varphi\right),\tag{4.1}$$

where Π (J) is the total surface energy of the system, γ_{LV} (N/m) is the liquid-air interfacial tension, D (m) is the distance between the two filaments (i.e., the minimum distance between the two filament surfaces under consideration), r (m) is the radius of the two identical cylindrical filaments of the circular cross section, θ is the contact angle between the liquid and filament surface, and φ is the orientation angle between the two filaments. Dimensionless variables have been adopted in this analysis for ease of understanding. Herein, f is a dimensionless function with respect to the dimensionless volume $V/(4/3\pi r^3)$, dimensionless spacing ratio D/r, contact angle θ, and orientation angle φ.

The capillary torque can be determined by differentiating surface potential energy [i.e. in Eq. (4.1)] with respect to the orientation angle φ (radians):

$$\frac{T}{(4\pi r^2)\gamma_{LV}} = \frac{d\Pi}{(4\pi r^2)\gamma_{LV}} = \frac{df\left(\frac{V}{4/3\pi r^3}, \frac{D}{r}, \theta, \varphi\right)}{d\varphi}.\tag{4.2}$$

4.3. Numerical Simulation

The morphology of a droplet-on-filament system at equilibrium is the one which minimizes the total surface energy of the system. Theoretically, the morphology of such a system can be determined by directly solving the resulting Young-Laplace equation; however it is extremely difficult to find an explicit mathematical solution due to the

complexity of the system, even in the two trivial cases, with the orientation angle at either 0° or 90°. For this reason, the efficient, powerful Surface Evolver software package was further utilized to search for actual droplet morphology and related surface energy at the equilibrium state. This surface energy is further used to calculate the capillary torque induced by a misaligned, liquid bridge based on Eq. (4.2). In the numerical process, the filament radius r is fixed as the reference length and the surface tension of droplet γ_{LV} is considered as unit. Two contact angles ($\theta = 30°$ and $60°$), two filament spacing ratios ($D/r = 0.5$ and 1), and two dimensionless droplet volumes ($V= 2$ and 5) were selected, respectively, to explore the influence of these variables on the capillary torque. To calculate the capillary torque at a particular orientation angle, two surface energies were calculated respectively with $0.25°$ less and more than the specific orientation angle under consideration. Numerical differentiation of the potential energy is the capillary torque exerted at that orientation angle:

$$\frac{Tl_{\varphi=\varphi_0}}{(4\pi r^2)\gamma_{LV}} = \frac{\Pi\left[\frac{V}{4/3\pi r^3}, \frac{D}{r}, \theta, (\varphi + \Delta\varphi)\right] - \Pi\left[\frac{V}{4/3\pi r^3}, \frac{D}{r}, \theta, (\varphi - \Delta\varphi)\right]}{(4\pi r^2)\gamma_{LV}(2\Delta\varphi)} , \quad (4.3)$$

where φ is varied from $10°$ to $80°$ with an interval of $10°$. The corresponding capillary torque for each orientation angle is calculated by using a central difference scheme where $\Delta\varphi = 0.25° = 1.3889*10^{-3}\pi$ (radians) is the incremental angular step used in the calculation.

The data file of two angled filaments was generated from the data file used for two parallel filaments in Chapter 2, in which the rotation of one filament, with respect to the other was considered. The orientation angle, as a new system parameter, was incorporated into the data file and all vertices attached onto the rotated filament were transformed accordingly. For the purpose of generalization, a transformation matrix was used to

transform the coordinates of vertices in a rotated coordinate system. This transformation matrix for a clockwise rotation is given as

$$[T] = \begin{bmatrix} cos\varphi & sin\varphi \\ -sin\varphi & cos\varphi \end{bmatrix} \tag{4.4}$$

After a clockwise rotation of one of the filaments, coordinates of vertices attached to this filament are given such that

$$\begin{bmatrix} Y \\ Z \end{bmatrix} = \begin{bmatrix} cos\varphi & sin\varphi \\ -sin\varphi & cos\varphi \end{bmatrix} \cdot \begin{bmatrix} y \\ z \end{bmatrix} \tag{4.5}$$

The data file generated to solve this problem is attached in Appendix.

Typical droplet morphologies captured after executing the data files are shown in Fig 4.2.

(a)   (b)   (c)

(d)   (e)   (f)
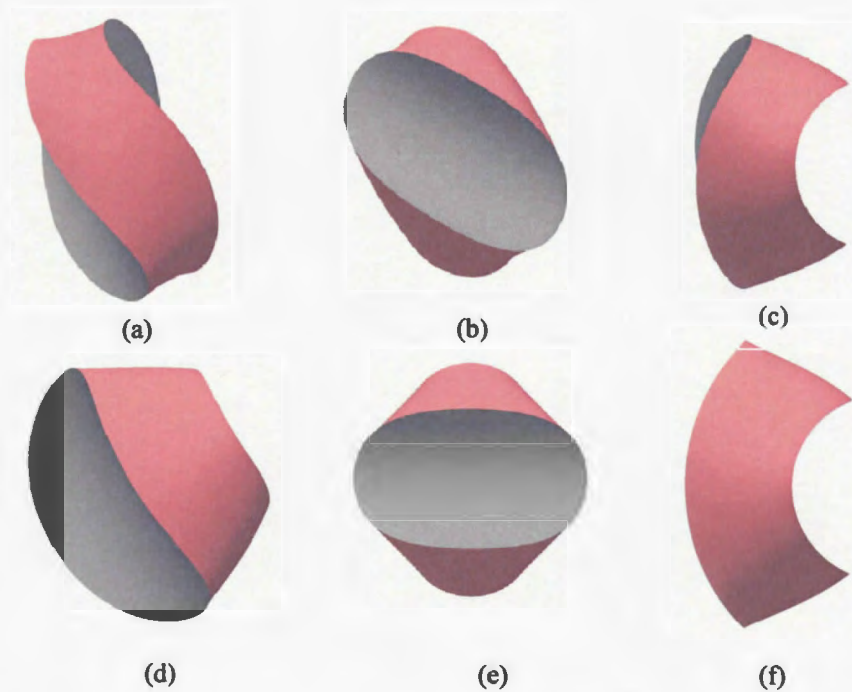
Figure 4.2: Final morphologies of the bridge-shaped systems when two filaments are misaligned. (a)Isometric view with orientation angle 45°; (b) front view with orientation angle 45°; (c) top view with orientation angle 45°; (d) isometric view with orientation angle 90°; (e) front view with orientation angle 90°; and (f) top view with orientation angle 90°. (Images were captured from graphical user interface of surface evolver program.)

4.4. Results and Discussion

To evaluate the effects of the above geometrical and surface property parameters on the final morphology, five, discrete orientation angles were selected in the range of 0° to 90° (i.e. 0°, 30°, 45°, 60° and 90°), while the other parameters were kept the same as in the simulation. Fig. 4.3 shows the variation of wetting length. It can be observed that, as the orientation angle increases, the wetting length shortens.

(a)   (b)   (c)

(d)   (e)
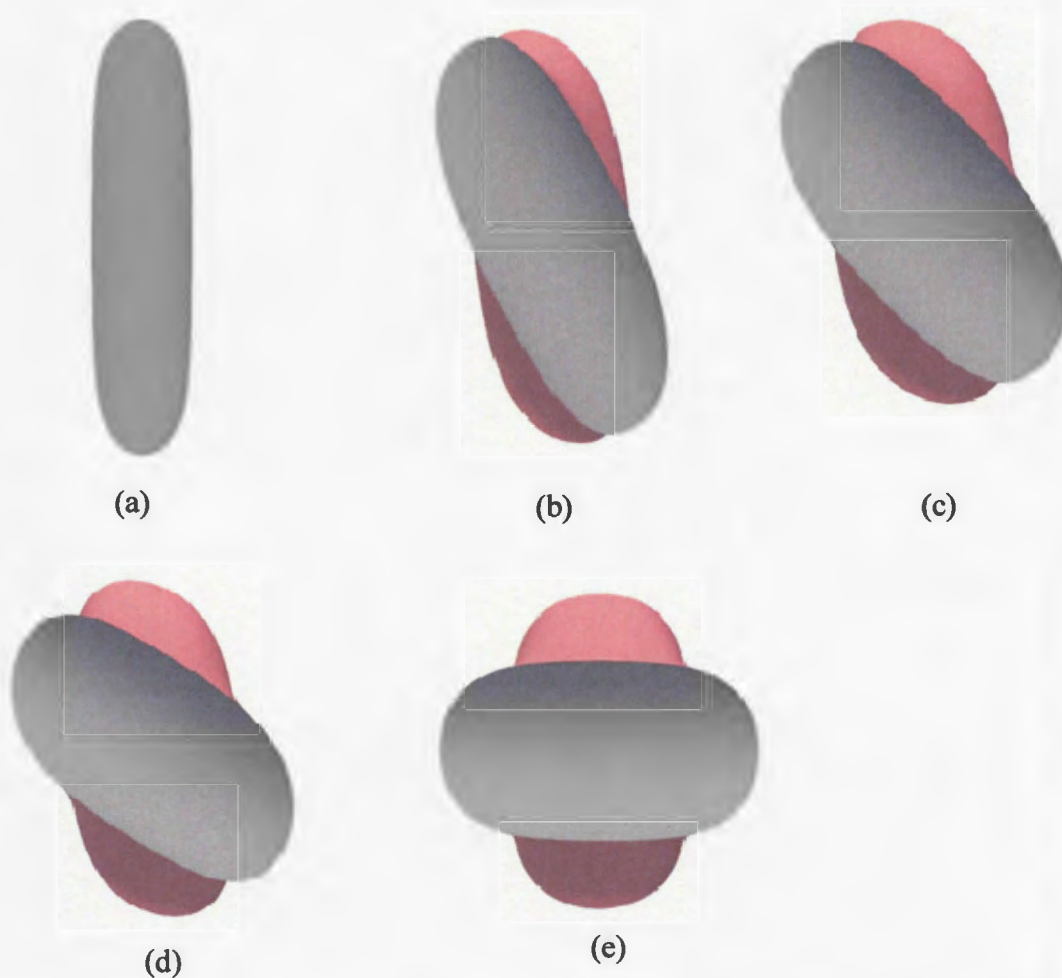
Figure 4.3: Variation of the droplet wetting length with varying orientation angles: (a) 0°, (b) 30°, (c) 45°, (d) 60°, and (e) 90°. In each simulation, the following parameters were fixed such that the radius of filaments $r= 1$, contact angle $\theta=30^o$, liquid-vapor surface tension $\gamma= 1$, and the droplet volume $V= 5$.

Fig. 4.4 shows a typical example of the surface energy of droplet bridge at varying filament orientation. It can be seen that the surface energy increases nonlinearly with increasing orientation angle, and two stationary points exist at oriental angles $0°$ (parallel filaments) and $90°$, corresponding to two torque-free droplet bridges of stable (minimum surface energy) and metastable (maximum surface energy) states, respectively.
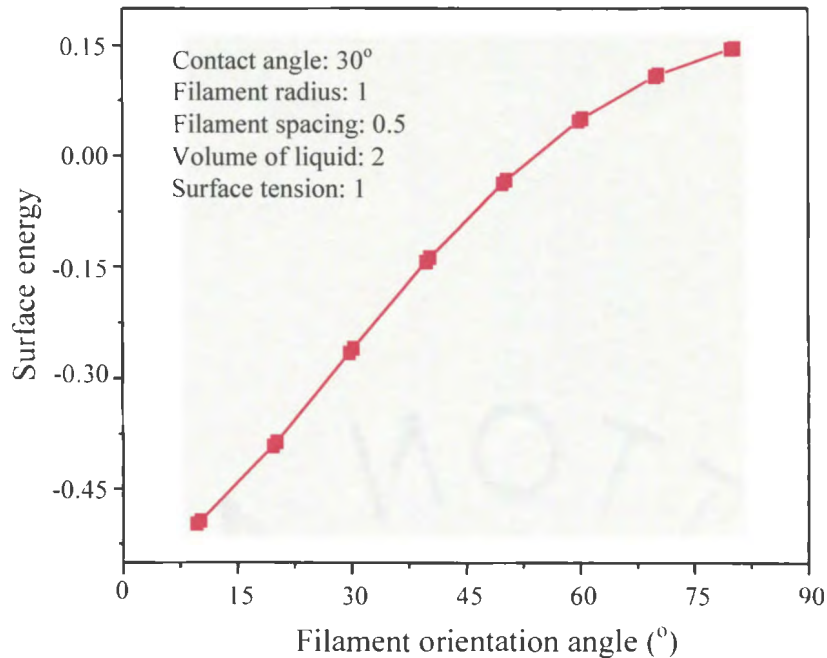
Figure 4.4: Variation of the surface energy Π vs. the filament orientation angle φ of a liquid bridge formed between two filaments of identical diameter and surface wetting properties. [The simulation was based on the Surface Evolver program with filament radius: r=1; filament spacing: D=0.5; droplet volume: V=2; and contact angle: $\theta=30°$]. (Bedarkar & Wu, 2009)

To calculate the capillary torque exerted due to misalignment between the two microfilaments, the total surface energy of the system at different orientation angles was calculated by executing the data file based on the Surface Evolver software package. The capillary torque for 8 discrete orientation angles (i.e. $10°$, $20°$, $30°$, $40°$, $50°$, $60°$, $70°$, and $80°$) has been calculated. For this purpose, central difference algorithm has been adopted

[Eq. (4.3)], in which a small angular increment 0.25° was chosen for the numerical differentiation. The capillary torque is plotted against the filament orientation angle, while other parameters were kept constant. It is observed from Figs. 4.5 and 4.6 that for given filament radius, separation distance, droplet volume, and surface tension, the capillary torque first increases gradually from the initial torque-free state at $\varphi=0^{\circ}$ up to the peak value and then starts decreasing down to the second torque-free state at $\varphi=90^{\circ}$. Moreover, the capillary torque increases rapidly with increasing droplet volume in both cases (spacing ratio $D/r= 0.5$ and 1) investigated in this numerical experiment.

In Figs. 4.6 and 4.7, the red line indicates results corresponding to the contact angle at 30°, while the blue one corresponds to those with a contact angle of 60°. The results in Figs 4.5 and 4.6 indicate that the capillary torque increases with a diminishing contact angle. Also, the capillary torque decreases with growing spacing ratio. Results shown in Figs. 4.5 and 4.6 are only for two contact angles which represent the general wetting and spreading behavior of hydrophilic liquids. In addition, the above numerical approaches have also been tried to cover hydrophobic liquids ($\theta>90^{\circ}$). However, numerical behavior observed in simulations was poor, and typically it was difficult to converge to a stable droplet morphology using the Surface Evolver program. Although no theoretical conclusion has been made yet in the literature such that no hydrophobic droplet bridges can be formed between two angled filaments of identical diameter and surface wetting properties, our numerical simulation tends to support such speculation. Thus, further theoretical study is still needed in order to explore the mechanism of hydrophobic liquid wetting on filaments.
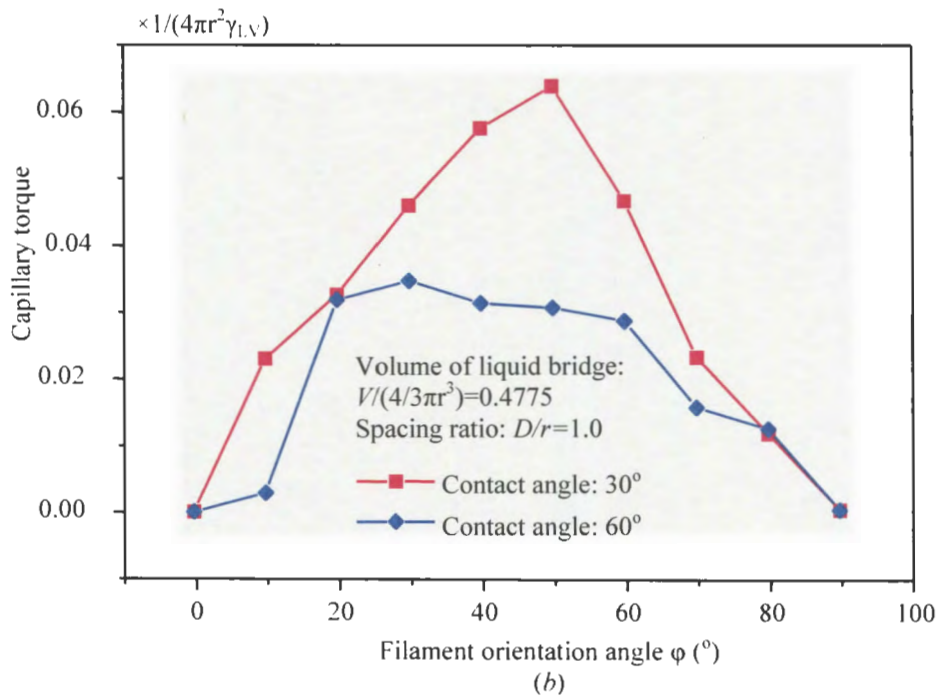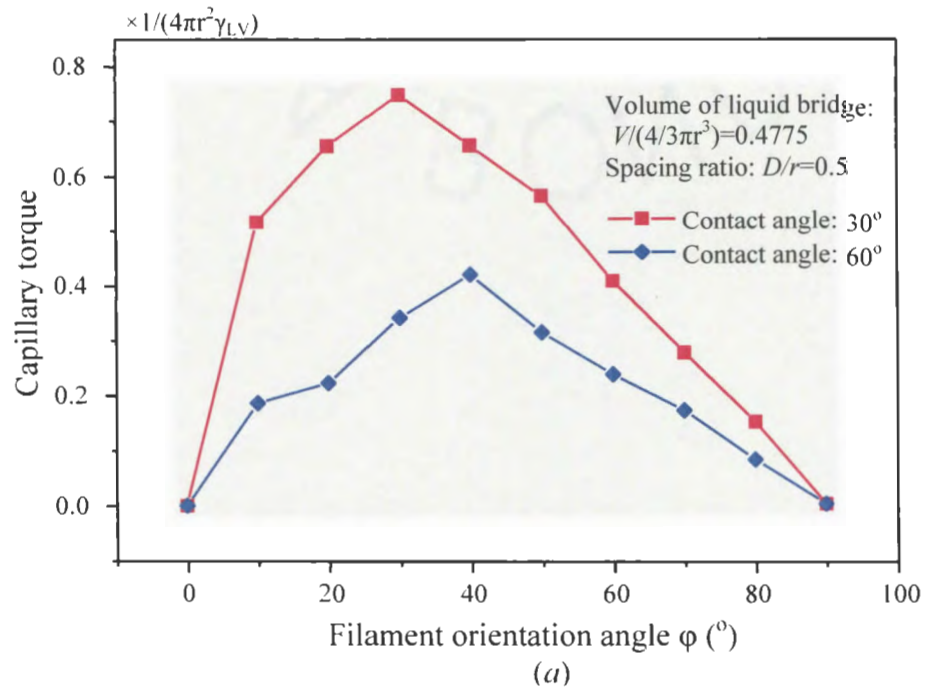
Figure 4.5: Variation of dimensionless capillary torque $T/[(4\pi r^2)\gamma_{LV}]$ vs. filament orientation angle φ. (a): Droplet volume: $V/(4/3\pi r^3)=0.4775$, filament spacing: D/r=0.5 and contact angle: $\theta=30^\circ$ and 60°; (b): droplet volume: $V/(4/3\pi r^3)=0.4775$, filament spacing: D/r=1 and contact angle: $\theta=30^\circ$ and 60°.
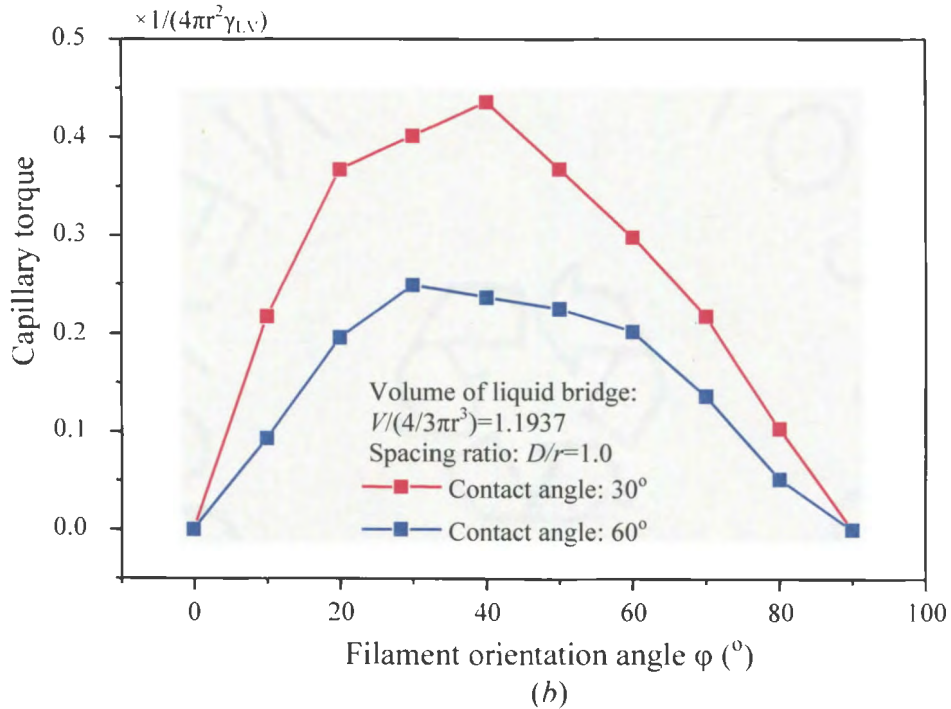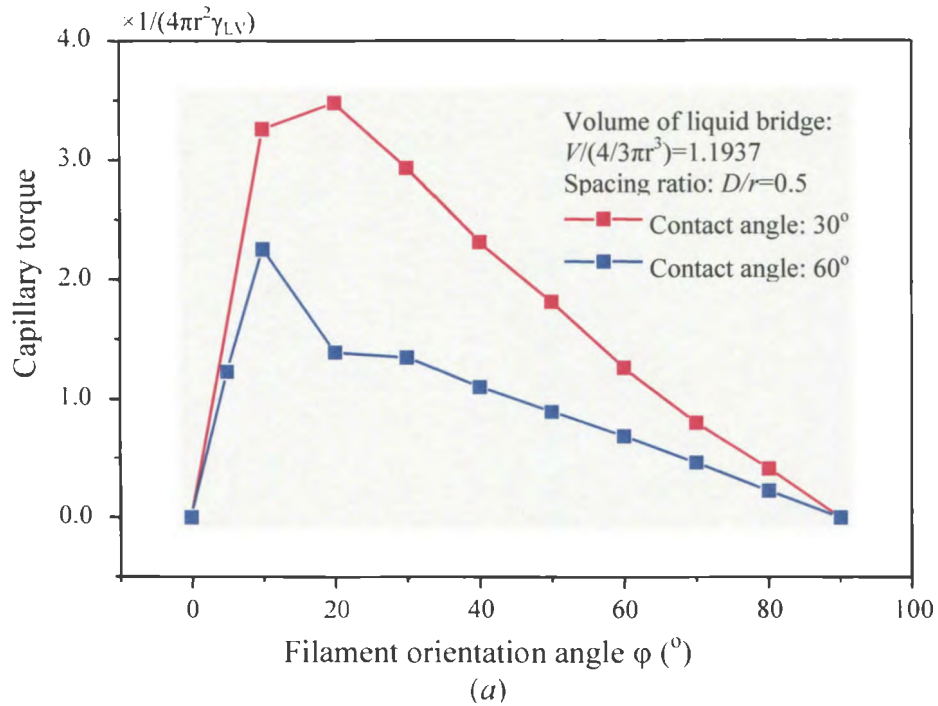
Figure 4.6: Variation of the dimensionless capillary torque $T/[(4\pi r^2)\gamma_{LV}]$ vs. the filament orientation angle φ. (a): Droplet volume: $V/(4/3\pi r^3)=1.1937$, filament spacing: D/r=0.5 and contact angle: $\theta=30^{\circ}$ and 60°; (b): droplet volume: $V/(4/3\pi r^3)=1.1937$, filament spacing: D/r=1 and contact angle: $\theta=30^{\circ}$ and 60°.

4.5. Summary

In this chapter, detailed, numerical simulation has been conducted to examine the capillary torque induced in a bridge-shaped system composed of two misaligned filaments. A family of capillary torque curves has been obtained, which demonstrates the variation of capillary torque with respect to orientation angle at varying filament spacing, droplet volume and contact angle. In the case of hydrophobic liquids, the present numerical study indicates that no stable droplet morphology can be achieved which projects an outstanding theoretical assumption that no hydrophobic droplet bridges can be formed between two misaligned filaments.

As an example of the study in this chapter, in the dying process, it is commonly observed that rod-like particles and microfilaments tend to align to each other when they sediment in solutions due to solvent evaporation. This alignment might be a result of capillary torque explored in this study. Capillary torque exerted on filaments can also be exploited for the assembly of microelectronic parts and the translation and alignment of biological cells, among other purposes.

CHAPTER 5. CAPILLARY EFFECT IN THE MECHANICAL BEHAVIOR OF ULTRATHIN SOFT FIBERS SUBJECTED TO AXIAL STRETCHING

This chapter is aimed to examine the capillary effect exerted by wetting droplets on the mechanical response of ultrathin compliant fibers subjected to axial stretching. Ultrathin soft fibers, such as those made of biopolymers and hydrogels, have been conveniently produced with recent development of fabrication technology, especially the birth of modern, electrospinning technique (Reneker and Chun, 1996; Li and Xia, 2004). When structured in a wet, vaporous, or humid environment, such as in biological tissues, these soft fibers are commonly wetted by water and biological fluids. Due to the small diameter of these fibers, typically in the range of hundreds of nanometers, droplets forming on fiber surfaces may induce an appreciable capillary effect in the mechanical response of these fibers. In this study, a novel, nonlinear, continuum hydroelastic model is formulated to examine such a combined effect of capillarity and axial stretch. During the process, the thin, compliant fiber is modeled as an incompressible, isotropically-hyperelastic, Mooney-Rivlin solid, whereas a barrel-shaped droplet morphology is presumed. An explicit solution is derived to evidence the reliance of mechanical behavior on parameters such as fiber diameter, droplet dimensions and wetting properties. Besides, critical condition for capillary buckling of the thin fibers wetted by droplets is determined. Results demonstrated in this chapter can be used in the prediction of realistic performance of soft nanofibers associated with liquid-vapor surrounding such as those structured in biological colloidal

64

solutions, etc. The method offered herein can be broadened to ultrathin, hollow filaments, among others.

5.1. Introduction

With recent development of nanotechnology, continuous fibers with the diameter ranging from tens to hundreds of nanometers can be conveniently produced by electrospinning. Besides, quite a few other technologies, such as drawing (Ondarcuhu & Joachim, 1998), template synthesis (Feng, et al, 2002; Martin, 1996), and phase separation (Liu, et al, 1999) have also been used to produce nanofibers. Among others, electrospinning is regarded as one of the most efficient and economic techniques that makes mass production possible (Huang, et al, 2003).

Fig. 5.1(a) illustrates the schematic setup of an electrospinning process, which consists of a high-voltage DC supply, a capillary tube connected to a polymer solution bath, and a conductive nanofiber collector. During the electrospinning process, one electrode of the setup is connected to the solution bath, while the other is attached to the nanofiber collector. As the DC voltage increases, an electrostatic stretching force is generated, which pulls and deforms the polymer solution at the tip of the capillary tube to form what is called a Taylor cone. When this force overcomes the surface tension of the Taylor cone, a thin, straight jet is released from the nozzle, and accelerates within the electrostatic field. The straight jet loses stability after initial thinning within a few centimeters. After solvent evaporation and drying, the ultrathin jet of solution is deposited on the collector plate as a nonwoven nanofiber mat.
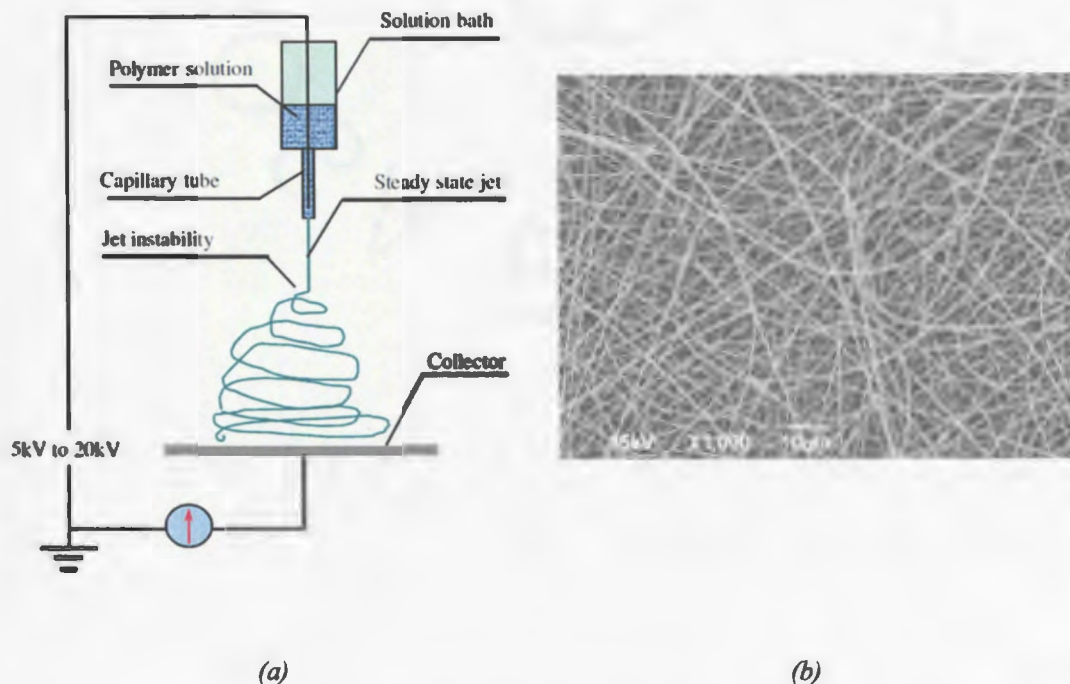
Figure 5.1: (a) Schematic electrospinning process. (b) Electrospun continuous PMMA nanofibers [Professor Wu's Laboratories at NDSU]

Fig 5.1(b) shows the typical scanning electron microscopy (SEM) image of poly (methyl methacrylate) (PMMA) nanofibers fabricated by electrospinning.

So far, nanofibers have found numerous applications, including nanofiber composites, biosensors, ultrafine filters, tissue scaffolds, etc. In reality, there is always a situation where the liquid droplet wets nanofibers and spreads across the surface. The mechanical response of such thin fibers, wetted by liquid droplets and simultaneously subjected to axial stretching, has not yet been studied in the literature. Thus, in this study, we will pursue the corresponding stress-stretch relationship of ultrathin soft fibers subjected to axial tension as well as capillary forces exerted by liquid droplets.

66

5.2. Problem Formulation

Consider a thin soft fiber wetted by micro-sized, barrel-shaped droplets, as illustrated in Fig 5.2. For generality, it is assumed that all droplets are of identical dimensions and properties. The ultimate shape of a single droplet can be achieved by minimizing the total potential energy of the combined system. The fiber undergoes a finite, radial deformation as a result of the combined effect of axial tension and capillary forces acting simultaneously on the fiber. Consequently, the mechanical response of the fiber is affected by axial stretching, surface tension, and capillary forces.

Forces acting on the thin, soft fibers are shown in Fig 5.3(*a*) and the corresponding deformation is illustrated in Fig. 5.3(*b*). Profile of the droplet near wetting fronts of the droplets is complicated and exerts forces (at an angle). Such forces may result in a localized increase in the fiber radius, while the center area of the droplet is in capillary compression due to the surface tension. For the purpose of simplification, only the fiber segment within the droplet is considered in this study, which is subjected to radial capillary pressure and axial capillary compression in the case of hydrophilic droplets.

A continuum mechanics approach will be employed to determine the analytical solution of this nonlinear, hydroelastic problem. Two configurations of the material point are presumed in this work, i.e. undisturbed stretch-free and current configuration after finite fiber deformation. Undisturbed, stretch-free configuration is the one without droplet, surface tension, and action of external forces; and the current configuration is the state of the fiber under the combined action of capillary forces and axial external forces. Corresponding coordinates of the material point in the cylindrical coordinate system are described as (R,Θ,Z) and (r,θ,z) respectively.

67
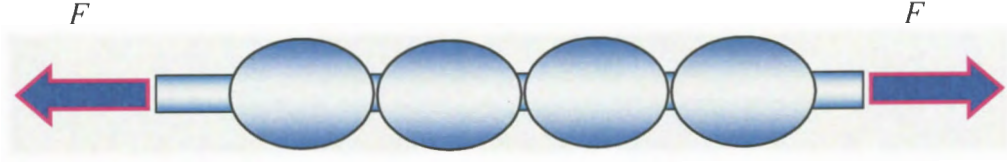
Figure 5.2: Schematic of a thin soft fiber wetted with liquid droplets and subjected to axial stretching (Wu, Bedarkar, & Akhatov, 2010)

(a)   (b)
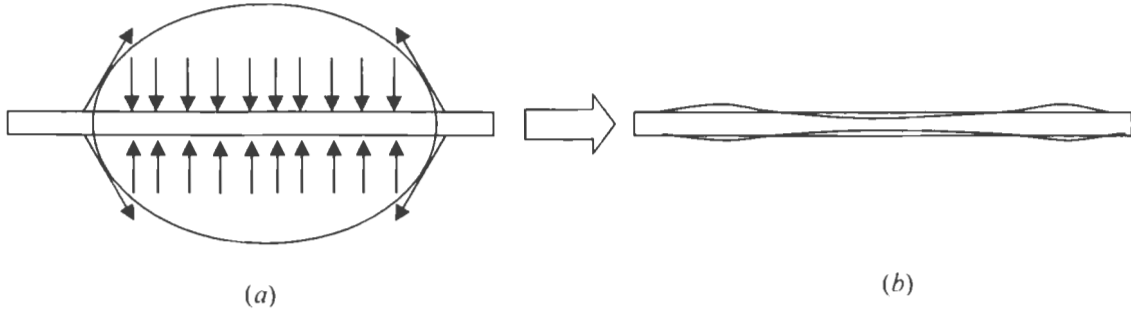
Figure 5.3: (a) Forces acting on a thin fiber and (b) Schematic deformation of the thin fiber across its length.

Axisymmetric deformation of the thin, soft fiber can be expressed as

$$r = \lambda_1 R \ (0 \le R \le R_0), \qquad \theta = \Theta \ (0 \le \Theta \le 2\pi), \qquad z = \lambda_3 Z, \tag{5.1}$$

where, λ_1 and λ_3 are transverse and longitudinal stretches, and they are independent of spatial location. The deformation gradient of the above deformation is

$$[F] = \begin{bmatrix} \partial r/\partial R & 1/R \ \partial r/\partial \Theta & \partial r/\partial Z \\ r \ \partial \theta/\partial R & r/R \ \partial \theta/\partial \Theta & r \ \partial \theta/\partial Z \\ \partial z/\partial R & 1/R \ \partial z/\partial \Theta & \partial z/\partial Z \end{bmatrix} = \begin{bmatrix} \lambda_1 & 0 & 0 \\ 0 & \lambda_1 & 0 \\ 0 & 0 & \lambda_3 \end{bmatrix}. \tag{5.2}$$

Material incompressibility leads to the condition that transverse and longitudinal stretches follow the following relationship:

$$\lambda_1^2 \lambda_3 = 1. \tag{5.3}$$

Hence, the resulting left Cauchy-Green tensor $[B]$ and its inverse can be expressed as,

68

$$[B] = \begin{bmatrix} \lambda_1{}^2 & 0 & 0 \\ 0 & \lambda_1{}^2 & 0 \\ 0 & 0 & \lambda_3 \end{bmatrix} \quad \text{and} \quad [B]^{-1} = \begin{bmatrix} \lambda_1{}^{-2} & 0 & 0 \\ 0 & \lambda_1{}^{-2} & 0 \\ 0 & 0 & \lambda_3{}^{-2} \end{bmatrix}. \tag{5.4}$$

Scalar invariants of $[B]$ are

$$I_1 = 2\lambda_1^2 + \lambda_3^2 = 2\lambda_3^{-1} + \lambda_3^2, \qquad I_2 = 2\lambda_3 + \lambda_3^{-2}, \qquad I_3 = 1. \tag{5.5}$$

It is assumed that the thin, soft fiber obeys the behavior of a general, incompressible, isotropic, hyperelastic Mooney-Rivlin solid. The corresponding, constitutive law is given by Cauchy stress tensor in terms of $[B]$ (Corwin & Doty, 2007).

$$T = -pI + 2c_1 B - 2c_2 B^{-1}, \tag{5.6}$$

where p is the hydrostatic pressure, and c_1 and c_2 are two material constants. In the special case of a Neo-Hookean solid, $c_2 = 0$ and c_1 is half of the shear modulus. The constitutive law given in relation (5.6) can be written in terms of stress components as below,

$$T_{rr} = T_{\theta\theta} = -p + 2c_1\lambda_1^2 - c_2\lambda_1^{-2} = -p + 2c_1\lambda_3^{-1} - 2c_2\lambda_3, \tag{5.7}$$

$$T_{zz} = -p + 2c_1\lambda_3^2 - 2c_2\lambda_1^4 = -p + 2c_1\lambda_3^2 - 2c_2\lambda_3^{-2}, \tag{5.8}$$

$$T_{r\theta} = T_{rz} = T_{\theta z} = 0. \tag{5.9}$$

The deformation of the fiber is axisymmetric, and the corresponding equilibrium equations in a spatial cylindrical coordinate system can be expressed as

$$\frac{\partial T_{rr}}{\partial r} + \frac{T_{rr} - T_{\theta\theta}}{r} = 0, \tag{5.10}$$

$$\frac{\partial T_{\theta\theta}}{\partial \theta} = 0, \tag{5.11}$$

$$\frac{\partial T_{zz}}{\partial z} = 0. \tag{5.12}$$

Surface tension and capillary pressure acts on the fiber surface, which causes radial compressive stress to act on the fiber.

$$T_{rr} = -\frac{\gamma_{LS}}{r_0} - p_0, \tag{5.13}$$

where γ_{LS} (J) is the specific, interfacial energy between the solid, fiber material and liquid droplet, which is assumed to be independent of the fiber radius and axial stretch. p_0 is the capillary pressure to be determined by the resulting Young-Laplace equation (Carroll, 1976; Wu and Dzenis, 2006). r_0 is the fiber radius in the current configuration. If we equate forces along the fiber axis, we will get

$$P = 2\pi \int_0^{r_0} rT_{zz}dr + 2\pi r_0 \gamma_{LV} \cos\varphi, \tag{5.14}$$

where, P is the external, applied force along the fiber axis, γ_{LV} is the surface tension of the liquid, and φ is the contact angle between liquid and fiber surface. p_0 is constant in Eq. (5.13). Substitution of Eqs. (5.7) and (5.8) into Eqs. (5.11) and (5.12) yields,

$$\frac{\partial p}{\partial \theta} = \frac{\partial p}{\partial z} = 0. \tag{5.15}$$

Eq. (5.15) indicates that the hydrostatic pressure p is only a function of r, such that

$$p = p(r). \tag{5.16}$$

Additionally, eliminating p_0 in Eqs. (5.7) and (5.8) and then solving Eq. (5.10) determine T_{zz} as

$$T_{zz} = 2\left(\lambda_3^2 - \frac{1}{\lambda_3}\right)\left(c_1 + \frac{c_2}{\lambda_3}\right) - \frac{\gamma_{LS}}{r_0} - p_0. \tag{5.17}$$

Substituting Eq. (5.17) into (5.14) yields,

$$P = 2\pi r_0^2\left(\lambda_3^2 - \frac{1}{\lambda_3}\right)\left(c_1 + \frac{c_2}{\lambda_3}\right) - \pi r_0 \gamma_{LS} - \pi r_0^2 p_0 + 2\pi r_0 \gamma_{LV} \cos\varphi. \tag{5.18}$$

Capillary pressure p_0 in Eq. (5.18) can be determined by formulating the hydrostatic problem of the barrel-shaped droplet on the fiber as shown in Fig 5.4.
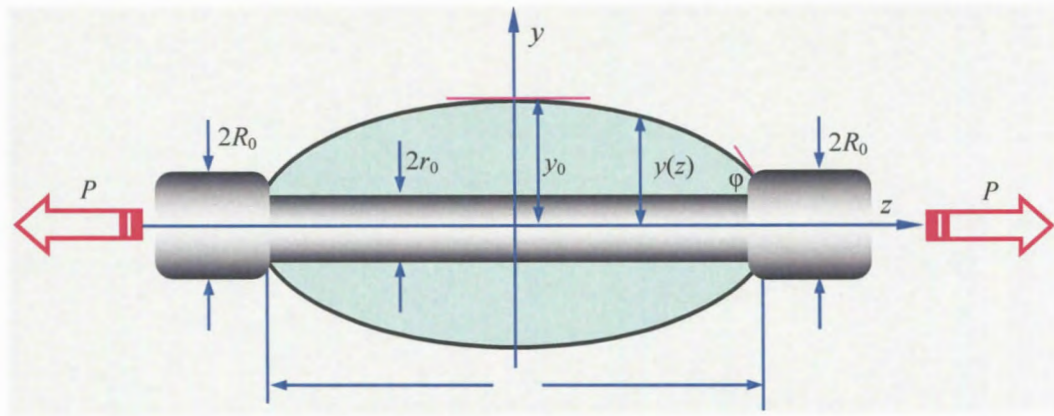
Figure 5.4: Geometries of a barrel-shaped droplet wetting on a thin fiber (Wu, Bedarkar, & Akhatov, 2010).

Furthermore, total potential energy of the droplet-on-filament system is given by the following energy functional (Wu & Dzenis, 2006):

$$J = 4\pi \int_0^{L/2} \left\{ (\gamma_{LS} - \gamma_{LV})r_0 + \gamma_{LV}y(z)\sqrt{1 + [y'(z)]^2} \right\} dz, \tag{5.19}$$

where L is the total wetting length of the droplet, $y(z)$ is the droplet radius at location z. Moreover, in Eq. (5.19), the droplet shape has been assumed to be axisymmetrical because droplet gravity has been neglected, as aforementioned in the proceeding chapters. The boundary conditions at $z = 0$ (droplet mid-plane) and $z = L/2$ (wetting front) are known and given by,

$$y'(0) = 0 \text{ and } y(L/2) = r_0. \tag{5.20}$$

Constant volume of a barrel-shaped droplet is given by the following equation:

71

$$V_0 = 2\pi \int_0^{L/2} \{[y(z)]^2 - r_0^2\} \, dz. \tag{5.21}$$

We need to determine the radius of droplet at peak value $y(0)$ and the total droplet wetting length L.

Barrel-shaped morphology of a droplet wetting on a filament can be determined by solving the above variation problem (5.19) based on the constraints specified in (5.20) and (5.21) (Carroll, 1976; Wu and Dzenis, 2006):

$$z = \int_y^{y_0} \frac{(y^2 + \eta r_0 y_0)}{\sqrt{(y_0^2 - y^2)(y^2 - \eta^2 r_0^2)}} \, dy, \tag{5.22}$$

where,

$$\eta = \frac{y_0 \cos\varphi - r_0}{y_0 - r_0 \cos\varphi}. \tag{5.23}$$

Then, capillary pressure of the droplet can be determined as (Carroll, 1976)

$$p_0 = \frac{2\gamma_{LV}(y_0 - r_0 \cos\varphi)}{y_0^2 - r_0^2}. \tag{5.24}$$

With the use of Eq. (5.23), the volume of droplet in Eq. (5.22) is written as,

$$V_0 = 2\pi \int_{r_0}^{y_0} \frac{(y_0^2 - r_0^2)(y^2 + \eta r_0 y_0)}{\sqrt{(y_0^2 - y^2)(y^2 - \eta^2 r_0^2)}} \, dy, \tag{5.25}$$

and the wetting length (L) can be determined as

$$L = 2 \int_{r_0}^{y_0} \frac{(y^2 + \eta r_0 y_0)}{\sqrt{(y_0^2 - y^2)(y^2 - \eta^2 r_0^2)}} \, dy. \tag{5.26}$$

With the axis of Eq. (5.1) i.e. $r_0 = \lambda_1 R_0 = \frac{R_0}{\sqrt{\lambda_3}}$, the axial engineering stress can be determined from (5.18) such that

72

$$\sigma = \frac{P}{\pi R_0^2} = 2\left(\lambda_3 - \frac{1}{\lambda_3^2}\right)\left(c_1 + \frac{c_2}{\lambda_3}\right) - \frac{\gamma_{LS} - 2\gamma_{LV}\cos\varphi}{\sqrt{\lambda_3}R_0} - \frac{p_0}{\lambda_3}. \tag{5.27}$$

Eq. (5.27) gives the axial engineering stress in the fiber due to the combined effect of axial stretch and capillary forces exerted by a droplet. This axial stress depends on the system parameters, including axial stretch, material constants, surface tension, fiber radius, and droplet volume.

5.3. Critical Conditions for Capillary Buckling

Wetting properties of the liquid-solid interface can be determined for given geometry and surface chemistry. So, the liquid droplet that wets the solid surface is either hydrophilic (with a contact angle less than 90°) or hydrophobic (with a contact angle greater than 90°). If hydrophilicity prevails, capillary forces acting on a thin fiber result in the axial compressive forces. Moreover, if hydrophobicity exists, capillary forces, as a result, generate axial tensile forces. Focusing on hydrophilic liquids, buckling of the ultrathin fiber can be the outcome of such axial compression. If the fiber is assumed as stiff (with negligible radial deformation), the classical Euler buckling theory of elastic columns is applicable; consequently allowing researchers to determine the critical condition for capillary buckling.

Classic Euler buckling theory is presented in terms of maximum axial force that a slender elastic column can withstand before it undergoes buckling, as

$$F = \frac{\pi^2 EI}{(KL)^2}, \tag{5.28}$$

73

where, F is the maximum axial force before buckling, E is the elastic modulus of the column (fiber) material, I is the moment of inertia of the cross-sectional area, K is the column-length effective factor, and L is the total length.

Returning to the problem related to the current study, two buckling conditions can be justified for the upper and lower limiting cases. The upper limiting case is the one where two wetting fronts of the fiber are assumed to be fixed, so the effective column length factor in the Euler buckling formula takes the value of 0.5. The second boundary condition is the one where fiber is assumed to be jointed at two wetting fronts. In this case, $K=2$.

Furthermore, the axial capillary force exerted by the droplet is

$$F_c = 2\pi R_0 \gamma_{LV} \cos \varphi. \tag{5.29}$$

The Euler buckling condition for the first boundary condition ($K = 0.5$) becomes

$$F = \frac{4\pi^2 EI}{L^2}, \tag{5.30}$$

and for the second boundary condition with ($K = 2$), it is

$$F = \frac{\pi^2 EI}{4L^2}. \tag{5.31}$$

For the fiber of circular cross-section, $I = \pi R_0^4 / 4$. By correlating Eq. (5.29) and Eq. (5.30) for the upper case and correlating Eq. (5.29) and Eq. (5.31) for the lower case, the capillary buckling condition is presented in terms of the critical slenderness ratio ($\lambda_c = L/R$).

$$\lambda_c^{upper} = \pi \sqrt{\frac{ER_0}{2\gamma_{LV} \cos \varphi}} \tag{5.32}$$

$$\lambda_c^{lower} = \frac{\pi}{4} \sqrt{\frac{ER_0}{2\gamma_{LV} \cos \varphi}} \tag{5.33}$$

Consequently, the range of critical slenderness ratio λ_c is expressed as

$$\frac{\pi}{4}\sqrt{\frac{ER_0}{2\gamma_{LV}\cos\varphi}} \leq \lambda_c \leq \pi\sqrt{\frac{ER_0}{2\gamma_{LV}\cos\varphi}} \qquad (5.34)$$

As an example, if a soft polymer fiber with Young's modulus 8 GPa, diameter 8 μm, is wetted by a water droplet (γ_{LV} =72.8 dyne/cm at 20°C) at a contact angle of 30°, the critical slenderness ratio varies in the range of 560-2238. This is a very large value so the possibility of capillary buckling is much less. However, for a soft nanofiber with Young's modulus 150 MPa, diameter 100 nm is wetted with water with the same properties, the corresponding, critical, slender ratio is in the range of 8-34. This range is favorable to nanofibers of the given size so the capillary buckling is likely to happen in ultrathin, compliant fibers.

5.4. Numerical Stress-Stretch Diagrams

The most conventional technique to signify the mechanical behavior of any material is the stress-stretch diagram. In the present study, stress-stretch diagrams are plotted for a number of combinations to represent the mechanical response of the thin, soft fibers with the combined effect of axial stretch and capillarity.

To calculate the tensile stress for every value of stretch λ_3, we use the relationship $r_0 = \lambda_1 R_0 = \frac{R_0}{\sqrt{\lambda_3}}$ to find out r_0. Now, by using the known quantities r_0 and V_0, y_0 has been determined by using Eq. (5.25), which allows evaluation of the capillary pressure p_0 using Eq. (5.24). Axial engineering stress σ can be determined eventually by Eq. (5.27). Iterative method has been employed to evaluate y_0 with the help of Matlab[TM] software. In the numerical simulation process, a vulcanized rubber compound (Trelorar, 1975) is used as

the material for the thin, soft fiber, with two material constants where c_1=0.2 MPa and c_2 = 0.1 MPa. The liquid droplet is assumed to be of water with γ_{LV} = 72.8 dyne/cm at 20°C. The effect of liquid-solid surface energy γ_{LS} on the mechanical behavior of thin, soft fibers has been explored in recent literature (Wu & Dzenis, 2007; Wu, et al. 2000; Wu 2010) and, therefore, is neglected herein for simplification.

In the simulation process, as shown in Fig. 5.5, combinations of five, thin, fiber radii (R_0 = 50, 100, 200, 500 and 1,000 nm), two dimensionless droplet volumes [$V_0 / (4/3\pi R_0^3))$ = 50, 100], and two contact angles (φ = 15° and 45°) selected. The volumes selected here confirm the stable barrel-shape morphology (McHale & Newton, 2002). The reason for not maintaining the hydrophobic liquid with the contact angle more than 90° is that it is hard to achieve a stable barrel-shape morphology based on McHale and Newton's argument (2002). Results obtained from the simulations are plotted in graphical format as shown in Fig. 5.5.

Fig. (5.5) indicates the variation of dimensionless axial stress σ/c_1 with respect to the axial stretch λ_3 at varying fiber radius, dimensionless, droplet volume and contact angle. This proves that, for the case of hydrophilic, liquid droplets, load carrying capacity of fiber increases. It has been observed that the axial stress decreases with increasing fiber radius in every possible combination. Moreover, numerical results show that the axial tensile stress at λ_3=1 is approximately 50% less at φ =45° compared to φ =15°. This effect becomes less prominent as the axial stretch increases and fiber diameter reduces.
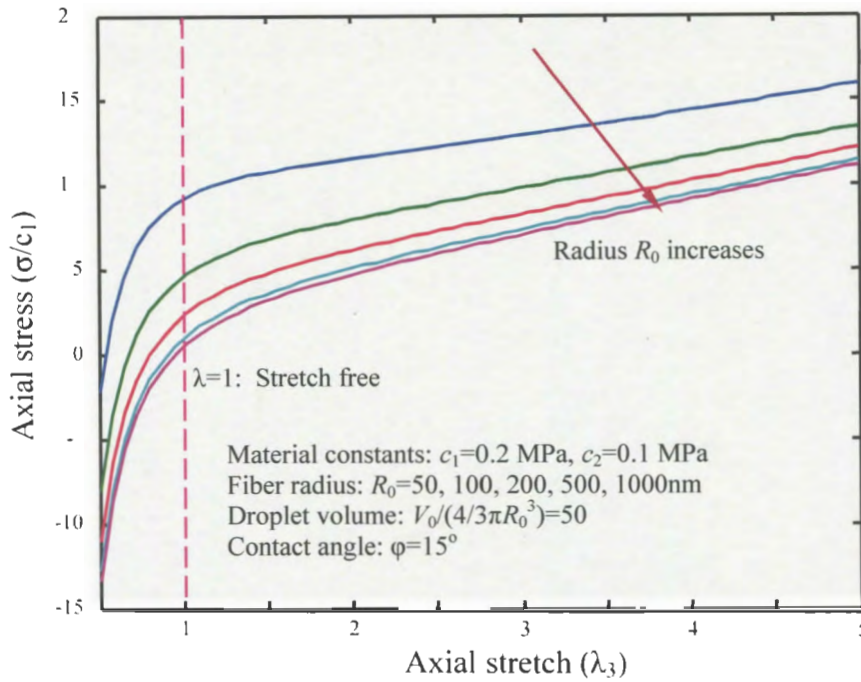
Figure 5.5 (a): Axial stress-stretch diagrams of soft thin fibers at varying fiber radius at dimensionless droplet volume =50 and contact angle 15^0. (Wu, Bedarkar, & Akhatov, 2010)

Figure 5.5 (b): Axial stress-stretch diagrams of soft thin fibers at varying fiber radius at dimensionless droplet volume =50 and contact angle 45°. (Wu, Bedarkar, & Akhatov, 2010)

77

Figure 5.5 (c): Axial stress-stretch diagrams of soft thin fibers at varying fiber radius at dimensionless droplet volume =100 and contact angle 15°. (Wu, Bedarkar, & Akhatov, 2010)
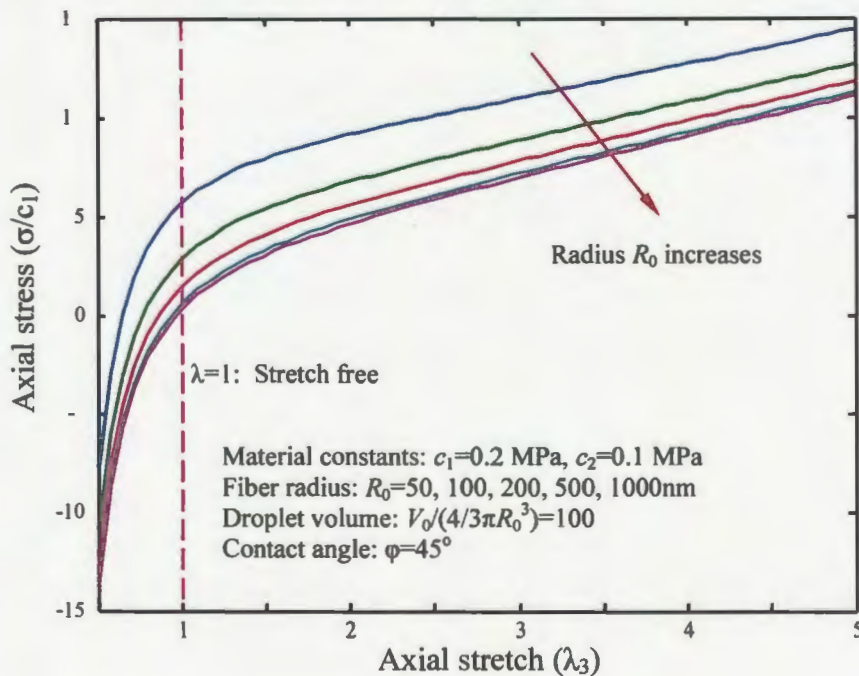
Figure 5.5 (d): Axial stress-stretch diagrams of soft thin fibers at varying fiber radius at dimensionless droplet volume =100 and contact angle 45°. (Wu, Bedarkar, & Akhatov, 2010)

By increasing droplet volume, capillary pressure decreases; consequently, the effect of capillarity on the mechanical properties is suppressed further. Nevertheless, the axial compression, due to surface tension, is dependent on droplet volume. In addition, the effect of capillary pressure is opposite to that of the capillary forces exerted at wetting fronts (compression) for a hydrophilic droplet. Thus, the larger the droplet volume, the higher the load-carrying capacity of the fiber. However, such an effect is not very significant, even for the smallest fiber radius of 50 nm. Fig. 5.5 also depicts that at the stretch free state i.e. $\lambda_3=1$, a certain external axial force is needed to maintain a stretch-free state, because the axial compressive force induced by capillary forces results in a negative, effective, axial force of the thin, soft fiber. This effect increases with decreasing fiber radius and contact angle.

5.5. Summary

Mechanical behavior of thin, compliant fiber wetted by a liquid droplet is studied in this chapter using the concepts of continuum mechanics. Mooney-Rivlin hyperelastic material behavior is assumed for the thin, soft fiber, and the droplet wetting on nanofiber is considered to assume a barrel-shaped morphology. It has been observed that the influence of capillarity results in axial compression, which further reinforces the softening of the thin fiber. Results incurred from numerical analysis demonstrate that the capillary effect becomes more dominant as the fiber radius and contact angle decreases. Critical conditions for capillary buckling has been put forward based on the concept of Euler buckling theory. This type of buckling is more eminent in ultrathin, soft fibers in contrast to micro-sized fibers. Results obtained in this study are useful in design and analysis of devices constituting thin, soft fibers by regulating its properties. Moreover, the procedure

developed in this chapter can be extended to determine the mechanical behavior of hallow, soft filaments, and other soft, microfluidic systems used for micro and nano liter liquid delivery and biological cell transportation and manipulation.

CHAPTER 6. SUMMARY AND FUTURE RESEARCH

A detailed computational study on droplet wetting on micro and nano filaments has been performed in this research. Surface finite element method based on the open source Surface Evolve software package has been used and user interface data files have been developed for all the cases under consideration. In the case of a droplet wetting symmetrically on two parallel filaments of identical diameter and surface wetting properties, critical condition of the morphology transition between barrel-shaped morphology and liquid-bridge morphology has been determined in terms of a family of wetting characteristic curves (W-curves). Each characteristic W-curve gives the critical, dimensionless, droplet volume as a function of filament spacing ratio at given contact angle, which defines the boundary of a barrel-preferred droplet and a liquid-bridge preferred droplet in the dimensionless droplet volume-spacing ratio phase diagram. These W-curves can facilitate the experimental and computational processes of droplet wetting on filaments since the W-curves can be used to predict the energy-favored droplet morphology and provide a background for future, rigid theoretical examination. The concepts of critical condition and W-curves can be conveniently extended to other microfluidic systems and multi-filament systems.

Besides, capillary torque induced in a distorted droplet bridging two misaligned filaments has been determined by numerical differentiation of the potential energy of the droplet-on-filament system at varying filament spacing, droplet volume, contact angle, and filament orientation angle. Results obtained in this study are applicable for micro and nano liter liquid delivery, nonlinear capillary twister, and biological cell transportation and manipulation, among others. The present computation also discovered the phenomenon that

81

hydrophobic droplets cannot form stable liquid bridges between filaments although no rigid theory is available in the literature at this moment.

Moreover, an explicit solution is presented for the mechanical behavior of ultrathin, soft fibers wetted with micro droplets. It is founded that for hydrophobic droplets, appreciable axial stresses are exerted at small fiber diameters, which can even induce capillary buckling at specific slenderness ratios as derived in this study. The study opens up an innovative research field of the hydroelasticity of micro and nano filamentary materials as growing soft micro and nanofibers of biopolymers and hydrogels are finding applications in biomedical, bioengineering, and other applications.

Potential future research work related to this study includes:

(a) Extension of the concepts of morphology transition, wetting characteristic curves, and capillary torque to other microfluidic and droplet-on-filament systems, such as droplet-on-filament systems made of filaments of dissimilar diameters and surface properties;

(b) Kinematic and dynamic study of two dissimilar droplets engulfing on filaments;

(c) Hydroelastic study of interaction between droplets and multi-filaments and filamentary materials;

(d) Experimental study of droplet wetting and spreading on filaments and filamentary materials;

(e) Design and computational analysis of droplet-on-filament microfluidic devices for micro and nano liter liquid delivery, microelectronics, and biological cell transporters and manipulators, among others.

REFERENCE

- Bedarkar, A., & Wu, X. F. (2009). Capillary Torque in a Liquid Bridge Between Two Angled Filaments. *Journal of Applied Physics*, *106*, 113527-1 to 113527-5.

- Bedarkar, A., Wu, X. F., & Vaynberg, A. (Under Review). Wetting of Liquid Droplets on Parallel Filament Rails. *Applied Surface Science*.

- Bernet, N. P., Bourban, P.-E., & Maason, J.-A. E. (2000). On the Characterization of Wetting and Adhesion in Glass Fiber-PA12 Composites. *Journal of Thermoplastic Composite Materials*, *13*, 434-450.

- Booyabazooka. (2008). *Wikipedia*. Retrieved from http://en.wikipedia.org/wiki/File:WassermoleküleInTröpfchen.svg

- Brakke, K. A. (2008, Jan 01). Surface Evolver Manual version 2.30.

- Brakke, K. A. (2008). Surface Evolver Software.

- Bush, J. W. (2004, May). *MIT Lecture Notes on Surface Tension, lecture 3*. Retrieved from http://web.mit.edu/1.63/www/Lec-notes/Surfacetension/Lecture3.pdf

- Carroll, B. J. (1986). Equilibrium Conformation of Liquid Drops on Thin Cylinders under Forces of Capillarity. A theory for the Roll-up Process. *Langmuir*, *2*, 248-250.

- Carroll, B. J. (1976). The Accurate Measurement of Contact Angle, Phase Contact Areas, Drop Volume and Laplace Excess Pressure in Drop-on-Fiber Systems. *Journal of Colloid and Interface Science*, *57*, 488-495.

- Cowin, S., & Doty, S. (2007). *Tissue Mechanics*. New York: Springer.

- Demarquette, N. R. (2003). Evaluation of experimental techniques for determining interfacial tension between molten polymers. *International Materials Reviews , 48,* 247-269.

- Ebbesen, T. W. (1996). Wetting, Filling and Decorating Carbon Nanotubes. *J. Phys. Chem Solids , 57,* 951-955.

- Finn, R. (1986). *Equilibrium Capillary Surfaces.* New York, NY, USA: Springer-Verlag New York Inc.

- Gennes, P.-G. d., Brochard-Wyart, F., & Quere, D. (2001). *Capillarity and Wetting Phenomena.* (A. Reisinger, Trans.) New York, NY, USA: Springer.

- Herval. (2005). Retrieved from http://www.flickr.com/photos/herval/19252684/sizes/o/

- Huang, Z., Liao, X., Kang, Y., Yin, G., & Yao, Y. (2009). Equilibrium of drops on inclined fibers. *Journal of colloid and Interface Science. , 330,* 399-403.

- Hunter, R. J. (1998). *Introduction to Modern Colloid Science.* New York, NY, USA: Oxford University Press Inc.

- Keis, K., Kornev, K. G., Neimark, A. V., & Kamath, Y. K. (2004). *Nanoengineered Nanofibrous Materials.* (S. Guceri, Y. G. Gogotsi, & V. Kuznetov, Eds.) Springer.

- Koponen, A., Kandhai, D., Hellen, E., Alava, M., Hoekstra, A., Kataja, M., et al. (1998). Permeability of Three-Dimensional Random Fiber Webs. *Physical Review Letters , 80,* 716-719.

- Le, C. V., Ly, N. G., & Stevens, M. G. (1996). Measuring the Contact Angles of Liquid Droplets on Wool Fibers and Determining Surface Energy Components. *Textile Research Journal*, *66*, 389-397.

- Lin, F., Shuhong, L., Huanjun, L., Jin, Z., Yanlin, S., Lei, J., et al. (2002). Super Hydrophobic Surface of Aligned Polyacrylonitrile Nanofibers. *Angew Chem Ed*, *41(7)*, 1221.

- Liu, G., Ding, J., Qiao, L., Guo, A., Dymov, B., & Gleeson, J. (1999). Polystyrene-block-poly (2-cinnamoylethyl methacrylate) nanofibers-Preparation, characterization and liquid crystalline properties. *Chem-A European J*, *5*, 2740.

- Logan, J. D. (1997). *Applied Mathematics, second edition*. New York: Wiley.

- Lucas, R. (1918). Ueber das Zeitgesetz des kapillaren Aufstiegs von Flüssigkeiten. *Colloid & Polymer Science*, *23*, 15-22.

- Lukas, D., & Pan, N. (2003). Wetting of a Fiber Bundle in Fibrous Structures. *Polymer Composites*, *24*, 314-322.

- Lukas, D., Chaloupek, J., Kostakova, E., Pan, N., & Martinkova, I. (2006). Morphological transitions of capillary rise in a bundle of two and three solid parallel cylinders. *Physica A*, *371*, 226-248.

- Martin, C. (1996). Membrane-based synthesis of nanomaterials. *Chem Mater*, *8*, 1739.

- McHale, G., & Newton, M. I. (2002). Global geometry and the equilibrium shapes of liquid drops on fibers. *Colloids and Surfaces.*, *206*, 79-86.

- McHale, G., Newton, M. I., & Carroll, B. J. (2001). The Shape and Stability of small Liquid Drops on Fibers. *Oil and Gas Science and Technology*, *56*, 47-54.

- Ondarcuhu, T., & Joachim, C. (1998). Drawing a single nanofiber over hundreds of micron. *Europhys Lett*, *42(2)*, 215.

- Princen, H. M. (1969). Capillary Phenomena in Assemblies of Parallel Cylinders I. Capillary Rise between Two Cylinders. *Journal of Colloid and Interface Science.*, *30* (1), 69-75.

- Princen, H. M. (1969). Capillary Phenomena in Assemblies of Parallel Cylinders II. Capillary Rise in Systems with More Than Two Cylinders. *Journal of Colloid and Interface Scinece.*, *30* (3), 359-371.

- Princen, H. M. (1970). Capillary Phenomena in Assemblies of Parallel Cylinders III. Liquid Columns between Horizontal Parallel Cylinders. *Journal of Colloid and Interface Science*, *34* (2), 171-184.

- Quere, D. (1999). Fluid Coating on a Fiber. *Annu. Rev. Fluid Mech*, *31*, 347-384.

- Song, B., Bismarck, A., Tahhan, R., & Springer, J. (1998). A Generalized Drop Length-Height Method for Determination of Contact Angle in Drop-on-Fiber Systems. *Journal of Colloid and Interface Science.*, *197*, 68-77.

- Trelorar, L. (1975). *The Physics of Rubber Elasticity.* Clarendon, Oxford.

- Vaynberg, A., Stuart, M., & Wu, X.-F. (2009). Differential wetting characterization of hair.

- Wagner, H. D. (1990). Spreading of liquid droplets on cylindrical surfaces: Accurate determination of contact angle. *Journal of Applied Physics.* , *63* (3), 1352-1355.

- Washburn, E. W. (1921). The Dynamics of Capillary Flow. *The Physical Review* , *13*, 273-283.

- Wu, X. F., Bedarkar, A., & Vaynberg, A. k. (2010). Droplet Wetting on Filament Rails: Surface Energy and Morphology Transition. *Journal of Colloid and Interface Science* , *341*, 326-332.

- Wu, X.-F. (2010). Wave Propagation in Prestretched polymer nanofibers. *Journal of applied physics* , *107*, 013509.

- Wu, X.-F., & Dzenis, Y. A. (2006). Droplet on a fiber: geometrical shape and contact angle. *Acta Mechanica* , *185*, 215-225.

- Wu, X.-F., & Dzenis, Y. (2007). Size effect in polymer nanofibers under tension. *Journal of applied physics* , *102*, 044306.

- Wu, X.-F., Bedarkar, A., & Akhatov, I. (2010). Capillary Effect in the mechanical response of compliant ultrathin fibers wetted with droplets. *Underreview* .

- Wu, X.-F., Kostogorova-Beller, Y. Y., Goponenko, A., Hou, H., & Dzenis, Y. A. (2008). Rippling of Polymer Nanofibers. *Physical Review E* , *78*, 061804.

- Yamaki, J.-I., & Katayama, Y. (1975). New Method of Determining Contact Angle between Monofilament and Liquid. *Journal of Applied Polymer Science* , *19* (10), 2897-2909.

- Yarin, A. L., & Oron, A. (1993). Capillary Instability of thin liquid film on a cylinder. *Phys. Fluids A , 5*, 91-98.

- Zheng-Ming, H., Zhang, Y.-Z., Kotaki, M., & Ramakrishna, S. (2003). A review on polymer nanofibers by electrospinning and their applications in nanocomposites. *Composite Science and Technology , 63*, 2223.

APPENDIX A: SURFACE EVOLVER DATAFILES – CHAPTER 3

1.   Data file for the droplet-bridge shaped morphology. (Complete Model):

Parameter	rodr = 1	//fiber radius
Parameter	ratio = 1	
#define	DL (rodr/sqrt(2))	// initial dimension of fiber
parameter	spin = 0.0	// angular velocity
parameter	angle = 60	// internal contact free surface
parameter	tens = 1	// surface tension of free surface
parameter	pp = pi/2	// to be halved each refinement
parameter	qq = pi/6	// to be halved each refinement
parameter	pp2=pi/2	// to be halved each refinement
parameter	qq2=pi/6	// to be halved each refinement
Parameter	dens= 0	

#define rode -tens*cos(angle*pi/180)
// initial dimensions of the droplet (box)

#define	Lx 1.5	// Initial droplet length
#define	Ly 0.5	// Initial droplet width
#define	Lz 1.5	// Initial droplet height
#define	rx0 1	// Bottom size ratio with respect to the initial droplet x-length
#define	ry0 1	// Bottom size ratio with respect to the initial droplet y-length
#define	Vdroplet 5	// Droplet volume

constraint 1   // Constraint for vertices and edges in contact with filament 1.
formula: (x-Lx/2-DL)^2 + y^2 = rodr^2
energy:
e1: 0 // -rode*z*y/rodr
e2: 0 // rode*z*(x-Lx/2-DL)/rodr
e3: 0

// Horizontal symmetry place
constraint 2   // Constraint to include horizontal symmetry.
formula: z = 0

constraint 3 nonnegative   // Constraint to keep the liquid away from the filament surface.
formula: (x-Lx/2-DL)^2+y^2 = rodr^2

constraint 4 nonnegative   // Constraint to keep the liquid away from the filament surface.
formula: (x+Lx/2+DL)^2+y^2 = rodr^2

constraint 5   // Constraint for vertices and edges in contact with filament 2.
formula: (x+Lx/2+DL)^2 + y^2 = (rodr*ratio)^2
energy:
e1: 0 // -rode*z*y/(rodr*ratio)
e2: 0 // rode*z*(x+Lx/2+DL)/(rodr*ratio)
e3: 0

vertices

1	-Lx/2	Ly/2	0	constraint 2,5

2	-Lx/2	-Ly/2	0	constraint 2,5	
3	Lx/2	-Ly/2	0	constraint 2,1	
4	Lx/2	Ly/2	0	constraint 2,1	
5	-Lx/2	Ly/2	Lz	constraint 5	
6	-Lx/2	-Ly/2	Lz	constraint 5	
7	Lx/2	-Ly/2	Lz	constraint 1	
8	Lx/2	Ly/2	Lz	constraint 1	
9	-rx0*Lx/2	ry0*Ly/2	0	fixed	// On symmetrical plane
10	-rx0*Lx/2	-ry0*Ly/2	0	fixed	// On symmetrical plane
11	rx0*Lx/2	-ry0*Ly/2	0	fixed	// On symmetrical plane
12	rx0*Lx/2	ry0*Ly/2	0	fixed	// On symmetrical plane
13	-Lx/2	-Ly/2	-Lz	constraints 5	
14	Lx/2	-Ly/2	-Lz	constraints 1	
15	Lx/2	Ly/2	-Lz	constraints 1	
16	-Lx/2	Ly/2	-Lz	constraints 5	

edges
1	2	3	constraint 2
2	4	1	constraint 2
3	2	6	constraint 5
4	3	7	constraint 1
5	4	8	constraint 1
6	1	5	constraint 5
7	6	7	
8	7	8	constraint 1
9	8	5	
10	5	6	constraint 5
11	13	14	
12	15	16	
13	13	2	constraint 5
14	14	3	constraint 1
15	15	4	constraint 1
16	16	1	constraint 5
17	16	13	constraint 5
18	14	15	constraint 1
19	3	4	constraint 1,2
20	2	1	constraint 2,5

faces
1	1	4	-7	-3	tension tens	color lightred	// side face 1
2	2	6	-9	-5	tension tens	color lightred	// side face 2
3	7	8	9	10	tension tens	color lightred	// top surface
4	11	14	-1	-13	tension tens	color lightred	
5	12	16	-2	-15	tension tens	color lightred	
6	11	18	12	17	tension tens	color lightred	
7	20	6	10	-3	constraint 5	tension rode	color lightgrey
8	-17	16	-20	-13	constraint 5	tension rode	color lightgrey
9	18	15	-19	-14	constraint 1	tension rode	color lightgrey
10	19	5	-8	-4	constraint 1	tension rode	color lightgrey

bodies
1	1 2 3 4 5 -6 7 8 9 10	volume Vdroplet

read   // some initialization

90

transforms off   // jest show fundamental region to start with

// a slight pertubation, to check stability
perturb:= set vertex y y+.01 where not on_constraint 1

hessian_normal // to make Hessian well-behaved
linear_metric // to normalize eignhvalues

2   Data file for the droplet-bridge shaped morphology. (1/8 Model):

Parameter	rodr =1.5	//fiber radius.
#define	DL 1	// distance between the fiber surface and the symmetric plane.
#define	Lx DL+rodr/sqrt(2)	//initial droplet length
#define	Dx rodr/sqrt(2)	
#define	Ly 3	// Initial droplet width
#define	Lz 15	// Initial droplet height
#define	Vdroplet 25	// Droplet volume
parameter	angle1 = 60	// fiber-liquid contact angle
parameter	angle2 = 90	// plane-liquid contact angle-(90-degree for two-fiber bridge)
parameter	tens = 1	// surface tension of free surface

#define	rode -tens*cos(angle1*pi/180)	// relative fiber-liquid interfacial tension
#define	pane -tens*cos(angle2*pi/180)	// relative plane-liquid interfacial tension

constraint 1   // Constraint for symmetry about X-axis.
formula: x = 0

constraint 2   // Constraint for symmetry about Y-axis.
formula: y = 0

constraint 3   // Constraint for symmetry about Z-axis.
formula: z = 0

constraint 4   // Constraint for vertices and edges on filament surface.
formula: (x+DL+rodr)^2 + y^2 = rodr^2

constraint 5 nonnegative   // Constraint to keep the liquid away from filament surface.
formula: (x+DL+rodr)^2+y^2 = rodr^2

vertices

1	-Lx	Ly	0	constraint 3,4
2	-Lx+Dx	0	0	constraint 2,3,4
3	0	0	0	constraint 1,2,3
4	0	Ly	0	constraint 1,3
5	-Lx	Ly	Lz	constraint 4
6	-Lx+Dx	0	Lz	constraint 2,4
7	0	0	Lz	constraint 1,2
8	0	Ly	Lz	constraint 1

edges

1	2	3	constraint 2,3
2	4	1	constraint 3
3	2	6	constraint 2,4

91

4	3	7			constraint 1,2		
5	4	8			constraint 1		
6	1	5			constraint 4		
7	6	7			constraint 2		
8	7	8			constraint 1		
9	8	5					
10	5	6			constraint 4		
11	3	4			constraint 1,3		
12	1	2			constraint 3,4		

faces

1	1	4	-7	-3	constraint 2	tension 0	color lightred
2	2	6	-9	-5	tension tens	color lightred	
3	7	8	9	10	tension tens	color lightred	
4	-4	11	5	-8	constraint 1	tension pane	color lightred
5	12	3	-10	-6	constraint 4	tension rode	color lightgrey
6	1	11	2	12	constraint 3	tension 0	color lightgrey

bodies

1	1 2 3 4 5 -6		volume Vdroplet

3. Data file for the barrel-shaped morphology. (Complete Model):

parameter	rodr = 0.5	//filament radius
#define	DL (rodr/sqrt(2))	// initial dimension of fiilament
parameter	spin = 0.0	// angular velocity
parameter	angle = 0	// internal contact free surface
parameter	tens = 1	// surface tension of free surface
#define	rode -tens*cos(angle*pi/180)	// liquid-fiber interface energy
parameter	dens= 0	// density of liquid, negative for bubble

// initial dimensions of the droplet (box)

#define	Lx	8	// Initial droplet length
#define	Ly	2	// Initial droplet width
#define	Lz	3	// Initial droplet height
#define	shift	5	// distance between two fibers
#define	rx0	1.5	// Bottom size ratio with respect to the initial x-length.
#define	ry0 2.0		// Bottom size ratio with respect to the initial y-length
#define	Vdroplet 25*10		// Droplet volume

quantity centrip energy global_method facet_vector_integral
vector_integrand:
q1: 0
q2: 0
q3: -0.5*dens*spin*spin*(x^2+y^2)*z

// y moment, for detecting instability
quantity ymoment info_only global_method facet_vector_integral
vector_integrand
q1: 0
q2: 0
q3: y*z

constraint 1   // Constraint for vertices and edges on upper right filament.
formula: $(x-shift/2)^2 + y^2 = rodr^2$
energy:
e1: -rode*z*y/rodr
e2: rode*z*(x-shift/2)/rodr
e3: 0
// Horizontal symmetry place
constraint 2   // Constraint to incorporate symmetry.
formula: z = 0

constraint 3 nonnegative   // Constraint to keep liquid away from right filament.
formula: $(x-shift/2)^2+y^2 = rodr^2$

parameter   pp2=pi/2   // to be halved each refinement.
parameter   qq2=pi/6   // to be halved each refinement.
constraint 4   //Constraint to divide edges evenly after refinement.
formula: (atan2(y,x-shift/2)+pi/6-pi/4) % pp2 = qq2

constraint 5   // Constraint for vertices and edges on upper left filament.
formula: $(x+shift/2)^2 + y^2 = rodr^2$
energy:
e1: -rode*z*y/rodr
e2: rode*z*(x+shift/2)/rodr
e3: 0

constraint 6 nonnegative   // Constraint to keep liquid away from left filament.
formula: $(x+shift/2)^2+y^2 = rodr^2$

parameter   pp=pi/2   // to be halved each refinement.
parameter   qq=pi/6   // to be halved each refinement.
constraint 7   //Constraint to divide edges evenly after refinement.
formula: (atan2(y,x+shift/2)+pi/6-pi/4) % pp = qq

constraint 8   // Constraint for vertices and edges on lower right filament.//
formula: $(x-shift/2)^2 + y^2 = rodr^2$
energy:
e1: rode*z*y/rodr
e2: -rode*z*(x-shift/2)/rodr
e3: 0

constraint 9   // Constraint for vertices and edges on lower left filament.//
formula: $(x+shift/2)^2 + y^2 = rodr^2$
energy:
e1: rode*z*y/rodr
e2: -rode*z*(x+shift/2)/rodr
e3: 0

vertices

1	-Lx/2	Ly/2	0	constraint 2	// equatorial vertices
2	-Lx/2	-Ly/2	0	constraint 2	
3	Lx/2	-Ly/2	0	constraint 2	
4	Lx/2	Ly/2	0	constraint 2	

5	-Lx/2	Ly/2	Lz		// upper outer corners
6	-Lx/2	-Ly/2	Lz		
7	Lx/2	-Ly/2	Lz		
8	Lx/2	Ly/2	Lz		
9	-DL+shift/2	DL	Lz	constraints 1,4	// vertices on the right fiber
10	-DL+shift/2	-DL	Lz	constraints 1,4	
11	DL+shift/2	-DL	Lz	constraints 1,4	
12	DL+shift/2	DL	Lz	constraints 1,4	
13	-rx0*Lx/2	ry0*Ly/2	0	fixed	// On symmetrical plane
14	-rx0*Lx/2	-ry0*Ly/2	0	fixed	
15	rx0*Lx/2	-ry0*Ly/2	0	fixed	
16	rx0*Lx/2	ry0*Ly/2	0	fixed	
17	-DL-shift/2	DL	Lz	constraints 5,7	// vertices on the left fiber
18	-DL-shift/2	-DL	Lz	constraints 5,7	
19	DL-shift/2	-DL	Lz	constraints 5,7	
20	DL-shift/2	DL	Lz	constraints 5,7	
21	-Lx/2	Ly/2	-Lz		// upper outer corners.
22	-Lx/2	-Ly/2	-Lz		
23	Lx/2	-Ly/2	-Lz		
24	Lx/2	Ly/2	-Lz		
25	-DL+shift/2	DL	-Lz	constraints 4,8	// vertices on lower rgh fiber.
26	-DL+shift/2	-DL	-Lz	constraints 4,8	
27	DL+shift/2	-DL	-Lz	constraints 4,8	
28	DL+shift/2	DL	-Lz	constraints 4,8	
29	-DL-shift/2	DL	-Lz	constraints 7,9	// vertices on lower left fiber.
30	-DL-shift/2	-DL	-Lz	constraints 7,9	
31	DL-shift/2	-DL	-Lz	constraints 7,9	
32	DL-shift/2	DL	-Lz	constraints 7,9	

edges

1	1	2	constraint 2	// equatorial edges
2	2	3	constraint 2	
3	3	4	constraint 2	
4	4	1	constraint 2	
5	5	6		// upper outer edges
6	6	7		
7	7	8		
8	8	5		
9	9	10	constraint 1,4	// edges on upper right fiber
10	10	11	constraint 1,4	
11	11	12	constraint 1,4	
12	12	9	constraint 1,4	
13	1	5		// vertical outer edges
14	2	6		
15	3	7		
16	4	8		
17	5	17		// cutting up top face
18	6	18		
19	7	11		
20	8	12		
25	19	10		
26	20	9		
27	17	18	constraint 5,7	// edges on upper left fiber
28	18	19	constraint 5,7	

94

29	19	20				constraint 5,7	
30	20	17				constraint 5,7	
31	21	22					
32	22	23					
33	23	24					
34	24	21					
35	21	1					
36	22	2					
37	23	3					
38	24	4					
39	29	30				constraint 7,9	// edges on lower left fiber
40	30	31				constraint 7,9	
41	31	32				constraint 7,9	
42	32	29				constraint 7,9	
43	25	26				constraint 4,8	// edges on lower right fiber
44	26	27				constraint 4,8	
45	27	28				constraint 4,8	
46	28	25				constraint 4,8	
47	21	29					
48	22	30					
49	23	27					
50	24	28					
51	31	26					
52	32	25					

faces

1	1	14	-5	-13			tension tens	// side faces
2	2	15	-6	-14			tension tens	
3	3	16	-7	-15			tension tens	
4	4	13	-8	-16			tension tens	
5	5	18	-27	-17			tension tens	// top faces
6	6	19	-10	-25	-28	-18	tension tens	
7	7	20	-11	-19			tension tens	
8	8	17	-30	26	-12	-20	tension tens	
9	-29	25	-9	-26			tension tens	
11	36	-1	-35	31			tension tens	
12	37	-2	-36	32			tension tens	
13	38	-3	-37	33			tension tens	
14	35	-4	-38	34			tension tens	
15	39	-48	-31	47			tension tens	
16	40	51	44	-49	-32	48	tension tens	
17	45	-50	-33	49			tension tens	
18	46	-52	42	-47	-34	50	tension tens	
19	41	52	43	-51			tension tens	

bodies

1	1 2 3 4 5 6 7 8 9 11 12 13 14 15 16 17 18 19	volume Vdroplet

read
transforms off

// special refinement command redfinition
r2:={autorecalc off; pp:= pp/2; qq:=qq%pp; pp2:= pp2/2; qq2:=qq2%pp2; 'r'; autorecalc on;}

// a slight pertubation, to check stability
perturb:= set vertex y y+.01 where not on_constraint 1

hessian_normal // to make Hessian well-behaved
linear_metric // to normalize eigenvalues

4.   Data file for the barrel-shaped morphology. (1/8 Model):

```
parameter        rodr = 1.0                          // Filament radius.
parameter        DL =2                               // Distance between filament center and plane.
parameter        vdroplet =133                       // 1/8-Volume of liquid droplet
parameter        spin = 0.0                          // angular velocity
parameter        angle =  60                         // fiber/liquid contact
parameter        angle2 = 90                         // internal contact free surace-- plane/liquid
parameter        tens = 1                            // surface tension of free surface
parameter        LL =  vdroplet^(1/3)                //approximate droplet dimension

#define          dis rodr+DL                         // Distance between fiber center and plane
#define          Lz LL                               // half-initial droplet height
#define          Lx  LL/2                            // half-initial droplet length
#define          Ly LL                               // half-inital droplet width
#define          rode (-tens*cos(angle*pi/180))      // contact angle energy of fiber
#define          pane (-tens*cos(angle2*pi/180))     // contact angle energy of plane

constraint 1                              .           // Constraint for vertices and edges on filament surface.
formula: x^2 + y^2 = rodr^2
energy:
e1: -rode*z*y/rodr
e2: rode*z*x/rodr
e3: 0

// Horizontal symmetry place
constraint 2                                          // Symmetry about Z-axis.
formula: z = 0

constraint 3 nonnegative                              // Constraint to keep liquid away from filament surface.
formula: x^2+y^2 = rodr^2

parameter pp=pi/2 /* to be halved each refinement */
parameter qq=pi/6 /* to be halved each refinement */
constraint 4                                          // Constraint to divide curved surface evenly.
formula: (atan2(y,x)+pi/6-pi/4) % pp = qq

constraint 5
formula: x= dis

constraint 6 nonpositive
formula: x= dis

constraint 7
formula: y= 0

constraint 8 nonnegative
formula: y= 0
```

96

vertices

1	-Lx	0	0	constraint 2,7
2	dis	0	0	constraint 2,5,7
3	dis	Ly	0	constraint 2,5
4	-Lx	Ly	0	constraint 2
5	-Lx	0	Lz	constraint 7
6	dis	0	Lz	constraint 5,7
7	dis	Ly	Lz	constraint 5
8	-Lx	Ly	Lz	
9	-rodr/sqrt(2)	0.0	Lz	constraint 1,7
10	rodr/sqrt(2)	0.0	Lz	constraint 1,7
11	rodr/sqrt(2)	rodr/sqrt(2)	Lz	constraint 1,4
12	-rodr/sqrt(2)	rodr/sqrt(2)	Lz	constraint 1,4
13	-rodr/sqrt(2)	0.0	0.0	constraint 1,2,7
14	rodr/sqrt(2)	0.0	0.0	constraint 1,2,7

edges

1	1	13	constraint 2,7
2	2	3	constraint 2,5
3	3	4	constraint 2
4	4	1	constraint 2
5	5	9	constraint 7
6	6	7	constraint 5
7	7	8	
8	8	5	
9	10	6	constraint 7
10	10	11	constraint 1,4
11	11	12	constraint 1,4
12	12	9	constraint 1,4
13	1	5	constraint 7
14	2	6	constraint 5,7
15	3	7	constraint 5
16	4	8	
17	13	9	constraint 1,7 // cutting up top face
18	14	10	constraint 1,7
19	7	11	
20	8	12	
21	14	2	constraint 2,7

faces

1	17	-5	-13		constraint 7	color lightred	tension pane
2	21	14	-9	-18	constraint 7	color lightred	tension pane
3	2	15	-6	-14	constraint 5	color lightred	tension pane
4	3	16	-7	-15	tension tens	color lightred	
5	4	13	-8	-16	tension tens	color lightred	
6	5	-12	-20	8	tension tens	color lightred	
7	9	6	19	-10	tension tens	color lightred	
8	7	20	-11	-19	tension tens	color lightred	

bodies

97

```
1     1 2 3 4 5 6 7 8              volume Vdroplet
read
transforms off
r2:={autorecalc off; pp := pp/2; qq :=qq % pp; 'r'; autorecalc on;}
perturb:= set vertex y y+.01 where not on_constraint 1
hessian_normal // to make Hessian well-behaved
linear_metric // to normalize eignhvalues
```

APPENDIX B: SURFACE EVOLVER DATAFILE – CHAPTER 4

Data file to determine capillary torque in droplet-bridge morphology

parameter	R1 = 1	// fiber 1 radius 0.05/2 mm
parameter	R2 = 1	// fiber 2 radius 0.1/2 mm
parameter	angle1 = 60	// Left R1-fiber contact angle
parameter	angle2 = 60	// Right R2-fiber contact angle
parameter	theta = 30	// angle between two fibers
parameter	tens =1	// surface tension of free surface

#define	DL 0.5	// Fiber spacing mm
#define	Lz 8	
#define	rode1 -tens*cos(angle1*pi/180)	// Left R1-fiber liquid-fiber interface energy
#define	rode2 -tens*cos(angle2*pi/180)	// Right R2-fiberliquid-fiber interface energy
#define	SIN sin(theta*pi/180)	
#define	COS cos(theta*pi/180)	
#define	Vdroplet 5	// Droplet volume

constraint 1
formula: x^2 + y^2 = R1^2

constraint 2
formula: (x-R1-R2-DL)^2 + (COS*(y-Lz/2*SIN)+SIN*(z-Lz/2*(1-COS)))^2 = R2^2

constraint 3 nonnegative
formula: x^2 + y^2 = R1^2

constraint 4 nonnegative
formula: (x-R1-R2-DL)^2 + (COS*(y-Lz/2*SIN)+SIN*(z-Lz/2*(1-COS)))^2 = R2^2

vertices

1	R1/sqrt(2)	-R1/sqrt(2)	Lz	constraint 1
2	R1	0	Lz	constraint 1
3	R1/sqrt(2)	R1/sqrt(2)	Lz	constraint 1
4	R1+DL+R2/sqrt(2)	COS*(R2/sqrt(2)-Lz/2*SIN)+SIN*(Lz-Lz/2*(1-COS))		
	-SIN*(R2/sqrt(2)-Lz/2*SIN)+COS*(Lz-Lz/2*(1-COS))			constraint 2
5	R1+DL	COS*(-Lz/2*SIN)+SIN*(Lz-Lz/2*(1-COS))		
	-SIN*(-Lz/2*SIN)+COS*(Lz-Lz/2*(1-COS))			constraint 2
6	R1+DL+R2/sqrt(2)	COS*(-R2/sqrt(2)-Lz/2*SIN)+SIN*(Lz-Lz/2*(1-COS))		-
	SIN*(-R2/sqrt(2)-Lz/2*SIN)+COS*(Lz-Lz/2*(1-COS))			constraint 2
7	R1/sqrt(2)	-R1/sqrt(2)	0	constraint 1
8	R1	0	0	constraint 1
9	R1/sqrt(2)	R1/sqrt(2)	0	constraint 1
10	R1+DL+R2/sqrt(2)	COS*(R2/sqrt(2)-Lz/2*SIN)+SIN*(-Lz/2*(1-COS))		
	-SIN*(R2/sqrt(2)-Lz/2*SIN)+COS*(-Lz/2*(1-COS))			constraint 2
11	R1+DL	COS*(-Lz/2*SIN)+SIN*(-Lz/2*(1-COS))		-
	SIN*(-Lz/2*SIN)+COS*(-Lz/2*(1-COS))			constraint 2
12	R1+DL+R2/sqrt(2)	COS*(-R2/sqrt(2)-Lz/2*SIN)+SIN*(-Lz/2*(1-COS))		
	-SIN*(-R2/sqrt(2)-Lz/2*SIN)+COS*(-Lz/2*(1-COS))			constraint 2

edges

1	1	2		constraint 1
2	2	3		constraint 1
3	3	4		
4	4	5		constraint 2
5	5	6		constraint 2
6	6	1		
7	7	8		constraint 1
8	8	9		constraint 1
9	9	10		
10	10	11		constraint 2
11	11	12		constraint 2
12	12	7		
13	7	1		constraint 1
14	8	2		constraint 1
15	9	3		constraint 1
16	10	4		constraint 2
17	11	5		constraint 2
18	12	6		constraint 2

faces

1	12	7	8	9	10	11	tension tens		// bottom surface
2	-6	-5	-4	-3	-2	-1	tension tens		// top surface
3	-12	18	6	-13			tension tens		// front surface
4	-9	15	3	-16			tension tens		// back surface
5	13	1	-14	-7			constraints 1,3	tension rode1	// R1-fiber/liquid interface
6	14	2	-15	-8			constraints 1,3	tension rode1	// R1-fiber/liquid interface
7	16	4	-17	-10			constraints 2,4	tension rode2	// R2-fiber/liquid interface
8	17	5	-18	-11			constraints 2,4	tension rode2	// R2-fiber/liquid interface

bodies

1	1 2 3 4 5 6 7 8	volume Vdroplet

read
transforms off

// special refinement command redfinition
//r2:={autorecalc off; pp:= pp/2; qq:=qq%pp; pp2:= pp2/2; qq2:=qq2%pp2; 'r'; autorecalc on;}

// a slight pertubation, to check stability
perturb:= set vertex y y+.01 where not on_constraint 1

hessian_normal // to make Hessian well-behaved
linear_metric // to normalize eignhvalues

APPENDIX C: LIST OF PUBLICATIONS AND PRESENTATION

1. **Amol Bedarkar** and Xiang-Fa Wu, "Capillary torque in a liquid bridge between two angled filaments," *Journal of Applied Physics* 2009, **106** (11): Art. No. 113527 (5 Pages).

   This paper was also collected in *Virtual Journal of Nanoscale Science and Technology* **20**(25), December 21 (2009) and *Virtual Journal of Biological Physics Research* **18** (12), December 15, (2009).

2. Xiang-Fa Wu, **Amol Bedarkar**, and K. Abraham Vaynberg, "Droplets wetting on filament rails: surface energy and morphology transition," *Journal of Colloids and Interface Science* 2010, **341** (2): 326-332.

3. **Amol Bedarkar**, Xiang-Fa Wu, and Abe Vaynberg, "Wetting of liquid droplets on parallel filaments" *Applied Surface Science, 2010, 256 (21): 7260-7264.*

4. Xiang-Fa Wu, **Amol Bedarkar**, and Iskander S. Akhatov, "Capillary effect in the mechanical behavior of compliant nanofibers wetted with droplets," *Journal of Applied Physics* **108**, 083518 (2010) (*6 pages*)

5. Xiang-Fa Wu and **Amol Bedarkar**, "Droplets engulfing on a filament," *Journal of Colloid and Interface Science* (in preparation).

6. **Amol Bedarkar**, "Droplets wetting on filament rails: Morphology transition and capillary torque -- A computational approach," Graduate Seminar Presentation, Department of Mechanical Engineering, North Dakota State University, Fargo, ND, November 12, 2009.

7. Xiang-Fa Wu and **Amol Bedarkar**, "Computational modeling of droplets wetting on microfibers and applications," *Proceedings of 3rd International Conference of Modeling and Computation*, Wuxi, China, June 3-6, 2010 (to be presented).

APPENDIX D: ABOUT THE AUTHOR

Amol Bedarkar was born and raised in a small town in western India named 'Satara'. He completed his Bachelor's degree in Mechanical Engineering at the Pune University (India). After completion of his Bachelor's degree, he worked at Mahle Filters (India) for two and half years in design engineering. Then, he came to the United States to pursue his graduate studies in the Department of Mechanical Engineering at North Dakota State University (NDSU), Fargo. He is currently working with "Cummins Inc".